

2-P(mix)

(NASA-CR-115639) ABSORPTION SPECTROMETER N72-25343  
BALLOON FLIGHT AND IODINE INVESTIGATIONS  
(Barringer Research Ltd.) Aug. 1970 - 136 p  
CSCL 04A Unclas  
G3/13 30383

BARRINGER RESEARCH LIMITED  
304 CARLINGVIEW DRIVE  
REXDALE, ONTARIO, CANADA

Reproduced by  
NATIONAL TECHNICAL  
INFORMATION SERVICE  
U S Department of Commerce  
Springfield VA 22151

OFFICE OF PRIME RESPONSIBILITY



FINAL REPORT  
ABSORPTION SPECTROMETER BALLOON  
FLIGHT & IODINE INVESTIGATIONS

PREPARED FOR  
NATIONAL AERONAUTICS AND SPACE ADMINISTRATION  
MANNED SPACECRAFT CENTER  
HOUSTON, TEXAS  
CONTRACT NO. NAS9-9492

PREPARED BY  
BARRINGER RESEARCH LIMITED  
304 CARLINGVIEW DRIVE  
REXDALE, ONTARIO, CANADA  
AUGUST 1970

TR70-148 ✓

TABLE OF CONTENTS

<u>SECTION</u>	<u>DESCRIPTION</u>	<u>PAGE.NO.</u>
	INTRODUCTION	1
	SUMMARY & CONCLUSIONS	
	PART I	
1	BACKGROUND	5
2	EXPERIMENTAL APPROACH	7
3	INSTRUMENT DESIGN & MODIFICATIONS	9
	3.1    SO <sub>2</sub> & NO <sub>2</sub> SPECTROMETER	9
	3.2    RADIOMETER	11
	3.2.1    INSTRUMENT PARAMETERS	12
	3.3    GONDOLA LAYOUT & ANCILLARY EQUIPMENT	13
	3.4    SUN TRACKER	13
	3.5    ENVIRONMENTAL TESTS	15
	3.6    HIGH ALTITUDE SIMULATIONS TESTS	15
	3.6.1    TEST FACILITIES	15
	3.7    RESULTS	16
4	INTEGRATION AT WINZEN RESEARCH	20
5	PREPARATIONS FOR LAUNCH	21
6	DATA COLLECTION	23
7	METEOROLOGY OVER CHICAGO	27
	PART II	
8	DATA PLOTS	32
	8.1    STATION WAGON	32
	8.2    BALLOON	32
	8.2.1    COMPUTERIZED DATA REDUCTION	33
	8.2.2    SO <sub>2</sub> /NO <sub>2</sub> VECTOR PLOTS	37

TABLE OF CONTENTS

<u>SECTION</u>	<u>INTRODUCTION</u>	<u>PAGE NO.</u>
9	DISCUSSION OF RESULTS	38
	PART III	
10	BACKGROUND	45
11	PROGRAM OBJECTIVES & EXPERIMENTAL APPROACH	46
12	SITE SELECTION	48
13	INSTRUMENT MODIFICATION & REFURBISHMENT	49
14	FIELD TESTS RESULTS	50
	14.1 PORPHYRY COPPER DEPOSITS	50
	14.2 OIL FIELDS	53
	14.3 GEOTHERMAL EMISSIONS	56
	14.4 WET CHEMICAL ANALYSES	57
	14.4.2 AIR ANALYSES- CATALYTIC METHOD	57
	14.4.3 PORPHYRY COPPER (SIERRITA PIT)	58
	14.4.4 OIL FIELD - MIDWAY SUNSET	59
	14.4.5 GEOTHERMAL SOURCES (GEYSERVILLE)	60
15	DISCUSSION OF RESULTS	
16	AIRCRAFT & SPACECRAFT APPLICATIONS OF THE I <sub>2</sub> CORRELATION SPECTROMETER	65
	16.1 INTRODUCTION	65
	16.2 SIGNAL-TO-NOISE RATIO	66
	16.3 SPECTRAL RADIANCES AVAILABLE AT THE INSTRUMENT	69
	16.3.1 SKY SPECTRAL RADIANCE	69
	16.3.2 SOLAR REFLECTED SPECTRAL RADIANCE AIRBORNE INSTRUMENT	71
	16.3.3 ATMOSPHERIC SCATTERED SPECTRAL RADIANCE, SATELLITE PLATFORM	72

TABLE OF CONTENTS

<u>SECTION</u>		<u>DESCRIPTION</u>	<u>PAGE NO.</u>
16	16.4	SIGNAL-TO-NOISE RATIO CALCULATIONS	72
	16.5	CONCLUDING OBSERVATIONS	77
17		ACKNOWLEDGEMENTS	79
		REFERENCES	80

## INTRODUCTION

### NATURE OF FINAL REPORT

This report presents the results of work performed under contract to NASA Manned Spacecraft Center, Houston, Texas, Contract No. NAS9-0402. This contract called for a high altitude balloon flight experiment to determine the technical feasibility of employing absorption spectroscopy to measure SO<sub>2</sub> and NO<sub>2</sub> gases in the earth's atmosphere from above the atmospheric ozone layer. In addition to the balloon experiment the contract includes a ground-based survey of natural I<sub>2</sub> emissions from geological sources and studies of the feasibility of mapping I<sub>2</sub> from spacecraft. This report is divided into three major sections as follows:

Part I covers the planning engineering and execution of the balloon experiment.

Part II deals with data reduction and analysis of the balloon data.

Part III presents the results of the I<sub>2</sub> phase of the contract.

It should be noted that much of the contents of this report, particularly the balloon data have been presented on previous occasions, see references (8) and (9). Also note that a review of the SO<sub>2</sub> raw chart data since publication of references (8) and (9) has produced some additional data points which have been added to Figures 26 and 27 in this report.

### SUMMARY AND CONCLUSIONS

#### Balloon Flight

The balloon was launched from Dowagiac, Michigan at 355 CST on Sept. 3rd 1969 and carried SO<sub>2</sub> and NO<sub>2</sub> correlation spectrometers, plus a radiometer, along a curving trajectory over Chicago at an altitude of 35 Km (114,000 ft.). All data

collected were transmitted to the ground in real time via FM/FM telemetry. The results indicate that all equipments in the scientific payload functioned essentially as planned with the exception of the radiometer which appeared to malfunction in one of the two UV channels and tended to saturate part of the time in the second UV channel. The visible channel was normal.

The unexpected curvature of the trajectory carried the payload directly over the south-east part of Chicago but scattered-to-broken cloud cover obscured much of the ground along the track. Unfortunately the NCAR ground-track recovery camera malfunctioned and the cloud pattern over the flight path had to be reconstructed from meteorological data and satellite photographs. The cloud cover analysis was performed by the Scientific Balloon Facility of the National Center for Atmospheric Research (NCAR). The ground track was developed from tracking data by Winzen Research Incorporated.

The loss of photographic coverage of the cloud formations under the balloon severely handicapped the interpretation of the  $\text{SO}_2$  and  $\text{NO}_2$  data and adds a significant degree of uncertainty to the validity of the results.

In spite of the uncertainties due to cloud cover, it is fair to conclude that the evidence strongly supports the view that the  $\text{SO}_2$  correlation spectrometer detected  $\text{SO}_2$  over Chicago. In the case of  $\text{NO}_2$  it appears highly likely that the signals received were in fact legitimate  $\text{NO}_2$  signals. The evidence in favour of this interpretation however is not nearly so strong as for  $\text{SO}_2$ .

The very compressed time scale of the entire program forced the acceptance of certain compromises in sensor performance the most significant of which deals with the optimization of the correlation masks. The masks were not optimized for maximum sensitivity to the target gas in the presence of a strong Fraunhofer background because to do so would have delayed the launch well beyond the August launch date. Instead the sensor's spectral operating range was adjusted to minimize the effect of Fraunhofer. In the case of  $\text{SO}_2$  the result was reasonably successful.

In the case of  $\text{NO}_2$  this compromise was less successful. In both cases, had more time been available to fully optimize the mask designs the sensitivities and the interpretive criteria for both sensors would have been substantially better.

On the subject of work that remains i.e. further analysis of the balloon data, there appears to be little to be gained in attempting to glean much more from it at this time. Usefulness of the radiometer data is definitely limited because of the apparent malfunction of one UV channel and the lack of photographic data.

#### Iodine Measurements Program

The long path (remote lamp) method of measurement proved unsatisfactory for absolute measurements of atmospheric  $\text{I}_2$  because of atmosphere-induced noise. Atmospheric turbulence imposed a threshold sensitivity of one ppb by volume or approximately  $10 \mu\text{gms}/\text{m}^3$  (over 1000 meters) which is above the upper limits of normal background  $\text{I}_2$ . This presumably includes all phases of the airborne  $\text{I}_2$  molecule whether it be chemically or organically combined, adsorbed on particles or as a free vapour.

Over the porphyry copper pits only sporadic measurements of anomalous levels of free vapour were recorded with the highest values being  $27 \mu\text{gms}/\text{m}^3$ . Over the oil field the highest values observed was about  $20 \mu\text{gms}/\text{m}^3$ .

In the passive mode the spectrometer performance was substantially better with a noise level of approximately 300 ppb-meters or  $3.15 \times 10^3 \mu\text{gms}/\text{m}^3$  referred to a path length of one meter or lower than the long path noise level by a factor of 3. A strong anomaly of 4.9 ppb-meters with a S/N ratio of 16 in passive mode measurements of the horizon sky over the oil field was recorded. This is equivalent to  $5.1 \times 10^4 \mu\text{gms}/\text{m}^3$  referred to a one meter path length.

The theoretical treatment of Section 16 shows that a more advanced instrument design using a fully optimized rotating correlation mask, multiple entrance slits and improved optical components is potentially capable of a photon noise level of  $1.3 \times 10^2 \mu\text{gms}/\text{m}^3$  referred to one meter i.e. a 25 fold improvement over the existing NASA sensor design. Ignoring atmospheric and ground reflectance noise sources this

represents an instrument noise equivalent signal, for a spacecraft sensor, roughly equivalent to the minimum background atmospheric  $I_2$  level of  $0.1 \mu\text{gms/m}^3$  assuming the background to be a homogeneous layer of some 1000 meters in depth and to be primarily in the free vapour phase. The possibility of noise generating phenomenon in the atmosphere such as wavelength dependent scattering by aerosol, and other mechanisms is yet unknown, degrading this theoretical performance should not be discounted however.

Errors or noise induced by wavelength dependent reflectance changes of the terrain are not expected to be large, since as shown in reference 7, the reflectance of most terrain materials is reasonably flat in the  $I_2$  absorption region. Since the difference in reflectance of these materials is large in this spectral region however, the requirements placed on the automatic gain control system will be considerably more severe than at shorter wavelengths such as in the blue visible for  $\text{NO}_2$  or the ultra-violet for  $\text{SO}_2$ .

In terms of program accomplishment, of the three geological features investigated only the oil field exhibited a distinct  $I_2$  vapour anomaly. Anomalous  $I_2$  levels in the vicinity of open pit porphyry were not detected. The steam field at Geyserville, California similarly did not indicate significant  $I_2$  emissions although this site in retrospect was probably an unfortunate choice for a representative geothermal target. The significance of  $I_2$  as a geochemical tracer for earth inventory purposes cannot be assessed adequately at this time without additional investigation. The advanced instrument design described in this report promises a 25 fold improvement in sensitivity over the existing NASA spectrometer. This predicted theoretical performance is solidly supported by comprehensive laboratory tests. It should be pointed out that a new sensor incorporating some of the basic features of the new design is presently being evaluated in the Barringer Research laboratories for application to other gases.

It is recommended that the iodine field measurements program be continued and that future work should utilize an advanced airborne spectrometer with enhanced sensitivity capable of clearly defining the potential role of iodine for earth resource monitoring purposes.

## PART I

### Section 1

#### BACKGROUND

A prime consideration in the detection of surface pollutants by remote sensing from above the earth's atmosphere is the level of radiant flux emerging from the top of the atmosphere which has been reflected by the earth's surface and its magnitude relative to emerging flux which has not reached the surface but has been reflected or back-scattered by the atmosphere. Figure 1 depicts the mechanisms involved and their influence on the remote sensor measurement. Note that attenuation of ultraviolet radiation occurs primarily by ozone absorption in the upper layer (between 20 and 30 Km) and by scattering in the more dense atmosphere between the ozone layer and the earth's surface. Note also that solar flux which has been reflected from the earth's surface and contains the desired gas signature must compete with backscattered flux containing little or no gas signature. This dilution effect is most severe in the ultraviolet and diminishes in severity with increasing wavelength. In addition, the relatively low reflectance of the earth's surface in the ultraviolet further reduces the useful SO<sub>2</sub> signal. Extensive tables exist for determining the flux levels emerging from the top of the atmosphere for various sun angles, molecular and aerosol number densities and ground albedoes (reference 1) but very little theoretical or experimental data exists which accurately describes the properties of a heavily polluted atmosphere over an industrial city. However, extensive tests of an airborne SO<sub>2</sub> remote sensor over industrialized areas (reference 2, 3) have clearly demonstrated a capability for aircraft pollutant monitoring and extrapolation of this performance to a spacecraft has indicated a good probability of success. This has provided the main impetus for the balloon experiment.

Figure 2 shows curves reproduced from the Air Force-Cambridge Handbook (reference 4) of the outgoing flux as a function of wavelength for various surface reflectances. The upper dashed curve is the incident solar flux for the sun at the zenith. Lines A and B indicate the approximate centre wavelength of the SO<sub>2</sub> and NO<sub>2</sub>

masks respectively. In specific terms the purpose of the balloon experiment was to determine if it is feasible to detect and measure SO<sub>2</sub> and NO<sub>2</sub> in the lower layers of the atmosphere at these wavelengths using the technique of absorption spectroscopy. The concept of a relatively low cost high altitude balloon experiment was developed in an earlier NASA contract (reference 2) and is based on the well-established fact that during the summer months, when observations of the ground from space are optimum, the velocities of high level winds at altitudes above the ozonosphere are nearly constant and hence highly predictable.

## Section 2

### EXPERIMENTAL APPROACH

The city of Chicago was chosen as the target for the balloon experiment primarily because of its size, pollutant source strength and excellent ground monitoring system.

In addition, within a radius of miles the region is relatively free of large industrial centers of comparable size and the target should therefore stand out as an unambiguous anomaly. Numerous small air fields in the neighbouring counties also offered the desired flexibility in launch site selection.

A balloon launch during August was decided upon since this was the earliest possible time for the equipment to be made ready and the sun angles and near-surface weather conditions would be preferable to later in the year. Towards the end of August, however, the upper level winds which characteristically blow steadily from east to west at about 60 knots enter the turn-around phase (at Chicago's latitude) and as the speed drops both the speed and direction become less predictable. From September 1st to October 15th the winds aloft are generally not suitable for balloon experiments. Assuming a launch in August, several promising launch sites were chosen in the South Bend area some 80 miles due east of Chicago.

In order to maximize the data obtained with one pass over the Chicago area, the field of view of the sensor system was required to scan from side to side at right angles to the anticipated east-to-west ground track through an arc of at least  $\pm 12$  degrees from the local vertical. This would provide sampling of the atmosphere over two parallel ground tracks approximately 10 miles apart. Since the balloon can be expected to rotate freely about its vertical axis a means of stabilizing the scan plane in azimuth was required. A relatively simple sun tracking, gondola stabilizing system developed by the University of Saskatchewan was chosen for the purpose not only because it satisfied the scan plane requirement but also because its use would eliminate another problem, namely signal fluctuations induced by a varying polarization angle of the solar flux back-

scattered from the atmosphere.

Since the spectrometer responses from  $\text{SO}_2$  and  $\text{NO}_2$  gas clouds near ground level were expected to be severely reduced by dilution light from the atmosphere, particularly in the  $\text{SO}_2$  channel, a means of measuring the dilution component was required. For this purpose a special radiometer was designed and built by Barringer Research to measure contrast ratios of the terrain at wavelengths of 3100 Å and 6000 Å. Briefly and in principle it scanned a small cone around the nadir and generated a high frequency output corresponding to the changes in reflectance plus a larger low frequency and DC component due to atmospheric backscatter. By using the average value of the signal to control an AGC loop, the high frequency output can be made proportional to the apparent contrast changes in the terrain. Then given the average values and variations in reflectance at the two wavelengths, the ratio of apparent and actual contrasts may be used to estimate the magnitude of the dilution effect. This approach however requires a rather precise record of the type of terrain materials viewed by the radiometer in time coincidence with the measurement as well as a knowledge of the actual contrasts of these materials.

Although not a contract requirement, a secondary experiment was planned to obtain a direct measure of the dilution factor. This comprised an upward-looking  $\text{SO}_2$  spectrometer mounted in ground vehicle which would be driven so as to position the sensor as close as possible to the balloon ground track, i.e. directly under the balloon during the flight. Then by comparing the balloon measurement of  $\text{SO}_2$  with that of the ground vehicle, with due regard for the multi-path factor in the balloon result, the best possible measure of dilution in the  $\text{SO}_2$  channel could be arrived at.

Figure 3 shows the primary  $\text{SO}_2$  sources in Chicago as provided by the city's Department of Air Pollution Control. Figure 4 shows the air-sampling sites including those tied into the automated telemetry network. Figure 5 shows the approximate anticipated path of the balloon. The dotted lines are meant to illustrate the sensors alternate look-angle produced by a FOV scanning mirror.

## Section 3

### INSTRUMENT DESIGN & MODIFICATIONS

#### 3.1 SO<sub>2</sub> & NO<sub>2</sub> SPECTROMETERS

Since the SO<sub>2</sub> and NO<sub>2</sub> spectrometer designs are essentially identical with the exception of wavelength considerations and the basic design is amply covered in the references provided (2), (4), the following is limited to a description of modifications required to optimize the basic design to meet the requirements of the balloon experiment.

The changes in design are as follows:

- (1) Replace fore-optics frame with welded assembly.
- (2) Fore-optics re-designed to achieve 1° X 1°.
- (3) Tuning fork mount re-designed for better support.
- (4) Refractor plates optimized for specific gas.
- (5) Entrance slit optimized for specific gas.
- (6) Correlation mask optimized with (4) & (5)
- (7) Grating scanner added to provide trace correlation.
- (8) Electronics re-built on integrated sensor head.
- (9) Integrated photo-multiplier and h.v. inverter.
- (10) Reference cells mounted on rotary solenoids.
- (11) Nickel sulfate filters replaced with infrared interference filter in SO<sub>2</sub> channel.

One of the more significant of the above modifications is the addition of a grating scan mechanism. This device provided a means of oscillating the grating back and forth between two selected mean wavelength positions at a rate determined by the frequency of pulses applied to a stepping motor. The result is two separate but superimposed motions of the target gas spectrum relative to the correlation mask; the rapid "jumping" motion between adjacent parts of the spectrum produced by the fork-driven refractor plates and a relatively slow steady oscillating motion due to the grating scanner. A full theoretical treatment of the electro-optical correlation function so produced is available in

reference (4). The following describes only the principles of the technique. The purpose of the grating scan function is apparent from Figure 6. Here is shown typical output signal traces when the grating was scanned in one direction over some  $100 \text{ \AA}$  in the  $\text{SO}_2$  absorption region, i.e. in the ultraviolet. Since the photo-detector and following electronics simply measures the ratio of net energy throughput for two positions of the slit array relative to the spectrum at a frequency determined by the tuning fork, the presence of absorption bands in the incoming spectrum will cause the output signal to swing through positive and negative peaks as the grating is slowly rotated. This assumes of course that the bands fall into registry with the slit array i.e. that they correlate. Because of the regular spacing of the  $\text{SO}_2$  absorption bands the correlation function swings through a series of evenly spaced peaks as shown in Figure 6. The use of the solar source for remote sensing with a correlation spectrometer requires detailed knowledge of the solar spectral distribution. The presence of abrupt irregularities in the source continuum will produce characteristic distortions in the output trace. This is apparent in the sky source trace of Figure 6. These traces were obtained with a six-slit  $\text{SO}_2$  mask designed to cover the range  $3000$  to  $3150 \text{ \AA}$  but not optimized for Fraunhofer rejection. Note the very pronounced sky signature as compared with the zero correlation output using the quartz iodine. There appears to be little doubt that correlation with Fraunhofer structure in the solar spectra is the primary reason for these distortions and this appears to be borne out by the high degree of constancy in position of the interfering bands regardless of the time or geographic location. Experience to date indicates that reliable measurements of target gas concentrations can be made by using the sky profile as a reference and observing departures from it due to absorption by the target gas. The lower trace shows the effect of superimposing a strong  $\text{SO}_2$  profile. It is evident then that it should be possible to extract the  $\text{SO}_2$  component from any given target signature by cross correlation with an  $\text{SO}_2$  reference waveform.

Figure 7 further illustrates the effect of increasing SO<sub>2</sub> concentrations. The interval bounded by the dotted lines is the scanning interval chosen for the balloon experiment. This particular interval was chosen because of the relatively high light level available and the relative ease of data interpretation.

Figure 8 shows similar profiles for NO<sub>2</sub>. These were obtained using a 5-slit mask covering the range 4300 to 4500 Å. Fraunhofer lines are particularly strong in this region and the Fraunhofer correlations coincide exactly with those for NO<sub>2</sub>. The method of measurement in this case is simply to observe the increase in peak-to-peak amplitude caused by NO<sub>2</sub> absorption. The dotted lines again indicate the interval used for the balloon experiment.

### 3.2 RADIOMETER

Principle of Operation - As previously described, the apparent and actual contrasts of the terrain viewed by the radiometer can be used to show how the ground-reflected radiation is diluted by back scatter. For example, if it is known that the terrain reflectance has changed from 5% to 6% in the ultraviolet then the corresponding radiometer signal is proportional to 1/5 the ratio of reflected to scattered radiation.

Since the scattered radiation in the red region is small, a similar scanning system working at these wavelengths will measure terrain reflectance changes directly and, if the type of terrain is known from photographic or ground-track data, these changes can be extrapolated from the red to the U.V. region of the spectrum.

This extrapolation is one of the main sources of uncertainty, since, apart from the difficulties of precisely identifying the reflecting materials, achieving an adequate signal/noise ratio requires that data be averaged before telemetry, so that a point by point comparison of the signals is not possible.

### 3.2.1 INSTRUMENT PARAMETERS

Figure 5 illustrates the operation of the radiometer. The 2" diameter, 10" focal-length mirror is attached to the motor shaft with its center of curvature  $2^\circ$  off the axis of rotation. The radiation from the mirror is divided by the U.V. filter which transmits a hundred angstrom band centered at  $3000 \text{ \AA}$  and reflects the rest. The reflected beam is filtered by a second  $100 \text{ \AA}$  wide filter and each beam is imaged onto a  $0.5^\circ$  diameter field stop in front of a 1P28 photomultiplier.

Since the angular scan rate of the mirror (380 radian/sec) is very large compared to the movement of the balloon ( $V/h = .7 \text{ mrad/sec}$ ), the signals due to the terrain consist of a series of harmonics of the mirror scan rate, that is signals of known frequency but unknown slowly varying phase. By processing the signal through two synchronous rectifier channels,  $90^\circ$  apart in phase, and vectorially combining the outputs, it is possible to achieve narrow effective bandwidths without the need for precisely controlled rotation rates or high Q filters. Such a phase quadrature system was used for the UV channel, where the expected signal/noise ratios were low. In the red channel, sufficient energy was available to permit the use of a comparatively broad filter which isolated the appropriate harmonic, followed by a half-wave rectifier and integrator. Taking the twelfth harmonic of the rotation rate corresponds to the highest spatial frequency resolvable by the optical system, i.e. changes in reflectance occurring in distances of the order of 1000 feet.

### 3.3 GONDOLA LAYOUT & ANCILLARY EQUIPMENT

Figure 10 shows the sensor payload. Both sensors scanned the ground through a common mirror assembly which was driven by a solenoid in bi-stable fashion from a position of vertical line of sight to a position  $24^\circ$  to the anti-solar side. The radiometer shared one mirror surface with the  $\text{SO}_2$  sensor. The bias to the anti-solar side was to take advantage of the reduced backscatter in the anti-solar direction. Spectral characteristics of the two sensors were as follows:

	$\text{SO}_2$	$\text{NO}_2$
Center Wavelength	3100 Å	4400 Å
Spectral Bandwidth	150 Å	200 Å
Grating Scan Range	6.2 Å	25 Å
Grating Scan Rate	1.0 cycles/min	0.8 cycles/min

A solenoid-driven diffuser plate and quartz iodine light source were provided for calibration purposes. Solenoid-actuated fused-silica reference cells were used in each sensor to determine incremental sensitivities during the flight. Quartz-iodine light sources and solenoid actuated diffuser plates were also employed as reference sources. The central area of the platform was reserved for the ballast chute and 16mm ground track recovery camera supplied by NCAR. The ground test control unit was used to simulate the input channels of the telecommand link and to provide jacking points for monitoring output signals to the telemetry equipment. In this way the complete scientific payload therefore could be checked out as an integrated working system. The scientific payload was contained entirely within the gondola framework as shown in Figure 11 (reproduced from Winzen Report, reference 5).

### 3.4 SUN TRACKER

The sun tracker design, provided by the University of Saskatchewan, was developed by U. of S. and used successfully on previous occasions (reference 6). In

principle the system is very simple and after a few modifications by Barringer Research proved to be a very satisfactory way of stabilizing the gondola in azimuth. The sun tracker consisted of three separate assemblies; the electronics, the solar cells and the rotator. The solar cells are shown mounted on a pedestal in Figure 11.

A circular baffle of appropriate size was mounted above the cell block so as to prevent solar reflection from the balloon reaching the cells without blocking the direct solar ray at the minimum zenith angle for a maximum pendulum half angle of  $5^{\circ}$ .

Figure 12 shows the block diagram of the sun tracker system. Briefly the operation may be described as follows:

The signal developed by the solar cells

$$E_{az} = G_{az} AP \cos \theta \quad \text{where } A = \text{cell area}$$

$$P = \text{incident solar flux}$$

$$G_{az} = \text{amplifier gain}$$

and after differentiating

$$E_{azd} = -G_{az} AP \sin \theta \frac{d\theta}{dt}$$

At the primary point the signal is simply

$$E_s = G_{az} AP \cos \theta - G_{azd} AP \sin \theta \frac{d\theta}{dt}$$

With appropriate adjustment of  $G_{az}$  and  $G_{azd}$  when  $\theta$  is small the  $\sin \theta$  component is small and the gondola will move under the influence of the position error component, to equalize AP from the back-to-back solar cells. As the equilibrium position is approached the opposing velocity component predominates, the motor reverses direction causing the gondola to slow down close to the null position. The position error once again comes into play to bring the system to rest with the plane of the solar cells aligned with incident solar rays. To avoid false driving

signals being introduced by pendulation, the planes of the cells were tilted up so the normal would approximate the mean sun position in elevation over the duration of the flight.

The critical parameter in the system is the loose friction coupling to the balloon suspension system. The original University of Saskatchewan design relied solely on bearing friction for torque transfer. During sun tracker tests using a simulated cable system it was found necessary to add a friction plate and teflon bearing to achieve reliable performance.

### 3.5 ENVIRONMENTAL TESTS

The original requirement for shock testing the sensing was waived because of the shortness of time and because the instruments were deemed sufficiently rugged to withstand the relatively low stress levels characteristic of a balloon flight.

### 3.6 HIGH ALTITUDE SIMULATIONS TESTS

#### 3.6.1 TEST FACILITIES

In order to simulate the conditions which would be encountered on an ascent to 120,000 feet, the wind tunnel at the University of Toronto Institute for Aeronautics Studies (UTIAS) was employed. This test chamber is 31 cu. ft. in volume and can be evacuated to 3 mm Hg in 30 minutes (equivalent to 120,000 ft.) By using a throttle plate the tunnel can simulate the ascent of a balloon remarkably well, arriving at 120,000 feet in 2 hours. Provision was made for liquid nitrogen to be pumped through a cooling coil in order to simulate the passage of the balloon through the cold dense troposphere.

Preparation for the work in the tunnel required the installation of a rotary feed-through coupling a 17 pin hermetically sealed plug and a BNC feed-through connector. This work was accomplished by UTIAS personnel.

The rotary feed-through was connected to a rotary test switch on the instrument by a speedometer cable. This allowed the selection of any one of the 12 electronic test points from outside the chamber while the instrument was under tests.

The 17 pin connector carried all input power, test leads, and signal leads which did not require shielding. The output test signal from the rotary switch was fed by a BNC lead to an oscilloscope external to the chamber.

Since the instrument required a light source, (quartz-iodine) to operate, one was installed in the chamber on a permanent tunnel fixture which allowed 5 degrees of freedom for positioning the lamp. The power lead was fed through existing connectors on the tunnel wall. A view of the tunnel showing an instrument in position is given in Figure 13.

### 3.7 RESULTS

The absorption spectrometer employs a photo-multiplier tube driven by a high voltage supply. This voltage was a concern as arcing could easily occur at the pressures involved. In order to minimize this problem the photomultiplier tube base was carefully removed, and the tube placed in a specially machined plastic housing. The high voltage supply, an inverter, was placed directly behind the PM tube, and enclosed in the housing. After connections were made the entire assembly was potted using a clear epoxy gel. The assembly with the still liquid gel was pumped down to 2 mm Hg pressure in a vacuum oven to ensure removal of all air entrapment. The PM tube assembly was then removed from the chamber and left to cure (about 3 days). The assembly was then placed inside a mu-metal shield and installed in the instrument. The only leads to this assembly were the -15V supply, the inverter control, the signal lead from the PM tube anode and ground lead. The epoxy gel should adhere to all materials, according to the supplier, but it was found that the cured material did suffer from shrinkage and actually pulled away from the acrylic housing. This proved to be no problem, however, as there were no components near these gaps.

After potting the PM tube assembly, it was noticed that electrical interference was affecting the signal output. The inverter was found to be the cause and it was necessary to use a shielded inverter (wrapped in aluminum foil which was connected to ground). This eliminated the electrical interference.

Both instruments had to undergo high altitude tests to ensure success of the flight. The NO<sub>2</sub> instrument was first made ready and taken to the test chamber after it had tested out properly in the lab. The instrument operated correctly up to about 35 mm Hg pressure where arcing began to occur. The presence of arcing could be observed at the output terminal of the F.E.T. pre-amplifier in the form of very high but very narrow spikes superimposed on the normal video signal.

Although they were not catastrophic and did not indicate incipient failure, their effect was such as to render the output signal unusable. This was traced to the hole used to insert the electrical shielding. After repairing the PM tube assembly the instrument was again tested. This time at 25 mm Hg pressure arcing was again observed. The entire rest chamber was then placed in darkness and all external view ports were covered except one which was used to observe the PM tube after removal of the mu-metal shielding. A blue corona discharge was observed in the area where the PM tube contacted the metal frame of the instrument as well as spurious flashes in the region of the inverter.

The instrument was then disassembled and the PM tube assembly was placed in a vacuum oven and positioned in such a way that the glass tube envelope was near the oven's metal structure which was grounded. A voltage regulator was placed in the chamber as well, in order to ascertain if the regulator could be causing the arcing due to some component failure at low pressure. The arcing was very noticeable near the glass envelope of the tube. It is felt that an electro-static charge buildup was induced outside the tube's glass envelope by the high voltage in the tube (1300 volts). This then flashed over to ground under rarefied conditions resulting in the blue corona discharge. The PM tube used is a Philips XP1002, 3, 4 type which employs a semi-transparent photocathode deposited on the glass or quartz window. This feature contributes to a charge buildup on the glass

envelope. A plastic tube was placed over the glass envelope and proved satisfactory in preventing this flash-over due to charge buildup. Some discharge was observed in the region of the inverter but was considered spurious as it had no effect on the signal output from the PM tube. Upon return to the UTIAS chamber the instrument performed properly and also worked at 2.71 mm Hg pressure. After soaking at 3mm Hg pressure over-night the instrument still performed satisfactorily. The maximum voltage obtainable (through a voltage divider), on the PM tube was 1300 volts. This proved to be too far below the tube manufacturer's recommended maximum voltage and it was necessary to rewind the inverter coil to reach the value recommended, 1800 volts.

At this time it was felt that perhaps the inert potting compound was affecting the inverter performance. Because of this question, plus the lengthy curing time required for potting and the very compressed time scale of the entire project, an aluminum pressure housing with quartz window was constructed which would keep the entire PM tube and inverter assembly at atmospheric pressure. This approach was used instead of the potted assembly. The NO<sub>2</sub> PM tube was found also to be defective and had to be replaced with another tube. The new PM tube assembly was installed first in the SO<sub>2</sub> instrument and it was subjected to the low pressure tests.

The SO<sub>2</sub> instrument performed properly during the simulated ascent to 120,000 feet and was still satisfactory after a 12 hour soaking period under normal light conditions. However, when the inverter voltage was adjusted to 1800 volts (i.e. no light) some residual arcing was observed. However, since the instrument is not intended to operate in total darkness and the arcs are not indicative of incipient failure the instrument was judged satisfactory for the high altitude environment. During the SO<sub>2</sub> test liquid nitrogen was pumped through the cooling coil. This, unfortunately, had very little effect on the temperature measured at the front or rear of the SO<sub>2</sub> instrument, in fact the reduction at the front was only 1° centigrade after 2 hours of coolant flow, due to the radiation cooling effect being minimal in relation to large bulk of the chamber walls. Since the internal gondola temperature was expected to be 27° during float

at 120,000 feet and cooling during climb out through the tropopause would be transitory only, the failure to test the SO<sub>2</sub> instrument at low temperatures and low pressure was not considered serious. The NO<sub>2</sub> instrument was subjected to -25°C temperatures at atmospheric pressure and came through the test very well with the only problem being the condensation of water on some part of the optics when the temperature was raised due to a high humidity being present on the test day.

Following the cold test the NO<sub>2</sub> instrument was returned to the UTIAS test chamber. The instrument performed exactly as did its sister instrument and both were ready, environmentally, to be flown.

The success of these environmental tests was proven when the instruments worked as planned during the 12 hour balloon flight over Chicago. No problems could be attributed to high voltage arcing or temperature effects, except the irregular noise pattern as described in Section 6 (page 21). This pattern was identical to that experienced during the simulated ascent tests conducted in the UTIAS environmental chamber.

## Section 4

### INTEGRATION AT WINZEN RESEARCH

The scientific payload arrived at Winzen Research in Minneapolis on August 22nd 1969, for integration with the gondola system. This work included mechanical fitting to the gondola framework, interfacing with the command and telemetry systems and testing for r.f. interference. Changes were made to the spectrometer control circuits to facilitate in-flight calibrations and additional outdoor tests were performed to finalize the grating scan parameters. Difficulties were encountered with the sun tracking system because of low torque transmission in the rotator. As described in section 3.4 this problem was solved by the addition of a friction plate provided by Winzen Research. For a full description of the telemetry and command channels refer to the Winzen report reference 5.

## Section 5

### PREPARATIONS FOR LAUNCH

On Sept. 1st, 1969 the launch crew and mobile equipment arrived at the Dowagiac, Michigan civil airport and preparations for the launch began immediately. This late arrival at the launch site was caused by an accumulation of minor delays in the program. As indicated previously, from September 1st to October 15th the winds aloft are generally not suitable for balloon experiments. However up until about August 26th meteorological reports showed the upper level winds were still holding and on the basis of computed trajectories performed regularly by NCAR's Palestine computer facility, Dowagiac Michigan was chosen as the launch site. By August 26th a deteriorating trend in wind conditions had set in and reliable trajectory predictions became more difficult. At midnight on Sept. 1st, a pre-launch planning meeting was held between NASA, NCAR, Winzen Research and Barringer Research. After a lengthy study of the anticipated wind conditions and possible alternate launch sites, a decision to launch was postponed for 24 hours. On Sept. 2nd NCAR's studies showed the upper level easterlies were still holding although growing weaker and more variable. However, surface conditions over Chicago appeared favourable for a launch the next day. The decision was made to launch on the morning of the following day (Sept. 3rd). Preparations for launch included a final check of instrument adjustments, sensor performance and sun tracker operation. Figure 14 shows the sensor platform under test on the day before the flight. Figure 15 is a close-up from the "front" of the gondola and Figure 16 shows the complete gondola system just before launch. The lower member is the crush pad. Urethane foam panels were used to enclose the sensor compartment. The telemetry command and balloon control equipments are mounted on the roof of the sensor compartment. The solar cell pedestal and sun tracker rotator are clearly visible. To prevent the ingress of cold moist air during climb-out, a plywood panel was fastened over the sensor viewing port and released by means of pressure switches before reaching float altitude. Moments before launch a final check was made of command and telemetry functions. The main power switch was closed to energize the sun tracker system. This was done as a

safeguard to minimize the chances of the rotator bearings tightening up or sticking from the extremes of temperature during climb out.

## Section 6

### DATA COLLECTION

The launch took place at 355 CST September 3, 1969. The NO<sub>2</sub> Spectrometer was turned on at 441 CST and the radiometer switched on by pressure switch at 510 CST. At 530 CST the SO<sub>2</sub> sensor was switched on. Severe noise appeared on all channels at 605 CST and remained until 645 CST. The cause was apparently the proximity of the balloon and attitude of the gondola antenna system. The balloon was moving overhead at this time. The characteristic Fraunhofer signature appeared on the NO<sub>2</sub> channel recorder early in the flight but the SO<sub>2</sub> amplitude was negligible.

At 7:06 CST the sun tracker had locked on and all systems were in operation. Both spectrometers, the sun tracker and scanning mirror system were functioning normally. The radiometer traces however showed that contrast levels in the UV (in  $\emptyset$ ) channel frequently exceeded the 5 volts dynamic range of the telemetry. and the UV (90°  $\emptyset$ ) signal was continuously outside this range. The visible (6000 Å) contrast levels were well within the range.

An irregular noise pattern made up of pulses of very short duration appeared in the SO<sub>2</sub> trace after making adjustments to the SO<sub>2</sub> sensor by telecommand. This noise is very similar to the electrostatic discharge spikes observed during the high altitude chamber tests at UTIAS and were very likely produced by the same cause. As described in Section 3.5 the effect which is believed to stem from the type of photomultiplier used, was greatly reduced by the use of a sealed photomultiplier housing but it could not be eliminated entirely at high operating voltages (low light level). Since the spike energy content is small their contribution to the signal amplitude is small. Their presence on the signal trace was effectively removed by connecting a capacitor across the recorder terminal.

A sample of the data chart from the six channel brush recorder is shown in Figure 17. The top trace shows the grating reversal markers produced by the micro-switches at the two limits of the grating scan. The next trace down is time phased between the U.V. (in  $\emptyset$ ) contrast measurement, the U.V.A.G.C. and the visible contrast signal. The middle trace is also time shared (by means of a rotary commutator) as indicated. The U.V. ( $90^\circ$ ) contrast is shown limiting at +2.5 V as previously mentioned.

The greater part of the chart speed shown in Figure 17 was obtained while the mirror was in the  $0^\circ$  position (FOV vertical). It has switched to the  $24^\circ$  position at the right hand end of the trace as indicated by the -2.1V amplitude. The AGC trace is time shared between the  $\text{SO}_2$  and  $\text{NO}_2$  sensors. The  $\text{NO}_2$  signal containing a large Fraunhofer component is shown, somewhat stretched, in the bottom trace.

Figure 18 shows data obtained later in the flight at the normal chart speed of 1mm/sec. The top trace shows noise bursts superimposed on the  $\lambda$  scan trace, by break-through from the radiometer UV (in  $\emptyset$ ) channel which occurs only when that signal exceeds the dynamic range of the telemetry. In the middle trace of Figure 18 the sinusoidal trace of the sun tracker illustrates the hunting action which is characteristic of this null-seeking loosely-coupled tracking system. This trace is the voltage applied to the driving motor and is proportional or nearly so, to the angular tracking error when the tracker is locked onto the sun. The peak-to-peak amplitude of the trace in Figure 18 represents an angular tracking error of approximately  $\pm 1.5^\circ$  about the null or zero error position. The sun tracker locked on at 706 CST and maintained lock-on until dumping ballast at 1725 CST.

The lower trace of Figure 18 shows a low resolution  $\text{SO}_2$  profile with the noise spikes previously discussed. This chart record was not used for obtaining  $\text{SO}_2$  or  $\text{NO}_2$  data but rather for obtaining timing information required for data reduction. The quantitative  $\text{SO}_2$  and  $\text{NO}_2$  data were obtained on a 10 inch Moseley recorder.

A typical set of SO<sub>2</sub> profiles from the Moseley recorder is shown in Figure 19. The upper trace is typical of sky signature with perhaps a small amount of SO<sub>2</sub> present. This was obtained early in the flight (1000 CST) at a time when substantial cloud cover was still present. The double peak was produced by scanning back and forth over the sky profile between the limits indicated by the dotted lines in Figure 7. Filling-in of the trough between the peaks and increase in the peak-to-peak values at the grating reversal points is indicative of increased SO<sub>2</sub> absorption as shown also in Figure 7. Disregarding dilution, the amount of SO<sub>2</sub> present in the sensors field of view, relative to that in the background (upper) waveforms, is determined by measuring the increase in peak-to-peak amplitude at the grating reversal points, that is at the mid-point of the +ve and -ve swings. The incremental sensitivity of the instrument is given by the increase in the peak-to-peak value using a reference cell of known SO<sub>2</sub> content. The lower trace shows the effect of inserting 55 ppm-meters of SO<sub>2</sub> in the instrument's field of view.

Figure 20 shows typical waveforms from the NO<sub>2</sub> sensor. As mentioned earlier the quantity of NO<sub>2</sub> detected by the instrument is determined by measuring the maximum peak-to-peak amplitude of the waveform. Here again the contribution of an NO<sub>2</sub> cloud is measured relative to a minimum gas waveform obtained at some point in the flight. The abrupt increase in peak-to-peak value evident in Figure 20 is the result of inserting a reference cell of 132 ppm-meters.

Figure 21 shows the balloon trajectory and the route of a station wagon carrying an upward-looking SO<sub>2</sub> sensor. The circuitous track of the balloon was completely unexpected although the south-westerly and north-westerly position of the trajectory were anticipated. Unfortunately, as previously mentioned, variable cloud covered much of the track. Under the influence of a light (7 knot) easterly wind and strong inversion conditions the ground level SO<sub>2</sub> levels were somewhat higher than usual as shown by the ground station readings in Figure 22. These values are for 1215 CST and were obtained from the automated pollution monitoring network of the city of Chicago. The station wagon followed a route which was intended to approximate the predicted east-to-west balloon trajectory (as far as Joliet). The station wagon had reached Joliet when advised of the balloon's change in direction and immediately turned back to intercept the balloon's ground track in the center of Chicago.

When the balloon was approaching South Chicago the city's Department of Air Pollution Control was notified and the sampling network was immediately switched from the normal 15 minute sample rate to a 5 minute rate.

Figure 23 shows several samples of the station wagon record. These traces, which read from right to left in time, shows a number of extremely large responses obtained as the station wagon passed under SO<sub>2</sub> plumes as it sped along the highway. It should be noted that the correlation spectrometer has inherently greater sensitivity and better resolution in the upward scanning mode as used in ground traverses than in the downward looking mode as used in aircraft and balloons because of the greatly reduced scattering and dilution. In Figure 23 the characteristic double peak does not appear over much of the trace because of the high gas burdens. This effect is also evident in Figure 7. Figure 24 shows the station wagon installation.

## Section 7

### METEOROLOGY OVER CHICAGO

A study of the cloud formations and weather conditions at the time of the balloon flight was conducted by the National Center for Atmospheric Research and is reproduced here in its entirety with the exception of the large thermodynamic diagrams identified as Figures 6, 7, 8, 9, and 10. Copies of these figures can be obtained if desired from NCAR or Barringer Research.

### CLOUDS AND WEATHER IN THE VICINITY OF CHICAGO ILL. NCAR - SEPT. 3, 1969

This brief informal summary is for the purpose of providing cloud and other weather information relative to the flight of Barringer Research, Inc. experimental equipment on a balloon on September 3, 1969.

Hourly reports from Madison and Milwaukee in Wisconsin; Muskegon, Grand Rapids, and Lansing in Michigan; South Bend, Fort Wayne and Grissom Air Force Base in Indiana; and Cahnute Air Force Base, Rockford and Chicago (O'Hare and Midway Airports) in Illinois were all studied carefully. Figures 7.3 to 7.5 show analyses of part of this data.

The radiosonde data from Green Bay, Wisconsin; Flint, Michigan; Dayton, Ohio; Peoria, Illinois and Midway Airport (Chicago), Illinois were also plotted and studied carefully. The radiosonde sounding from Midway was a detailed sounding to 700 mb (3Km); the others were standard soundings. Figures 6 - 11 are plots of the soundings, showing also analysis and comments.

Several photographs of the clouds taken from satellites were also available. Three of these were taken from ESSA 8.\* Two were taken on Orbit 3288. The time on Photo # 1 appears to be correct, but the time on photo #2 should be about 5 to 6 minutes later. Terrain features (outlines of the Great Lakes) are not done very accurately on one or both of these since cloud features referred to terrain features indicate impossibly large cloud movements. Neither of them can be

\* See end of Section 7 (page 30).

correlated satisfactorily with the surface cloud observations available on the hourly reports studied. They do, however, show cloud patterns which can be identified on a photograph taken at 1051 CST on the next orbit of ESSA 8, indicating a fair degree of permanence of certain cloud formations. These patterns are also shown with greater resolution on a photo taken at 10:40 CST by the NIMBUS 3 satellite. The NIMBUS photograph Figure 7.2 was selected, therefore, for further study.

Perhaps those more expert in the analysis of satellite cloud photos could determine the types of clouds directly from the photo. Further I could not be certain how well the terrain features were placed. Therefore on the basis of reports from the Winzen pilot, who was tracking the balloon, that only scattered cirrus were observed over southern Lake Michigan, and that the lower clouds consisted of two layers - a low layer of stratus and a layer of cumulus whose tops extended up to approximately 3 Km - I was convinced that the most significant cloud features should move with (be advected by) the low level winds. These winds were east winds with speeds generally below 10 knots. The cloud features should therefore be moving slowly westward. Winds above 3 Km were west winds and would have carried the clouds to the east. The single most significant observation shown in the hourly data appeared to be the "Total Opaque Sky Cover". It is a number varying from 0 to 10 and is the amount of the sky covered by opaque clouds averaged over an hour. This variable was plotted versus time for most of the stations for which hourly data were available. See Figure 7.1. A smooth curve was drawn through the point to show the trend of cloudiness. A bar graph would present the data more precisely, but would not serve the purpose quite so well.

Assuming that the clouds would be readily visible on the photo when 6 tenths or more of the sky was covered and much less visible when less than 6 tenths was covered, the graph for each station was divided into cloudy and not cloudy sections. The cloudy sections are shaded red. Assuming that each of these cloudy sections is moving westward at 8 knots permits one to place them on the map either east or west of the observing station at any particular time. It also tells one approximately how far they are from the station. This is shown in detail for Muskegon, Michigan on Figure 7.1 for the time of the NIMBUS photo (Figure 7.2).

The cloud patterns were undoubtedly changing during the day as well as advecting with the wind. Trying to deduce patterns much beyond 2 hours probably would not be very productive even though adjustments could be made to the pattern to make it fit the observed hourly data. Observations are too far apart.

What I can say about the total amount of cloudiness for the period of greatest interest is summarized by Figure 7.1 through 7.5. By studying the vertical distribution of temperature, humidity and wind, one can get some general ideas also about the vertical distribution of pollutants.

A special sounding was made at Chicago Midway at 1000 CST. It has been plotted on a thermodynamic diagram as Figure 6. I have made some comments on the chart. Soundings at the standard observation times 1200 Z September 3 and 0000 Z September 4 are plotted together from Dayton, Ohio as Figure 7 for Peoria, Illinois as Figure 8, from Green Bay, Wisconsin as Figure 9, and for Flint Michigan as Figure 10. Interpretations are also given on each of the figures, but I shall try to summarize here what I read from all of them.

The winds over the entire region were light easterly at the surface. At 3 Km (700 mb) the winds were southerly to westerly and at 5.5 Km (500 mb) they were generally southwest to west. The air was relatively more moist in the layer below 1.5 Km than in the layer above. This lowest layer gave evidence of being rather well mixed during the day although it was very stably stratified at the time of the 031200 Z (0600 CST) sounding (the blue curve on Figures 7 through 10).

During the early morning any pollutant released into the atmosphere near the surface would be trapped near the surface unless its density were considerably less than that of the atmosphere. As the sun rose higher and surface temperatures increased, surface air was mixed through a deeper layer and gaseous pollutants would have been distributed through that layer. It seems unlikely to me that new pollutants would penetrate to the top of the low cloud layer as long as that

layer remained unbroken, but as the mixed layer deepened to include the low cloud layer, the clouds would tend to breakup. Deeper cumulus might then develop, and these could easily reach above 3 Km at Chicago, Dayton and Peoria but not at Flint and Green Bay. To reach great heights, however, the individual cumulus cells would have had to have horizontal dimensions of 2-3Km. In smaller cells the moist air from the mixed layer would have been too diluted by the dry air above to develop to great height. No large cells were reported in the hourly data. My reaction then is that very little mixing of the lower air occurred with air above 1 to 1.5 Km over Chicago.

\* ESSA 8 Orbit No. 3288 (Photo #1) 14:57:13Z 03 Sept. 1969 52.7°N, 070.7°W  
ESSA 8 Orbit No. 3288 (Photo #2) 14:57:13Z 03 Sept. 1969 34.9°N, 079.7°W  
ESSA 8 Orbit No. 3289, 16:51:55Z 03 Sept. 1969  
NIMBUS 3 Orbit No. 1909, 16:40Z approx. 03 Sept. 1969  
Satellite Data Laboratory, Toronto International Airport

## PART II

### Section 8

#### DATA PLOTS

##### 8.1 STATION WAGON

Figure 25 shows a three-dimensional plot of the SO<sub>2</sub> burden measured by the station wagon. Note that the wagon route crosses the balloon ground track at two points; near ground station No. 23 where the wagon followed a detour to the north of Route 80 on the west bound leg and later the Chicago waterfront where the balloon left Chicago and floated out over the lake. The SO<sub>2</sub> levels were very low from the intersection of Routes 80/294 until the wagon reached a point just west of Joliet. At this point a strong signal (360 ppm-m) of short duration was recorded. A second signal of 725 ppm-m peak value was recorded after turning north on Route 55. From analysis of the wagon positions, chart profiles and wind direction, it was subsequently deduced that the wagon had measured the same plume twice as indicated in Figure 24. The identity of the industry south of Joliet has not yet been determined. The peak ppm-m value of the plume was not reached on the first pass because of the small size of the concentrated plume and the speed of the vehicle. Further north on Route 55 the wagon again recorded a very strong signal. This time the source was identified as the Romeoville Generating Station. This is a very large thermal plant whose SO<sub>2</sub> emissions are essentially uncontrolled. As the station wagon approached Chicago a substantial build-up of SO<sub>2</sub> was recorded. The origin of this was not determined but it was possibly due to the Calumet/State Line plume being carried westward by the easterly surface winds. Unfortunately, the major contributors to SO<sub>2</sub> pollution in the Chicago area; the Ridgehead, Crawford and Fisk Generating Stations were all downwind of the wagon route and no plumes were detected.

##### 8.2 BALLOON

The interpretation and reduction of remote sensor must be done with extreme care and with a comprehensive knowledge of not only the controlled but also the uncontrolled variables involved in the measurement. The criteria used for quantitative interpretation of the raw chart data are explained fully in reference (4). These criteria are basic to the computerized data reduction procedures described in paragraph 8.2.1 below.

### 8.2.1 COMPUTERIZED DATA REDUCTION

Four phases were required to process the analogue strip charts into computerized vector profiles. The first phase consisted of hand digitizing the following sections from the Chicago Aeronautical Charts:

- (a) flight path of balloon with annotated time values
- (b) station wagon path containing ground pollution instruments
- (c) shoreline of Lake Michigan
- (d) outline of Michigan City, Calumet, Stateline

This deck of punched cards formed the base map with the zero degree flight path annotated with some time values.

In the second phase, the spectrometer mirror angle position and wavelength scan interval from the six channel analogue chart were manually superimposed on the sulfur dioxide and nitrogen dioxide analogue charts. Both charts were separately digitized between 10:00 C.S.T. and 13:06 C.S.T. Every sample point in the sulfur dioxide contained the following information:

- (a) calibration interval?
- (b) no gas condition?
- (c) sample number
- (d) instrument malfunction?
- (e) actual mirror position--zero or twenty-four degrees
- (f) time value if annotated at scan on analogue chart
- (g) maximum and minimum value of scan

The nitrogen dioxide output contained similar information except that the "no gas condition" was replaced by a "lead or lag" waveform condition.

Phase three produced the magnetic plotting tape for phase four.

In the  $\text{NO}_2$  program, five subprograms at Fortran V level were used in the third phase, to compute a vector PPM-M value with a corresponding X and Y co-ordinate for each digitized sample. A Univac 1108 computer under control of an EXEC II

monitor system was used for the compilation. The first subprogram did a linear time interpolation between each time interval annotated on the output chart, to obtain a real time value for each sample. The second program interpolated a X and Y co-ordinate for each sample by using the time annotated co-ordinates of the digitized flight path of phase one. The third subprogram calculated the angle between the positive X axis and normal to the flight path at each data point. This angle was required to plot the vector PPM-M value normal to the flight path for the zero degree mirror condition. The fourth subprogram computed the magnitude of PPM-M value using a different set of equations for each of the four different conditions:

- (a) twenty-four degree mirror position, "lag" waveform
- (b) twenty-four degree mirror position "lead" waveform
- (c) zero degree mirror position, "lag" waveform
- (d) zero degree mirror position, "lead" waveform

The final program calculated the X and Y co-ordinates for the theoretical twenty-four degree flight path. Using time as a common parameter, a sun angle "theta" for each sample point was computed between the given azimuth angles from charts of the Nautical Almanac Office. The incremental distance between the zero degree flight path and the twenty-four degree flight path was determined using a mean balloon altitude of 113,000 feet and a spectrometer mirror angle of twenty-four degrees. The combination of the incremental distance and the angle "theta" at each sample created a new X and Y co-ordinate for the theoretical flight path.

The SO<sub>2</sub> program for phase three was basically the same as above except the "lead and lag" waveform condition was replaced by the "no gas condition". This resulted in a more simplified program.

The final program combined the base map of phase one and the vector PPM-M value of phase three to produce four different plots:

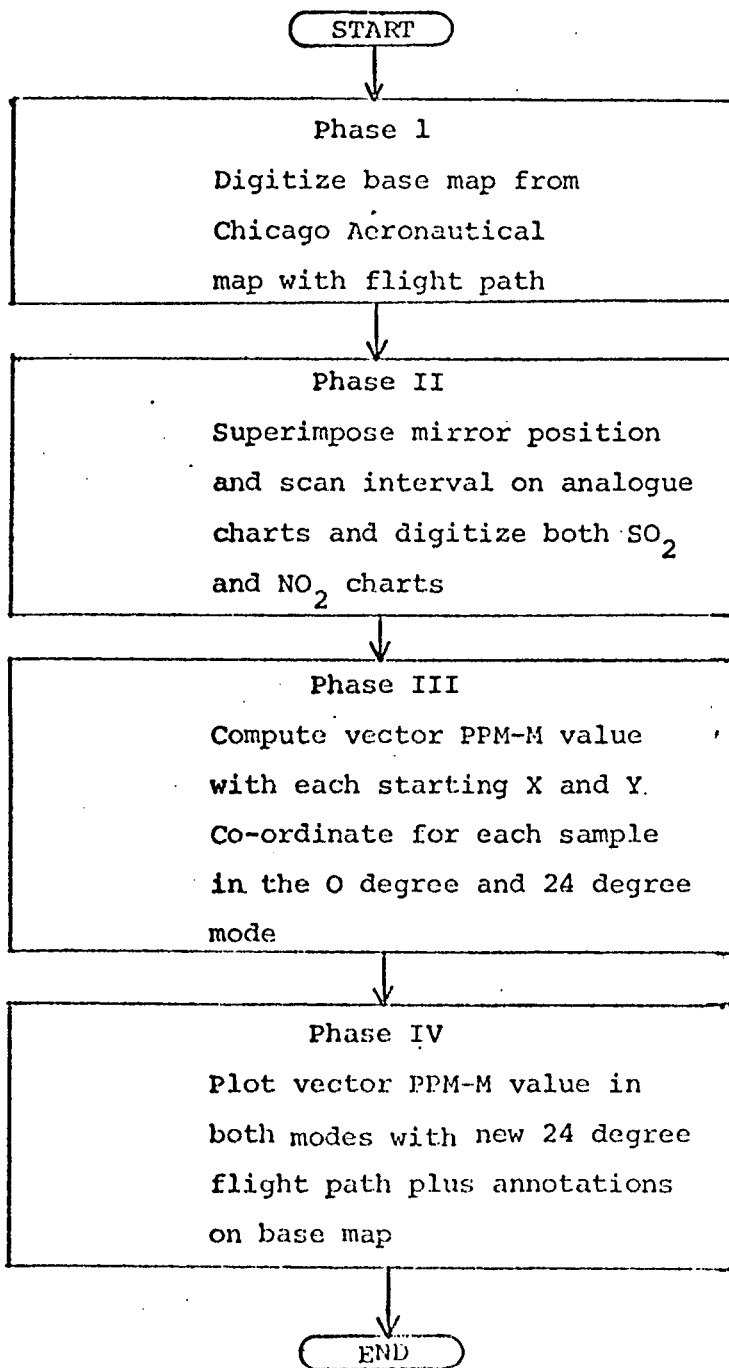
- (a) NO<sub>2</sub> zero degree profile
- (b) NO<sub>2</sub> twenty-four degree profile
- (c) SO<sub>2</sub> zero degree profile
- (d) SO<sub>2</sub> twenty-four degree profile

Various Calcomp subroutines annotated the profiles with appropriate labelling and scales. An off-line Calcomp 760 magnetic plotting system consisting of a Calcomp 760 magnetic tape unit and a Calcomp model 663 incremental plotter did the actual plotting.

Problems During Data Reduction:

- (1) The existence of negative PPM-M values were attributed to the cloud cover. These values were brought to a zero level during phase three.
- (2) The manual positioning of the mirror angle position and wavelength scan from the six channel chart to the NO<sub>2</sub> and SO<sub>2</sub> charts produced some human error because of the uncertainty during transistion period between each cycle.
- (3) Time annotated on the strip charts of NO<sub>2</sub> and SO<sub>2</sub> were not precise enough because error existed between some of these intervals.
- (4) Since the magnitude of the instrument offset and calibration, for the four conditions in the NO<sub>2</sub> case and for the two conditions in the SO<sub>2</sub> case, has a large influence on the magnitude of all the respective readings; these intervals should have been clearly marked on the chart during ideal conditions (with no clouds and around 12:00 C.S.T.).
- (5) The mirror flipping during the wavelength scan interval produced some zero readings in the PPM-M values.

FLOW CHART



### 8.2.2 SO<sub>2</sub>/NO<sub>2</sub> VECTOR PLOTS

Figure 26 shows the computerized plot of the balloon SO<sub>2</sub> spectrometer output signals. Note that the SO<sub>2</sub> responses obtained are shown plotted as discrete values on a base line which is the ground track of the remote sensor's field of view when the scanning mirror was in the 24° position. This base line is referred to as the "24° scan line". The gradual convergence of the 24° scan line and the balloon ground track with time is due to the gondola's solar tracking system which maintained the plane of the mirror scan angle in alignment with the sun's azimuth position. The measurements are shown as discrete values rather than as a continuous analog signal since the motion of the grating is continuous, except at the reversal points. As noted in Section 3 the amount, or burden of the SO<sub>2</sub> sensed is determined by the peak-to-peak amplitude of the trace taken at the reversal points. Each cycle of the grating yields two discrete measurements. In the case of NO<sub>2</sub>, two measurements are also obtained for each grating scan, one from the peak-to-peak deflection during clockwise rotation of the grating and a second from the peak-to-peak deflection during the counter-clockwise rotation.

The SO<sub>2</sub> plots in Figure 26 show no SO<sub>2</sub> responses early in the flight with some measurements obtained between 1015 and 1052 CST. A gap in the data occurs between about 1052 and 1145 CST followed by maximum SO<sub>2</sub> responses diminishing again to zero at 1330 CST.

Figure 27 shows similar data for the 0° scan line which corresponds to the balloon ground track. The NO<sub>2</sub> profile obtained along the 24° scan line is shown in Figure 28. The reason for the NO<sub>2</sub> data occurring in sets of two is due to the time sharing between the zero degree and twenty-four degree scan positions. The wind data shows surface conditions present at 1215 CST on September 3, 1969.

Figure 29 shows the corresponding NO<sub>2</sub> 0° scan line case.

## Section 9

### DISCUSSION OF RESULTS

The greatest challenge in successful development of remote sensor technology lies in the interpretation of the data obtained. The best interpretation, however, is only as good as the information available. In the balloon experiment described herein the interpretation was severely handicapped because of sparse information regarding the cloud conditions below the balloon. Without photographic coverage it is impossible to say with certainty whether the sensors saw the ground at any specific time. However, it is quite clear from the information available, particularly from the excellent meteorological analysis, that the sensors view of the ground was not continuously blocked by cloud and after 1200 CST the sensors could see the ground most of the time.

Referring again to Figures 26 and 27, note that no SO<sub>2</sub> data are shown before about 1015 CST. The reason for this is due to initial light-limiting conditions followed by instrument calibrations and adjustments up until about 925 CST. After 925 CST and before 1015 CST the SO<sub>2</sub> burden measured was negligible probably because of both cloud cover and low SO<sub>2</sub> burdens. As the balloon moved northward after 1015 CST, significant levels of SO<sub>2</sub> were recorded but only sporadically. The most likely reason, although it cannot be confirmed, is that the sensor could see the ground and hence the SO<sub>2</sub> layer only a fraction of the time because of intermittent cloud cover as discussed in Section 7 and as shown in Figures 7.3, 7.4 and 7.5.

The large gap in the data between 1052 and 1145 CST is due to a series of calibrations and adjustments made to the SO<sub>2</sub> sensor via the telecommand link. The time required to perform in-flight calibrations was considerably greater than anticipated and some data were lost because the sensor was not adjusted correctly. The rather excessive time required for calibrations was a consequence of the eleven position unidirectional rotary solenoids used for sensor adjustment. Specifically, when checking the sensor performance using the on-board reference source the magnitude of the offset compensation required was quite large because of marked differences in spectral gradient of the on-board reference lamp and the solar irradiance and the

number of commands i.e. solenoid steps involved in changing from the solar source to the reference source and back again was considerable. Thirty minutes worth of SO<sub>2</sub> data was lost when the system was maladjusted unknowingly. This occurred immediately following a reference source calibration and was caused by a large uncompensated gradient offset which resulted in operation near the edge of the telemetry band and a rather distorted and inverted SO<sub>2</sub> signal\*. This was subsequently corrected by stepping back into the mid-portion of the telemetry dynamic range. This condition was not immediately recognized because it had never been observed on any previous ground tests. It was also unexpected because zener diodes had been installed during the integration test phase to prevent such effects from occurring due to over loading of the telemetry discriminators. Another factor in the yield of useful data was the time sharing between the 0° and 24° mirror positions. The interval of time that the mirror spent in each position was adjusted, prior to the flight, to comfortably exceed the period of the grating oscillation i.e. about 100 seconds, in order to obtain at least one gas measurement for each "flip" of the mirror. If the mirror changed position between two measurement points on the trace then the measurement between these points was discarded.

The surprisingly large readings obtained over the lake cannot be pollution generated recently by Chicago because the NCAR analysis (Section 7) concludes that there was very little vertical mixing at 1 to 1.5 Km altitude and the surface winds were easterly. However the Meigs Field weather station at the waterfront reported fog haze and smoke and the Winzen pilot reported no clouds, only haze and smoke over the lake at 1320 CST. Another point worth noting is that the weather data shows the wind vector rotates with altitude from easterly at ground level to southerly and westerly at 10,000 feet. (Section 7) The SO<sub>2</sub> detected could perhaps be pollutant from previous days emissions moving eastward at 10,000 ft. or higher.

Plots of the NO<sub>2</sub> data are shown in Figures 28 and 20. Interpretation of these data is less certain than in the SO<sub>2</sub> case for two reasons viz (1) the maximum NO<sub>2</sub> responses were recorded when the sensor saw the ground only a fraction of the time as indicated by the cloud structure of Figure 7.4 (note balloon track is plotted in CDT in Figure 7.4) and (2) the criteria for NO<sub>2</sub> data interpretation is less positive

\*Winzen Research recently conducted laboratory tests of the same telemetry equipment and demonstrated that although non linearities do result from over-driving the VCO discrimination link, the signal is not inverted. The reason for the apparent signal inversion is therefore unknown at this time.

than for SO<sub>2</sub> as explained in reference (4). The very large Fraunhoffer background signal resulting from the particular mask design used in the experiment made the relatively small NO<sub>2</sub> contributions difficult to discern and without photographic data the possibility of causes other than NO<sub>2</sub> e.g. cloud or ground reflectance changes, giving the responses graphed in Figures 28 and 29 should not be discounted.

In spite of the uncertainties discussed above a very significant point worth noting in Figures 26 through 29 is the fact that maximum SO<sub>2</sub> responses were recorded in the vicinity of strongest emissions along the ground track. In Figure 26 maximum values are recorded at 1045 and 1200 CST which correspond in their location to high ground level readings. In Figure 27 the maximum value of 24 ppm-meters of SO<sub>2</sub> was obtained immediately downwind of the Calumet and State line Generating Stations which have a combined output of 80,622 tons of SO<sub>2</sub> annually. This also agrees with the maximum ground level measurement of 0.28 ppm at ground sampling site No. 6.

For the NO<sub>2</sub> plots of Figures 28 and 29 the sensor responses showed pronounced anomalies in the interval 1115 to 1145 CST on both the 24° and 0° scan lines. Ignoring the uncertainty introduced by the cloud formation for the moment it would appear that the NO<sub>2</sub> sensor saw very substantial and rather well defined NO<sub>2</sub> gas clouds located near sampling sites No.'s 8 and 24. Although the NO<sub>2</sub> or potential NO<sub>2</sub> (NO) output of the Calumet and State Line generating stations is not known, the combined plume from these sources would appear to be the most likely origin of the NO<sub>2</sub> signals. Note that in Figure 26 the SO<sub>2</sub> level measured at sampling site No. 8 is 0.20 ppm and in Figure 25 a broadly dispersed plume of SO<sub>2</sub> was recorded by the station wagon on returning from Joliet along highway 55. These facts, plus the recorded tendency of the wind vectors to rotate clockwise from south to north Chicago, suggest that the Calumet-State Line plume followed a southwest path from the stacks to about site 24 and then turned northwest over site 8 and crossed Highway 55 near the 55/294 intersection. The known presence of cloud without photographic detail makes this analysis impossible to confirm unfortunately. The recording of significant levels of NO<sub>2</sub> before 1052 CST in Figures 28 and 29 could be due to effluent from the heavily industrialized areas around Gary, Indiana.

As stated in Section 2 the purpose of the station-wagon traverse was to provide a measure of dilution for the balloon SO<sub>2</sub> measurement. From the foregoing it is apparent that time and space-coincident upward and downward looking measurements were not achieved however, a crude first approximation of the dilution factor is possible by comparing the nearest balloon and station wagon values with the City of Chicago ground level measurement at sampling site 23. The nearest corresponding balloon value is a solitary measurement of 12 ppm-meters just slightly north and downwind of station 23 (in Figure 27) and the most appropriate station-wagon value is directly downwind of station 23 (Figure 25). The readings and times taken are as follows:

Chicago monitoring site	1120 CST	0.12 ppm
Barringer station wagon	1206 CST	135 ppm-m
Balloon	1148 CST	11.5 ppm-m

The Chicago reading for 1120 CST was taken to allow for a transport time of about 15 minutes between the site and the balloon track.

If we now assume the thickness of the mixing layer is between 1000 and 1500 meters as concluded in Section 7, and the gases in the pollutant layer are uniformly distributed through the layer, then the Chicago monitor indicates a total vertical burden of 120 to 180 ppm-meters. Also at Chicago's coordinates, the sun's zenith angle at 1200 CST on Sept. 3, 1969 was 34.2°. In accordance with references (2) and (3) the multi-path "m" factor for this sun angle, assuming a homogeneous layer, is approximately 2.46. Now with no dilution the balloon sensor response should be 120 to 180 times the "m" factor or 295 to 443 ppm-meters. With a balloon sensor result of 11.5 ppm-meters this yields a dilution factor of 26 to 39. These results, including a dilution factor based on the station wagon reading, may be summarized as follows:

Method of Measurement	Vertical Burden SO <sub>2</sub> (ppm-meters)	Dilution Factor
Chicago monitor	120 to 180	26 to 39
Station wagon	135	29
Balloon	11.5	-

The agreement between the vertical burden as measured by the upward looking SO<sub>2</sub> sensor and the Chicago monitor value multiplied by the estimated mixing depth is surprisingly good considering the approximations made. The dilution factor using the upward-looking sensor reading should be the most accurate. Theoretical estimates of the SO<sub>2</sub> dilution factor are 2 to 3 times larger than the value of 29 shown above. With only a single set of readings to work with this result is obviously not very conclusive but its determination nevertheless represents an interesting and perhaps very useful first approximation of a dilution factor measurement from above the atmosphere.

Considering now briefly the radiometer data of Figures 17 and 18, note that the frequent limiting or saturation of the radiometer UV (in  $\emptyset$ ) channel shows that the actual contrast in the ultraviolet or terrain and/or clouds features as observed from space was higher than expected. The original design parameters for the contrast measuring circuits was based on theoretical contrast values derived from references (1) and (7). Amplifier gains in both UV and visible channels were finally adjusted during the integration phase at Winzen Research based on actual contrast measurements using outdoor scenes and theoretical dilution estimates. The fact that the UV (in  $\emptyset$ ) shows saturating levels of contrast over much of the flight indicates that the adjustment for increase in gain to compensate for "washing-out" of the signal due to dilution was rather excessive.

The radiometer UV (90°) signal was limiting or saturated throughout the flight. Since the circuit adjustment was made identical to that of the UV (in  $\emptyset$ ) channel and both were checked just prior to launch it must be assumed that a malfunction occurred during launch or climb-out. A normal signal from the UV (90°) channel would appear similar to the UV (in  $\emptyset$ ) signal. Since both quadrature components of the UV channel signal are required to derive the apparent contrast within the instrument's field of view the loss of UV (90°) data renders the balance of the radiometer data of limited usefulness.

An interesting feature of the UV (in  $\emptyset$ ) signal however, was its tendency to show low values of contrast during the flight with only occasional limiting (high contrast) until after 1000 CST when intervals of high contrast occurred about 50% of the time, increasing to 100% around 1200 CST. Again, without photographic data it cannot be confirmed but the most likely reason would appear to be the

cloud formation which obscured much of the sensor's view of the ground until shortly after 1200 CST when the balloon had passed over the cloud formation.

In retrospect it is perhaps worthwhile to review those areas of the program specifically in design and adjustment of the scientific payload, where significant compromises in performance had to be accepted in order to meet objectives of time and cost. These may be listed as follows:

- (1) Spectrometer photo detector design - The environmental tests revealed the basic unsuitability of the XP1000 series of photo-multiplier tubes in a near-space environment. Time did not permit replacement with a more suitable tube and the pressure tight housing modification proved not to be an entirely satisfactory alternative.
- (2) Correlation mask design. - The  $\text{SO}_2/\text{NO}_2$  masks were not optimized for Fraunhofer rejection because of shortness of time. The resulting performance in terms of sensor sensitivity was substantially less than what could have been achieved with more time.
- (3) Radiometer design, - Shortness of time prevented a more thorough ground testing of the instrument with a wider range of terrain features and contrast values.
- (4) The rotary stepping relay combined with the rather limited telecommand and telemetry systems was not a satisfactory method of making sensor adjustments. A more sophisticated arrangement was outside the scope of the program.
- (5) The bi-stable scanning mirror arrangement was not synchronized with either of the sensor grating scan mechanisms because of shortage of effort or time. The result was some loss of data.

- (6) Photographic data - With more time to perform a thorough check-out of the integrated balloon payload and telemetry system it is unlikely that a malfunctioning camera or distortion through the telemetry system would have occurred in flight.

## PART III

### Section 10

#### BACKGROUND

The close association of iodine with specific geological and biological regimes, its relatively high vapour pressure and its highly specific and intense light absorption characteristics make it particularly attractive as an atmospheric tracer for natural resource exploration and monitoring purposes. The iodine association with mineral deposits is believed to be due to the tendency of halogens to be concentrated in the ore-forming fluids. Studies of liquid inclusions in metalliferous ores and deep thermal brines carrying high metal contents both indicate the close connection between chlorides and other halogens in the ore forming processes. The iodine association with oil fields is attributed to the fact that oil is derived from marine organisms and marine life tends to concentrate iodine up to 100,000 times compared with the levels in sea water. For this reason the oil field brines, which are closely associated with accumulations of oil, are generally rich in iodine. The presence of the halogens in volcanic emanations, particularly flourine, chlorine and bromine is well documented.

The ratio of bromine to iodine in the products of volcanic out-gassing has been estimated to be 200:1 and that of chlorine to bromine to be 300:1. The development of instrumentation capable of remote sensing fumerole emissions in volcanically active regions of the earths surface would have obvious application in the monitoring of such activity from an airborne or space platform.

## Section 11

### PROGRAM OBJECTIVES & EXPERIMENTAL APPROACH

The objectives of the program may be stated briefly as follows:

- (1) Measure by means of correlation spectrometry,  $I_2$  emissions from at least three of the following types of geological sources; geothermal, sulphide ore, iodine ore and oil or natural gas. Wet chemical verifications is to be used whenever or wherever practical.
- (2) Establish the representativeness of the selected sources in terms of total world-wide complement of such sources.
- (3) Determine, in theoretical terms only, the feasibility of detecting and monitoring such  $I_2$  sources using an advanced correlation spectrometer for aircraft and spacecraft altitudes.
- (4) As a consequence of (1), (2) and (3) above, to establish the significance of atmospheric iodine as a geochemical tracer for earth resource inventory purposes.

Measurements at each of the three chosen sites will include horizontal (long path) measurements using a Xenon lamp both up-wind and down-wind of the source, or directly over the source, if it is distributed over a workable area, and vertical-look traverses using a moving vehicle and the sky as a source. Whereas the first type of measurement will yield accurate average concentrations, the second method will give the total mass flow of  $I_2$  generated within the selected target area. When and whenever practical measurements of atmospheric  $I_2$  will also be made using a wet chemical method and an appropriate number of rock and soil samples will be taken so as to verify as closely as possible, anomalous  $I_2$  concentrations detected by the spectrometer.

The essential measurements and/or instruments required for the program are as follows:

- (1) Long path sensor and Xenon light source
- (2) Distance measurement (stadimetric or geodetic)
- (3) Wind measurement (anemometer tripod)
- (4) Vehicle velocity (speedometer)
- (5) Temperature, barometric pressure and humidity
- (6) Wet chemistry, air and soil sampling equipment

Section 12

SITE SELECTION

The following test sites were selected after due consideration of geological significance, potential source strength, season and weather factors and logistic support.

- (1) sulphide ore - Ajo, Ray or Bisbee all in southern Arizona
- (2) oil - Bakersfield, California
- (3) geothermal - Geyserville, California (steam field)

## Section 13

### INSTRUMENT MODIFICATION & REFURBISHMENT

The following is a fairly complete description of the modification and testing required to convert the Balloon NO<sub>2</sub> sensor to a portable weatherproof I<sub>2</sub> sensor capable of both remote sensing using sky light and long path operation using a modulated artificial source.

Strip, clean, re-assemble and modify balloon NO<sub>2</sub> spectrometer for I<sub>2</sub> to include; new refractor plates, new entrance slit, two new masks (one for lamp and one for sky) additional mask holder, new spherical field lens and holder, fabricate I<sub>2</sub> reference cells and insertion device, modify grating scanner for no-slips, new folding mirror mount, 6000 Å grating, stop down primary mirror, install adjustable shutter, modify voltage regulator and mount on sensor, manufacture light-tight housing suitable for rugged outdoor use on tripod, install boresighting telescope, re-build electronics as required for dual operation, (sky and lamp) and optimize filtering for new lamp p.r.f., realign and refocus optics and evaluate performance on artificial point source, optimize focus for minimum signal offset over selected wavelength region, optimize grating scan speed for both lamp and sky, establish required I<sub>2</sub> reference cell heater current and prove constancy of cell I<sub>2</sub> level. Check out complete system outdoors over 200 to 1,000 meters. Since the sensor acceptance angle is only 1.25 mr the heavy duty tripod will be necessary. The PM tube used should be XP1002 (S20) or XP1003 (extended S20).

## Section 14

### FIELD TESTS RESULTS

#### 14.1 PORPHYRY COPPER DEPOSITS

The  $I_2$  field party was mobilized to Phoenix, Arizona in the latter half of March. During the last week of March and the first week of April two preliminary tests were made over Kennecott's porphyry copper open pit at Ray and the Phelps Dodge open pit at Bisbee. Both of these tests failed to detect  $I_2$  vapours but provided useful field experience for more comprehensive measurements at the Duval Sierrita porphyry copper pit near Twin Buttes, Arizona. The change in test site location from Ray to Bisbee to Sierrita was designed to improve the prospects of detecting anomalous levels of  $I_2$ . The Ray pit forms part of a large natural canyon system which characteristically on occasions conducts smelter effluent into the pit from the copper smelter at Hayden and because of the irregular topography, made atmospheric measurements difficult and severely limited the mobility of the field team.

The Bisbee pit was ideally suited for long path measurements but no  $I_2$  vapour was detected. The reasons for this were attributed to one or a combination of the following reasons:

- (1) The  $I_2$  concentrations were below the threshold sensitivity of the sensor.
- (2) The Bisbee pit is a relatively old working with about one year of economic life remaining, therefore if the oxidation of the ore and the liberation of free  $I_2$  occurs preferentially at the near-surface zones of the ore body then the probability of detecting anomalous levels of  $I_2$  over Bisbee might be lower than expected.

(3) Porphyry copper does not emit  $I_2$  vapours in anomalous quantities.

A decision was made to try a third porphyry copper deposit, namely the Duval Sierrita pit in order to try to answer the questions raised above.

The Sierrita pit is a new development, stripping of the overburden is still in progress and the production mining of ore has only begun to approach full scale.

Preparations were also made to install a modification in the spectrometer which would enhance its performance. This involved a special timing circuit which would reduce the amount of lost time between peak position of the grating and reduce the undesired Fraunhofer signal component.

Figure 30 shows the Sierrita pit with three different long path set ups. The sensor was set up on a high ledge on the eastern side of the pit. Figures 31 and 32 were taken at this location. The set-up of Figure 31 was used for zero path length calibrations of the spectrometer. The truck was used to facilitate tests with the exclusion of direct sunlight. The Zenon light source is shown illuminating a brushed aluminum reflector to provide a diffused source of light for the spectrometer. The 1142 meter path was used for the majority of measurements over the pit. During long path monitoring the wet-chemical measurements of atmospheric  $I_2$  were generally taken as close to the optical path as practicable. The 915 meter set up was used for background measurements on occasions when the winds were westerly. Soil and rock samples were taken outside the pit on two traverses C and S as shown.

Figure 32 shows details of pit geology and the soil sample locations in the pit. Atmospheric samples are denoted as CA. The procedures used for  $I_2$  analyses of the soil and air samples are given in Section 14.5.

The first data run was made using the long path configuration over the 1142 meter path on April 7th/70. Figure 34(1) is typical of the data obtained. This profile was produced by scanning the grating at a constant angular rate back and forth between two preset limits. The response of the instrument to the sensor's internal calibration cell is shown near the right hand end of the trace. The measure of  $I_2$  seen by the sensor is represented by the peak to peak value of the trace as taken between two adjacent positions of grating reversal. These points are located from

the steps in the fiducial marker trace that runs along the bottom of the chart. The magnitude of the peak to peak deflections is converted to ppm-meters of  $I_2$  by reference to the calibration cell response. The cell was charged with sufficient solid  $I_2$  to maintain a vapour-to-solid equilibrium condition under all anticipated instrument temperatures. From Figure 35 the vapour pressure of  $I_2$  for several temperatures was used to draw Figure 35 which gives the calibration cell burden in ppm-meters for a known temperature. The sensor's internal cell is fused silica of 10 mm optical length. In Figure 34(1) for example the maximum response from the cell plus atmospheric burden was 68 minor divisions. With an atmospheric or long path burden of some 8 minor divisions just before insertion, the cell alone produced 60 divisions with a cell value of 8.5 ppm-meters at 32°C cell temperature. Incremental sensitivity of the sensor was then  $8.5/6 = 1.4$  ppm-meters per major division. In a path length of 1142 meters this gives an average sensitivity (or chart scale) over the path of 1.23 ppb per major division. As indicated by the peak-to-peak values noted along the base of the chart, the  $I_2$  burden varied over the period of the run from zero divisions to a maximum of 21 minor divisions i.e. zero  $I_2$  to a maximum of about 2.6 ppb (by volume). The modification to the sensor previously mentioned was then installed and the measurement repeated two days later. No  $I_2$  was detected on either the 1142 meter path or the 2095 meter path. On April 13th measurements were again made over the 1142 meter path after careful calibration of the instrument. Figure 34(2) is a sample of the raw data. Note that with the modification to the sensor the grating scanned rapidly from one limit to the other in square wave fashion with a dwell time at each limit corresponding to maximum +ve and -ve correlations. The fiducial trace then indicates the dwell in each position. In Figure 34(2) the reference cell gave a positive deflection for position 7843 relative to 7840.8 (plus a mean value offset) which was reversed in phase when the cell was withdrawn. This condition was not persistent but occurred frequently enough to warrant investigating the possibility of interference from a competing absorber.

A quasi first derivative of spectra may be obtained with the correlation spectrometer by using only one slit in the correlation mask. Figure 34(3) is the single slit scan of the Xe source alone at zero path length with the grating scanning at a constant rate back and forth from 5305 Å to 5450 Å. The distortions in the zero gas line

are the results of emission spikes in the Xe continuum. Figure 34(1) shows the response from an external 50 mm calibration cell (42 ppm-meters) with a 915 meter background. A similar setup over the pit failed to show distinctive spectral signatures and the scan limits were extended to cover the entire  $I_2$  spectra from 5150 Å to 6060 Å. Figure 37 shows the grating wave length/position counter calibration. Figure 38 (1) shows a single slit scan on the Xe source with only 1 sec. integration time. Figure 37(2) is similar but with 330 ppm-m of Bromine in the external cell. Figure 38 (3) shows the entire  $I_2$  derivative spectrum. Note the sensor's sensitivity to  $I_2$  is some 200 to 300 times greater than its sensitivity to Bromine. Figure 38 (4) shows a typical single slit scan over the pit. Comparisons of the traces above shows no obvious correlation with either the iodine or bromine signatures except between counter 7800 and 7820. Both iodine and bromine are inphase in this range.

Simultaneous with the spectrometer measurements whenever practical wet chemical measurements of atmospheric  $I_2$  were made using both the specific ion electrode method and the more specific catalytic method. The results of these tests are discussed later in the report (Section 15).

Wind speed and direction were also recorded at frequent intervals along with temperature and humidity. Barometric pressure records were also obtained. Generally, the humidity was below 10% for the entire period at Sierrita and the barometric pressure remained constant within the resolution of the barometer (0.02" Hg) over the duration of a testing period. On April 15th the spectrometer was mounted in the station wagon with a 45° mirror for a sky-look traverse in the passive mode. A traverse was run from the Harrison ranch through the open pit to approximately 10 miles east of the pit. No anomalies were recorded. The system noise level in the passive mode was approximately 0.3 ppm-meters. On April 25th the field team left Sierrita and operations began in oil fields near Bakersfield California the following week.

#### 14.2 OIL FIELDS

With the assistance of the USGS field office in Bakersfield the large Midway Sunset field was selected for the test program. This field was chosen primarily because

of its size and productivity and because of its extended outcropping along the western edge. Midway Sunset lies on the eastern slopes of the Temblor range which is part of the coastal range system which forms the western limits of the San Joaquin Valley. The wells in this area vary in depth from several hundred to many thousands of feet depending roughly on their distance from the outcropping. Midway Sunset contains some 6,000 wells of which about one third are now productive. Arrangements were made with the principle oil companies in the field to carry out the tests. Companies contacted were as follows: Union Oil Company, Signal Oil Company, Standard Oil Company of California and Chanslor-Western Oil and Development Company. Figure 39 shows the topography of the area and the test locations and the soil sample traverses. Figure 40 shows the geology and Figure 41 the mineralogy and test locations.

To obtain a background reference reading of atmospheric  $I_2$ , measurements were made in virgin cattle country approximately 20 miles northwest of McKittrick. This is approximately 25 miles northwest of the Midway Sunset field. The single slit scan technique was used for these background measurements, atmospheric conditions were near ideal, instrument system pathlength was 1,000 meters, and the system noise level was less than 1 ppm-meter. No significant levels of Iodine were detected above the noise level of the instrument nor was there present any other interferer of measurable quantities. Measurements were then made in the middle of the Midway Sunset field using a single slit. Again the pathlength was 1000 meters. Figure 42 shows representative records. Note that whereas Figure 42(3) shows very little structure, scan No. 2 Figure 42(4) shows a fairly definite but weak  $I_2$  signal. This has been estimated to be 1-2 ppm (by vol). Figure 43 shows a portion of the map detailing the soil sample locations for traverses R and Q. The sensor was then converted to the passive mode of operation with the full 12 slit mask and the square wave grating drive.

Preliminary scans over the horizon sky across the oil field showed encouraging anomalous levels. The noise level in the measurement was, for these measurements, 0.3 ppm-meters. A number of passive mode panoramic scans were made over the oil fields from the Telephone Hills region in the northwest corner of Midway Sunset and also from the top of Midway Peak. Midway Peak is a mountain top approximately 3,000 feet above the elevation of the oil field and approximately 3 1/2 miles to the west of Midway Peak which demonstrated quite good anomalous levels of Iodine. Maximum measures of Iodine were obtained on the downwind side of the oil field. A limited scan was also done with the instrument pointing down  $10^{\circ}$  into the center of the oil field and scanning slowly from north to south. A very substantial anomaly was obtained with the maximum value being approximately 5 ppm-meters. Figure 44 shows a sample of the panoramic scan chart record in this case for  $10^{\circ}$  look-down. The sensors was stepped around at  $20^{\circ}$  intervals and a peak value obtained for each of the maximum correlation positions. The negative-going spike between each pair of measurements is due to Fraunhofer and the slow rotation speed of the grating relative to the sensor response time. Note that the maximum response was obtained at  $100^{\circ}$  from magnetic north. The noise level is the small fluctuation on the crest of each cycle. With an incremental sensitivity of 0.1 ppm-meters/minor division this represents a system noise level of about 0.3 ppm-meters. Note also that in the passive mode the data cannot, at this stage of the technology, be interpreted in absolute terms, therefore the passive mode is useful only in measuring differences in total burden. In Figure 44 a change of 46 divisions occurs in the peak-to-peak values from  $0^{\circ}$  to  $100^{\circ}$  or a positive change of 4.6 ppm-meters.

Figure 45 shows a polar plot of the  $0^{\circ}$  depression angle data. These are shown relative to the lowest value obtained at  $310^{\circ}$  which was set equal to zero. The max response of 4.7 ppm-meters was obtained at  $160^{\circ}$  as compared with an increase of 4.6 ppm-meters from  $0^{\circ}$  to  $100^{\circ}$  when looking directly into the oil field at a depression angle of  $10^{\circ}$ .

Immediately following the Midway peak tests the field team moved to the steam geyser area near Santa Rosa, California.

### 14.3 GEOTHERMAL EMISSIONS

Arrangements were made with Mobile Oil and the Pacific Gas and Electric Company to measure iodine emissions from the fumaroles and gas and steam wells in the Geyserville area. These natural steam geysers and steam wells occur in a small canyon in the remote northeast corner of Sonoma County. Figure 46 shows the test location and the soil sample sites. This field is presently being developed for geothermal electrical power generation and installed turbine capacity now exceeds 58,000 KW. The natural fumaroles have apparently diminished in intensity since the development of the steam wells and the only source of consequence is free-flowing steam well that cannot be harnessed.

A series of measurements were made over this plume from the well from positions below the plume and from positions along the rim of the canyon looking down on the plume. The maximum effective pathlength through the plume was judged to be about 30 meters. With a noise level of 0.5 ppm-meters the  $I_2$  concentration would have to exceed about 16 parts per million in the plume to be detectable. No iodine was detected in the plume.

The effluent from the turbines which comprise the natural non-condensable gases (primarily  $CO_2$ , methane, hydrogen, nitrogen,  $H_2S$  and ammonia) or else are monitored with the sensor but no  $I_2$  was detected. Here again the exhaust plume and hence the optical pathlength was very small. To detect  $I_2$  the concentration would have to be very substantial. It is evident that a more substantial geothermal source of greater aerial extent and hence pathlength is necessary to test the theory of significant and useful geothermal  $I_2$  emissions.

#### 14.4 WET CHEMICAL ANALYSES

An extensive literature search of the available analytical methods with suitable detection limit and precision was made on the basis of the published results. Two different wet chemical procedures were used as follows:

##### 14.4.1 Soil and Rock Analyses

The procedure described briefly below is known as the Catalytic Method. For complete details of this technique refer to reference 10.

A 100 milligram sample of the soil or pulverized rock sample was digested in 2ml of chloric acid until the volume was less than one ml. The volume was adjusted to 10 ml with arsenite solution and warmed in a water bath at 70°F. After about 15 minutes 1 ml of cerate solution was added. After another 8 minutes the reaction was "frozen" by adding the solution to a flask containing a few drops of mercury solution and then titrating with a ferrous solution. The accuracy of the method is  $\pm 5\%$  on pure solutions and the precision on natural samples is of the same order but the method suffers from interference by Hg and Ag resulting in negative readings. These elements were analyzed for independently and the results applied as correction factors to the iodine value to arrive at the final iodine determination.

In some instances the initial iodine value before Hg and Ag corrections was distinctly negative and after applying the appropriate corrections remained negative. This is probably due to interferences other than Ag and Hg which has not been previously reported. To avoid negative  $I_2$  values the most negative result was set to zero and all other values normalized to it. This in effect shifted the zero reference without disturbing the relative nature of the data or the shape of the anomaly. The individual iodine values however have no significance in the absolute sense. The threshold sensitivity of the method is  $0.1 \text{ ppm} \pm 0.05$ .

##### 14.4.2 Air Analyses - Catalytic Method

The above method for soils was attempted for measurement of atmospheric  $I_2$  by substituting for the 100 mgm soil sample, a 1.0 ml sample of a 25 ml solution from an air sampling apparatus. This was unsuccessful however because of limitations of

detection limit of the method and the air sampling apparatus. The amount of air required to reach the sensitivity required was far in excess of the air flow and collection capacity of the equipment.

Specific Ion Electrode Method - See reference 11 for a comprehensive treatment of the method. Briefly it involved pumping an air sample through 40 ml of deionized water in four high-speed glass bubblers.  $\text{SO}_2$  was introduced into the system every 20 minutes to counter  $\text{H}_2\text{S}$  interference. At the end of the sampling period the volume of water was adjusted to 25 ml and tested on a potentiometer using specific ion electrodes.

The method was unsuccessful because of the limitations of the air flow apparatus as previously discussed and possibly  $\text{H}_2\text{S}$  interference. The wet chemical results reported herein therefore do not include atmospheric iodine but are restricted to representative suites of samples from the very large numbers of rock and soil samples collected.

#### 14.4.3 Porphyry Copper (Sierrita Pit)

Figure 30 shows the soil sample results from a traverse extending some 7-8 miles north of the Sierrita pit and Figure 33 shows some of the results obtained inside the pit. The  $\text{I}_2$  value for each sample shown is given in normalized units of ppm by weight and appears immediately following the sample identification number and oblique stroke.

It is immediately evident from Figure 30 and 33 that values inside the open pit area tend to be, on the average, lower than values obtained in the soils or rocks at the north end of the traverse. This is of course exactly opposite to the geo-chemical anomaly that might be expected over a porphyry copper ore body. The full significance of this apparent inverted anomaly is not known and a fuller study of the geo-chemical character of the region is necessary. The magnitude of the effort required to perform this study adequately is considered outside the scope of this program, however, since the existence of an inverted anomaly (or lack of a positive one) is very pertinent to the results obtained with the spectrometer

it is perhaps worthwhile to speculate on what an extended study might reveal. Firstly, as touched on previously, the liberation of volatile materials from mineralized formations is considered by some authorities to be associated primarily with the near-surface zones of ore bodies and to be intimately related to bacterial action in the presence of near-surface organic materials. The stripping of the overburden and removal of the top layers of the ore body moreover effectively destroys the biogeochemical mechanism of volatile emissions and the anomaly is rapidly dissipated. This would account for the absence of anomalous  $I_2$  levels inside the pit but would not explain the low values within a few miles to the north of the pit.

A second explanation may be that the Sierrita deposit forms only one zone of a much larger mineral formation within perhaps the same underlying batholith and the volatile anomaly is associated not with the central zone of the deposit but with an encircling outer zone which became enriched with the volatile components of the ore-forming fluids when the ore body was originally formed. The existence of a doughnut-shaped mercury-enriched zones around a similar porphyry copper deposit (near Ely, Nevada) has been reported previously (reference 12). Additional analyses of rock and soil samples including some collected well to the north of the area covered in Figure 30, will hopefully help to resolve these questions. These results will be reported elsewhere.

#### 14.4.4 Oil Field - (Midway Sunset)

Figures 41 and 43 shows the locations of all the soil samples obtained in the Midway-Sunset oil field, with final  $I_2$  values shown for a representative suite covering the Globe Anticline area and centered roughly on the spectrometer long-path sites. Referring first to Figure 41 the presence of a very strong  $I_2$  anomaly is evident at the Tar Pit near McKittrick. This is a massive oil seep associated with outcropping of the Belgian Anticline oil field. A secondary anomaly is evident at P6 with a steady fall off to a minimum value at P25. Reference to a well-location map of Midway Sunset shows a majority of wells are located in the north and south ends of

of the field while the central region has a relatively low well density indicating that the strong soil anomalies are associated with areas of concentrated oil production. The zero ppm value shown at P25 is not zero of course but simply the lowest value of  $I_2$  measured as previously explained.

Figure 43 shows interesting results from a traverse which began to the west of the field at R1 and ran across the oil bearing sand out-crop into the oil field, followed the approximate boundary of the field to R27, back into the center of the field at R28 and proceeded eastward beyond the field to R41. The highest value of 5.6 ppm obtained at R9 is believed to be associated with the oil sand outcrop which runs lengthwise from NW to SE along the foothills of the Temblor Range which bound the field on the west side. The outcrop is visible to eye but unfortunately its position was not marked on the map. The high values of 4.9 and 4.5 ppm at R17 and R19 are probably associated with the high well density in this part of the field.

#### 14.4.5 Geothermal Sources (Geyserville)

Figure 46 shows the soil samples locations and some results. The very high  $I_2$  levels obtained are closely associated with very strong Hg anomalies in the immediate vicinity of the natural steam emissions. The reason for the relatively high value of 4.1 ppm at site 18 is not known.

Section 15

DISCUSSION OF RESULTS

The following relationship of units is useful in discussing iodine concentrations in the atmosphere and in soils or rocks.

- 1 ppb vol/vol. of I<sub>2</sub> vapour in air @ STP = 11.3 µgms/m<sup>3</sup>
- 1 ppb vol/vol. of I<sub>2</sub> vapour in air @ STP = 8.75 ppb wt/wt.
- 1 ppb wt/wt of I<sub>2</sub> in vapour in air @ STP = 1.29 µgms/m<sup>3</sup>.

The existing literature contains numerous references to previous investigations of airborne I<sub>2</sub>. Godschmidt (reference 13) quotes Fallenburg as stating that background I<sub>2</sub> varies from 0.1 to 1.5 ppb (by wt.) with an average of 0.5 ppb (wt) which is 0.128 to 1.92 µgms/m<sup>3</sup> with an average of 0.64 µgms/m<sup>3</sup>. Along the New England coast it reaches 12 ppb (wt) or 1.53 µgms/m<sup>3</sup>. Rankama and Sahama (reference 14) quote 0.1 to 1.0 µgms/m<sup>3</sup> for atmospheric background I<sub>2</sub>.

In terms of the correlation spectrometer output the conversion from ppb to µgms/m<sup>3</sup> requires a temperature correction factor since the sensor's internal reference cell was calibrated using a one meter laboratory standard at 21°C. Therefore to convert the remote sensor readings; for long path (remote lamp) readings;

$$\text{sensor reading (in ppb's)} \times 11.3 \times \frac{273}{294} = \text{sensor result in } \mu\text{gms/m}^3$$

or 1 ppb (by sensor) = 10.5 µgms/m<sup>3</sup>, similarly for passive mode operation;

1 ppb-meter (by sensor) = 10.5 µgms/m<sup>3</sup> over a path length of one meter.

Over the Sierrita pit a maximum value of 2.6 ppb was recorded over 1142 meters (Figure 34). This is equivalent to 27.3 µgms/m<sup>3</sup>. This was observed only for 4-5 minutes, with considerably lower values being recorded the rest of the time.

It is readily apparent from Figure 34 that a significant noise component occurs in the long path measurement of atmospheric gases. This noise component is due to a number of factors, some of which are not yet fully understood. The most significant of the noise generating mechanisms in the long path method of measurements is probably the random movement of air and airborne particulate matter in the optical path. Turbulent air alone will cause fluctuations in angle of arrival of the wave front which in turn cause the image of the light source to oscillate about a mean position (image dancing). Turbulence also causes apparent fluctuations in the light source intensity, i.e. amplitude scintillation. Both of these effects can be minimized by appropriate instrument design. A more serious source of error however is that due to non-uniform scattering of light into and out of the beam by airborne aerosol. Since the principle of the spectrometer measurement relies on changes in the spectral distribution of energy in its bandwidth, the tendency of cloud of airborne particles to selectively scatter light in the beam represents a fundamental source of noise and which may ultimately limit the sensitivity and accuracy of the remote lamp method of measurement.

At the time of recording Figure 34 (1) the wind was observed, to be quite variable. The rotating cup anemometer measured a wind speed of 5 mph gusting to 20 mph. Under these conditions the long path method of measurement was unable to detect  $I_2$  concentrations below about 1 ppb. In general, throughout the field program the threshold sensitivity of the long path system using a remote lamp was best at times of low winds and relative calm.

The occasional occurrence of negative  $I_2$  signals as shown in Figure 34 (2) was thought possibly due to another halogen characteristic of oxidizing ore bodies such as bromine. Bromine has absorption spectra which corresponds closely with portions of the  $I_2$  spectra but its absorption coefficient is very much less. The atmospheric bromine concentrations necessary to produce such interference would have to be of the order of 1000 ppb (by vol) which seems highly unlikely. The remaining halogens which are also considered to be associated with copper porphyrys, flourine and chlorine do not have significant spectral structure in the 5000 -

6000 Å region. Although the vibration rotational bands of chlorine according to the available literature show an almost featureless continuum over this range, a single-slit scan of a 220 ppm-meter (vol) cell of  $\text{Cl}_2$  indicated the presence of a continuous series of closely spaced band heads but much too weak to account for the effects observed over the pit.

The relatively intense Xe emission spikes evident in the upper trace of Figure 33 occur unfortunately, in the region of most intense  $\text{I}_2$  absorption. The correlation mask was designed to operate over a 230 Å range (Figure 37) with four slits of the total of 12 removed to avoid correlation with the 4 Xe lines evident in the Figure 38 (1). Whatever residual Xe line correlation signal remains is greatly reduced when the normal multi-slit mask is used.

In the case of the oil field, the background-only single slit scans at the Twistleman ranch was very similar to the Midway-Sunset scan No. 1 of Figure 42 (3) although the noise level was somewhat higher.

The presence of  $\text{I}_2$  in the single slit scan traces was detected by visual cross correlation of one trace against another. This is not an efficient or effective way of detecting signals buried in noise. It might be worthwhile in future work where trace gases are to be measured using this method on a large scale, to digitize the data and perform sliding correlation analysis with a computer.

The passive mode operation of the correlation spectrometer over the oil field produced the most encouraging results of the entire field trip. The polar plots of Figure 45 were done in clockwise fashion beginning at  $0^\circ$  and progressing clockwise through  $360^\circ$ . The time required to complete the full circle was 60 minutes and during this time interval the wind shifted direction from S.E. at the start to due East and occasionally northerly at the finish and increased in speed from 15 mph to 25 mph in the same period. This may account for the much smaller burden recorded at  $350^\circ$  than at  $10^\circ$ .

The much greater responses from the SE direction is considered to be due to the fact that wind-born  $\text{I}_2$  emissions from the region of Midway-Sunset south of Miwday peak would be substantially greater than regions of the field

north of the peak. The Elk Hill oil field is a Naval reserve and is non-productive. Little is known about the Buena Vista area but its production rate and hence its likely  $I_2$  emission is certainly substantially less than Midway Sunset. The signal-to-noise measurement is impressive. For the maximum value of 4,900 ppb-meters the S/N ratio was approximately 16. In terms of  $\mu\text{gms}/\text{m}^3$  the equivalent peak value of the anomaly was  $5.1 \times 10^4 \mu\text{gms}/\text{m}^3$  referred to a one meter pathlength. The equivalent noise level was  $3.15 \times 10^3 \mu\text{gms}/\text{m}^3$  referred to one meter.

## Section 16

### AIRCRAFT & SPACECRAFT APPLICATIONS OF THE I<sub>2</sub> CORRELATION SPECTROMETER

#### 16.1 INTRODUCTION

As is indicated in Section 13 of this report, the spectrometer configuration used on the I<sub>2</sub> field program utilized quartz refractor plates mounted on a tuning fork to produce the high speed oscillation of the spectrum relative to the mask. In this Section the feasibility of detecting atmospheric iodine using this same instrument technique is discussed as it relates to airborne and spaceborne sensors. Performance of a ground based sensor is included for comparison purposes. Specifically, the following theoretical development of sensor signal-to-noise ratios is calculated on the basis of photon noise limitation and does not include contributions from either electronic noise sources or dark current noise from the photodetector. The latter two sources are considered to be small in comparison to the photon noise contribution. Moreover the calculation is based on normal natural light conditions free of noise contributions from atmospheric fluctuations or variations in ground reflectivity. These noise sources can be largely taken care of by appropriate sensor design.

On the basis then of the expected photon noise level the work in this Section determines the minimum detectable amounts of molecular iodine with the present refractor plate instrument.

The expected improvement in the detectable threshold levels that could be obtained with a more advanced version of the correlation spectrometer is also indicated.

## 16.2 Signal-to-Noise Ratio

The response of the photodetector in amperes per watt of incident radiation is given by:

$$I_1 = \frac{P_1}{\mu/\lambda} G \eta e \quad \text{when the spectrum is in position (1) with respect to the mask. (Amp)}$$

$$I_2 = \frac{P_2}{\mu/\lambda} G \eta e \quad \text{when in position (2)}$$

where

$P_1, P_2$  are the Radiant powers incident on the photodetector when the spectrum is in position (1), (2) with respect to the mask (w)

G photodetector gain

$\eta$  quantum efficiency of the photodetector

$\mu/\lambda$  energy equivalent associated with wavelength  $\lambda$  at the nominal center of the waveband used (W sec)

e electronic charge (Coulombs)

The noise current at the photocathode is

$$I_{\text{noise}} = G e \frac{P \eta}{\mu/\lambda} \cdot \frac{1}{4\tau}$$

where P, is the power incident on the photodetector.

$\tau$ , is the integration time of the electronics.

Position(1) is used to control the AGC; thus, in this position  $I_1$  is fixed by electronic design, and the gain of the photodetector becomes:

$$G = \frac{h}{\lambda} \frac{I_1}{P_1 \eta e}$$

The physical observable chosen for the measurement is the difference of photo-detector currents; therefore,

I signal  $I_1 - I_2$ , that is

$$I_S = \frac{P_1}{h/\lambda} G \eta e - \frac{P_2}{h/\lambda} G \eta e$$

and substituting the value of G, from equation - 1 - we obtain

$$I_2 = I_1 \left\{ 1 - \frac{P_2}{P_1} \right\} = I_1 \left\{ \frac{P_1 - P_2}{P_1} \right\}$$

The expression for the signal to noise ratio becomes

$$\frac{S}{N} = \frac{I_S}{I_n} = \frac{I_1 \frac{P_1 - P_2}{P_1}}{G e \sqrt{\frac{P \eta}{h/\lambda} 4\tau}}$$

and substituting again the value of G from equation 1, we finally obtain

$$\frac{S}{N} = \frac{P_1 - P_2}{\max(P_1, P_2)} \sqrt{\frac{4\tau \eta}{h/\lambda}} \quad (2)$$

$\max(P_1, P_2)$  is the value of whichever happens to be the maximum of  $P_1$  or  $P_2$ , since its contributions to the photon noise will be the largest.

We recall from reference 15 that

$$P_1 = A \Omega R_1 = A \Omega \int_{\lambda 1i}^{\lambda 1i} [N_\lambda e^{-a(\lambda) cL} + N_\lambda'] \beta(\lambda) d\lambda \quad (w) \quad (3)$$

$$P_2 = A \Omega R_2 = A \Omega \int_{\lambda 2i}^{\lambda 2i} [N_\lambda e^{-a(\lambda) cL} + N_\lambda'] \beta(\lambda) d\lambda \quad (w) \quad (4)$$

where

- $A \Omega$  is the "étendue" or throughput of the instrument ( $\text{cm}^2 \text{sr}$ )  
 $N_{\lambda}$  spectral radiance irradiating the gas to be detected ( $\text{Wcm}^{-2} \text{nm}^{-1} \text{sr}^{-1}$ )  
 $N_{\lambda}$  spectral radiance with no gas absorption in it ( $\text{Wcm}^{-2} \text{nm}^{-1} \text{sr}^{-1}$ )  
 $a(\lambda)$  absorption crosssection per molecule of the gas at a fixed temperature and pressure ( $\text{cm}^2$ )  
 $cL$  concentration times pathlength in ( $\text{cm}^{-2}$ )  
 $\beta(\lambda)$  filter-optics transmission function  
 $\lambda_{1i}'$   $\lambda_{2i}'$  beginning and end wavelength of slit -i- in positions (1) and (2)

The product concentration times pathlength ( $\text{molecules/cm}^2$ ) can be expressed in parts per million by volume along a meter path length (ppm-m), or in micrograms per cubic meter of the chosen gas along a meter pathlength, by multiplying by the appropriate factors.

The dimension of the integrals are those of radiance ( $\text{W cm}^{-2} \text{sr}^{-1}$ ). Substituting (3) and (4) into (2), we obtain for the S/N:

$$\frac{S}{N} = \frac{|R_1 - R_2|}{\max(R_1, R_2)} \cdot \sqrt{\frac{4\eta\beta(\lambda)A\Omega}{h/\lambda}} \cdot \sqrt{\tau} \quad (5)$$

The values of  $R_1$  and  $R_2$  for each mask, jump, slits widths, etc. are obtained with the theoretical computer model of the instrument, as indicated in reference (15).

Existing instrument parameters

$$\begin{aligned} A \Omega &= \frac{\text{area of grating} * \text{area entrance slit}}{(\text{focal length dispersive element})^2} \\ &= \frac{(6.7)^2 \text{ cm}^2 \cdot 1 \text{ cm} \cdot 0.018 \text{ cm}}{625 \text{ cm}^2} = 1.3 \times 10^{-3} \text{ (cm}^2 \text{ sr)} \end{aligned}$$

$$\eta = 20\%$$

$$h/\lambda \text{ centered @ } 5370 \text{ \AA} \text{ is } 3.7 * 10^{-19} \text{ (W)}$$

Substituting in equation 5, we obtain

$$\frac{S}{N} = \frac{|R_1 - R_2|}{\max(R_1, R_2)} \cdot (2.24 * 10^7) \sqrt{T} \quad (6)$$

### 16.3 SPECTRAL RADIANCES AVAILABLE AT THE INSTRUMENT

We assume in the following calculations that the values of the spectral radiances obtained hold for the total of the instrument waveband.

The instrument's waveband is from 5250  $\text{\AA}$  to 5490  $\text{\AA}$ , and we will take 5370  $\text{\AA}$  as the nominal center of the waveband.

We will accept 5350  $\text{\AA}$  as representative, with respect to the atmospheric back-scattered radiation necessary for the ground band and satellite band instrument calculations. The following calculations will be performed for two sun zenith angles  $\theta_o$ , of 30 and 60 degrees.

#### 16.3.1 Sky Spectral Radiance, Ground Based Instrument

In reference (1) pages 256 to 270, we find the appropriate factors by which we should multiply the solar irradiance outside the atmosphere to obtain the radiance of the appropriate section of the sky.

We consider the anti-solar looking mode at sea level and find  $I_m$ , intensity of the radiation due to all orders of scattering in the direction of observation  $\theta_o$ .

The values are:

Zenith observation angle $\theta$	Sun Zenith Angle $\theta_o$	
	$\theta_o = 30^\circ$ $I_m$	$\theta_o = 60^\circ$ $I_m$
0	$3.624 \times 10^{-2}$	$2.453 \times 10^{-2}$
15	3.221	2.179
30	2.995	2.287
40	3.019	2.656
50	3.294	3.396
60	4.029	4.766
70	5.776	7.467
80	10.59	14.13

To obtain the spectral radiance at any observation angle, we must multiply  $I_m$  by  $H_o \lambda / \pi$ .

$H_o \lambda$  being the solar spectral irradiance outside the atmosphere at  $5370 \text{ \AA}$ ,  
 $H_o = 1.98 \times 10^{-4} \text{ (W cm}^{-2} \text{ nm}^{-1}\text{)}$   
 calculated at the mean sun-to-earth distance, reference (7) page (16-5).

We shall consider the most unfavourable cases for observation namely when

$$\theta = 30^\circ \text{ and the sun zenith angle } \theta_o = 30^\circ$$

$$\theta = 15^\circ \text{ and the sun zenith angle } \theta_o = 60^\circ$$

The two corresponding spectral radiances are:

$$\text{for } \theta = 30^\circ, \theta_o = 30^\circ, N_\lambda = 1.89 \times 10^{-6} \text{ (W cm}^{-2} \text{ nm}^{-1} \text{ sr}^{-1}\text{)}$$

$$\theta = 15^\circ, \theta_o = 60^\circ, N_\lambda = 1.49 \times 10^{-6} \text{ (W cm}^{-2} \text{ nm}^{-1} \text{ sr}^{-1}\text{)}$$

### 16.3.2 Solar Reflected Spectral Radiance, Airborne Instrument

From reference (7) pages 16-8 and 16-9, we obtain for the spectral irradiance incident on the ground:

SunZenith Angle $\theta_o$	Spectral Irradiance $H_\lambda$ (W cm <sup>-2</sup> nm <sup>-1</sup> )
30°	1.22 * 10 <sup>-4</sup>
60°	0.595 * 10 <sup>-4</sup>

We consider now an observer looking vertically down to a Lambertian reflecting ground. The reflectivity of the ground at 5370 Å varies widely from about 5% for wintertime coniferous forest to 60% for clay and limestone to as high as 80% for fresh snow; we will take 10% as representative. In this situation the spectral radiances of the ground for the observer are:

Sun Zenith Angle $\theta_o$	Spectral radiance $N_\lambda$ (W cm <sup>-2</sup> nm <sup>-1</sup> sr <sup>-1</sup> )	( $N_\lambda = \frac{H_\lambda}{\pi}$ )
30°	3.9 * 10 <sup>-6</sup>	
60°	1.9 * 10 <sup>-6</sup>	

This spectral radiance is attenuated on its way from the ground to the observer due to a combined (Rayleigh scattering-natural aerosol scattering effect). The attenuation coefficient  $\tau$  are obtained from reference 16, interpolating between the values at 5000 Å and 5500 Å.

The total attenuation is  $\exp[-\tau]$  and the apparent spectral radiance at the observer are:

Altitude of Observer (Km)	Attenuation coeff. $\tau$	Attenuation	Apparent Spectral Radiances	
			Sun $\theta_o=30^\circ$	Sun $\theta_o=60^\circ$
1	0.131	0.875	3.42*10 <sup>-6</sup>	1.65*10 <sup>-6</sup>
2	0.825	0.825	3.22*10 <sup>-6</sup>	1.57*10 <sup>-6</sup>
50	0.41	0.664	2.59*10 <sup>-6</sup>	1.26*10 <sup>-6</sup>

The last figure, that of 50 Km altitude, will be used for the satellite-based instrument calculations.

### 16.3.3 Atmospheric Scattered Spectral Radiance, Satellite Platform

The value of the intensity of radiation due to all orders of scattering are again obtained from reference (1), for the upward radiation emerging at the altitude of 0.18 mb, equivalent to approximately 60 Km.

The process to calculate the spectral radiance of the atmosphere for an observer looking vertically down is similar to that followed for an observer looking at the sky. The values are:

Sun Zenith Angle $\theta_o$	$I_m$	Backscattered Spectral Radiance $N'_\lambda$ ( $W\ cm^{-2}\ nm^{-1}\ sr^{-1}$ )	$(N'_\lambda = \frac{I_m}{\pi} H_o \lambda)$	Ratio Scattered direct reflected
30°	$3.6 \cdot 10^{-2}$	$2.27 \cdot 10^{-6}$		0.88
60°	$2.413 \cdot 10^{-2}$	$1.52 \cdot 10^{-6}$		1.2

### 16.4 SIGNAL-TO-NOISE RATIO CALCULATIONS

On the values obtained for the signal carrying spectral radiance  $N$  and for the backscattered spectral radiance  $N'_\lambda$ , we superimpose the equivalent width of the Fraunhofer lines of the solar spectrum in the waveband of interest.

The equivalent width are added for each  $2 \text{ \AA}$  intervals centered on each even wavelength. When the sum of the equivalent widths in one interval equals  $2 \text{ \AA}$ , we assume that there is no light available at that waveband.

In the other wavebands the corresponding fraction of energy is subtracted according to the equation

$$\text{effective spectral radiance} = N_\lambda \left\{ 1 - \frac{0.2nm}{TEW} \right\}$$

TEW is the total Equivalent Width of the Fraunhofer lines in the 0.2nm intervals. The line equivalent width are obtained from reference 17.

Following the mask optimization process outlined in References (4) and (5) we obtain  $R_1$  and  $R_2$ .

We assume that the double-sided response is used.

In general, the radiances  $R_1$ ,  $R_2$  are composed of two additive terms, as can be seen in equations -3 and 4, one with information about the gas chosen, and the other with no information.

The double-sided response consists in simple terms of the obtaining of two pairs of values of  $R_1$ 's and  $R_2$ 's, namely  $R_1, R_2, R_1', R_2'$ . For the pairs  $(R_1, R_2)$   $(R_1', R_2')$  the gas contributions are different (and if possible of different sign) and the no gas contributions equal. The difference of the response for the two pairs of values adds the gas contributions and cancels the spurious contributions due to interference and/or backscattered radiation. In the case of the double-sided response,  $|R_1 - R_2|$  is substituted by  $|R_1 - R_2| + |R_1' - R_2'| = \Delta R$ ,

and  $\sqrt{\max(R_1, R_2)}$  by  $\sqrt{\max(R_1, R_2, R_1', R_2')}$ , since we assume that the largest value of the radiant power incident onto the phototube is the one which determines the photon noise.

A 12 slit mask, optimized for the NASA  $I_2$  field program, has the following parameters:

1/2/9/10/18/19/27/28/36/46/47/56/57/68/69/78/79/89/90/101/102/113/114

Initial wavelength in position (1) is at 5256 Å

Initial wavelength in position (1') is at 5262 Å

Amplitude of jump  $\delta = 6$  Å, [position (2), coincides with (1')].

(Width of the slits, the same for all of them and equal to 4Å).

Figure 47 represents the theoretical response of the mask to the absorption bands of  $I_2$  when irradiated with a spectrally flat light source.

Figure 48 represents the theoretical response of the mask to the Fraunhofer lines of the solar spectrum in the same spectral region.

Figure 49 is an overlap of Figures 1 and 2 showing points A and A' where the response to the gas is at a maximum while the response to the Fraunhofer lines is the same (the difference therefore is zero).

Figure 50 is the actual laboratory scan of  $I_2$  gas corresponding to mask obtained with the theoretical model of Figure 1.

Figure 51 is the actual field scan of the solar spectrum using the mask, and corresponds to the theoretical Figure 2.

Figure 52 is an overlap showing the actual situation of the points AA' used for the measurement.

The theoretical computer-modelled response yields  $|R_1 - R_2| + |R_1 - R'_2| = 0.026 N_\lambda$  for 1 ppm-m of  $I_2$  at STP.

The maximum value of the set  $(R_1, R_2, R'_1, R'_2)$  is for  $R'_1 = 3.229 * N_\lambda$ , in the case of no backscattered radiation, and  $R'_1 = 3.229 [N_\lambda + N'_\lambda]$  for the situation with backscattered spectral radiance (satellite platform).

Thus,

$$\sqrt{\max(R_1, R_2, R'_1, R'_2)} = \begin{matrix} 1.815 \sqrt{N_\lambda} & \text{with no backscatter} \\ 1.815 \sqrt{N_\lambda (1+R)} & \text{with backscatter} \end{matrix}$$

R is the ratio between backscattered and direct ground-reflected spectral radiances.

The relationship between ppm (by volume) and  $\frac{\mu\text{gm}}{\text{m}^3}$  for  $I_2$ , at STP 20°C is

$$\frac{\mu\text{gm}}{\text{m}^3} = \text{ppm} \times 1.13 \times 10^4$$

thus, 1 part per million by volume =  $1.13 \times 10^4 \frac{\mu\text{gm}}{\text{m}^3}$

The Noise Equivalent Amount, NEA, or concentration pathlength product, for which the signal-to-noise ratio is one, is given by:

$$\text{NEA} = (S/N)^{-1} = \frac{\sqrt{\max(R_1, R_2, R_1', R_2')}}{\Delta R} * \frac{4.45 \times 10^{-8}}{\sqrt{\tau}} \text{ in ppm-m} \quad (7)$$

and it becomes

$$\frac{1.815 * 4.45 \times 10^{-8}}{0.026 \sqrt{N_\lambda} \sqrt{\tau}} \cdot 1.13 \times 10^4 = \frac{3.1 * 10^{-2}}{\sqrt{N_\lambda} \sqrt{\tau}} \left( \frac{\mu\text{gm}}{\text{m}^2} \right) \text{ for no backscatter}$$

and

$$= 3.1 \times 10^{-2} \sqrt{\frac{1+R}{N_\lambda}} \frac{1}{\sqrt{\tau}} \left( \frac{\mu\text{gm}}{\text{m}^2} \right) \text{ with backscatter}$$

In Tables I, II, and III the threshold concentration pathlength products for the different conditions, obtained by substituting the appropriate values of the  $N_\lambda$  and R in the previous equations, are presented for  $\tau = 1$  sec. integration time.

TABLE I

## GROUND-BASED INSTRUMENT LOOKING TO THE ANTISOLAR SIDE

Look Angle	NEA for $\theta_0 = 30^\circ$	NEA for $\theta_0 = 60^\circ$
	in $\frac{\mu\text{gm}}{3} \cdot \text{meter}$ m	in $\frac{\mu\text{gm}}{3} \cdot \text{meter}$ m
0	20.05	25
15	22	25.4
30	22.3	25.8
40	22.5	24
50	21.5	21.1
60	19.5	18
70	16.3	14.6
80	12	10.4

TABLE II

## AIRCRAFT-BASED INSTRUMENT LOOKING VERTICALLY DOWN

Altitude Km	NEA for $\theta = 30^\circ$	NEA for $\theta = 60^\circ$
	$(\frac{\mu\text{gm}}{3} \cdot \text{m})$ m	$(\frac{\mu\text{gm}}{3} \cdot \text{m})$ m
1	16.7	24.1
2	17.3	25.7

TABLE III

## SATELLITE-BASED INSTRUMENT LOOKING VERTICALLY DOWN

Sun Zenith Angle $\theta_0$	NEA $(\frac{\mu\text{gm}}{3} \cdot \text{m})$ m
$30^\circ$	26.4
$60^\circ$	41

## 16.5 CONCLUDING OBSERVATIONS

From the foregoing it is apparent that the most sensitive way of using the remote sensing correlation spectrometer to detect free molecular iodine in the atmosphere is to use it as a ground based instrument and observe the sky at high zenith look angles much the same way it was used for the field measurement program.

In this mode of operation, the advantages are two-fold, (1) long path lengths are obtainable and (2) plenty of energy from the backscattered solar radiation is available. The next most sensitive method of usage is as an aircraft-based instrument looking vertically down, with a combination of high sun zenith angles.

In the case of extended gas layers the airborne observation mode may be even more advantageous than the ground-based mode for the following reasons:

- (1) Longer path lengths through the gas cloud are realized because of the solar radiation passing at least twice through the layer.
- (2) Optimum sensor performance is obtained with low sun zenith angles (high solar altitude) which corresponds to maximum solar heating of the ground surface and hence maximum  $I_2$  emissions.

In the satellite application the instrument response also benefits from high solar altitude and long path lengths.

We will now consider the contribution of sky radiation incident on the ground carrying varying degrees of gas information. This light would in general increase the signal-to-noise ratios at least for the aircraft and satellite based instrument.

If we assume as a workable S/N ratio of 5 in the satellite observation mode with the sun at  $60^\circ$  from the zenith, we need  $205 \frac{\mu\text{gm}}{\text{m}^3}$  along a meter path length, or  $0.205 \frac{\mu\text{gm}}{\text{m}^3}$  along a 1 Km path length.

Considering that the scale height for the diffusion of  $I_2$  in the atmosphere is of the order of 1 Km, and that the estimated background levels of  $I_2$  are of the order of 0.1 to 1  $\frac{\mu\text{gm}}{\text{m}^3}$ , the detection of normal background  $I_2$  in the atmosphere seems possible although marginal.

We will now consider what further improvement is possible in an instrument where the constraints imposed by the refractor plate are eliminated, namely:

- (a) width of slit -i- in position (1) and (2) are the same.
- (b) Amplitude of jump equal for all slits.

At Barringer Research a second generation correlation spectrometer has been developed which utilizes a rotating disc-shaped correlation mask which accomplishes both the refractor plate and oscillating grating function. In this type of instrument an improvement in  $\Delta R$  of at least 30% is possible. Additional improvements are readily available some of which result from the rotating disc approach, namely

- (a) Multiple entrance slits for greater energy throughput.
- (b) More freedom in mask calculation and optimization.
- (c) Improved transmission efficiency by grating custom blazing, high quality optical materials, and reflective coatings.

Considering now a four entrance slit system, the improvements due to a more sophisticated (rotating disc) mask design (30%), and improved blaze angle efficiency (the efficiency assumed in the calculation has been 40% and this figure can be brought up to 60%). The minimum detectable or threshold levels can be lowered by a factor of 0.36 i.e. 131  $\mu\text{gms}/\text{m}^3$  relative to a one meter path length. This performance would appear to represent the theoretical limits of detectability for this type of correlation technique.

Section 17

ACKNOWLEDGEMENTS

The two projects reported on herein were both field evaluation programs which relied heavily on the voluntary cooperation and assistance of many individuals and organizations. Barringer Research gratefully acknowledges the support of the following:

University of Saskatchewan, Dr. E. J. Lewellyn

City of Chicago, Department of Environmental Control

Environmental Measurements Inc. of San Francisco

Department of Transport, Satellite, Data Laboratory, Toronto International Airport

Kennecott Copper Corporation

Phelps Dodge Corporation, Robert N. Schnepfe - Geophysicist

Duval Sierrita Corporation, Robert A. Metz, Chief Mine Geologist

U.S. Geological Survey, Mr. K. Heath, District Engineer, Bakersfield

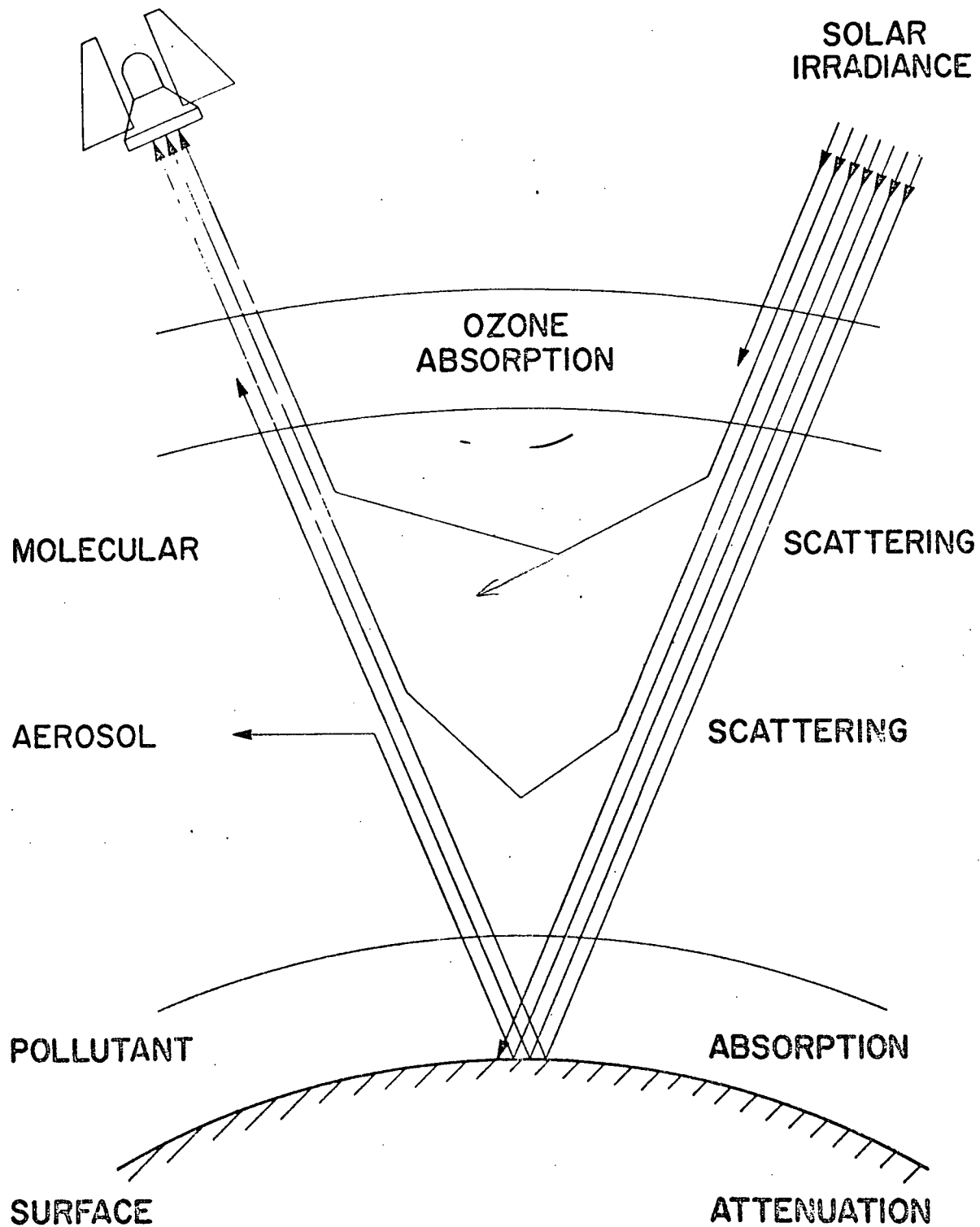
Standard Oil Company of California, Mr. E. Gialdini, District Superintendent,  
Taft, California.

## REFERENCES

1. Dave, J. V., Furukawa, P. M. - Scattered Radiation in the Ozone Absorption Bands at Selected Levels of a Terrestrial Releigh Atmosphere. The American Meteorological Society, Meteorological Monograph Volume 7, January 1966, No. 29.
2. Final Report - Absorption Spectrometer Modifications and Flight Testing. Contract No. NAS9-7958. Barringer Research TR69-79, January, 1969.
3. Results of Airborne Survey of NO<sub>2</sub> and SO<sub>2</sub> over Los Angeles Basin. Barringer Research Limited Report TR68-68, September 1968.
4. Feasibility of Air Pollutants Detection From a Balloon Platform Using the Barringer Correlation Spectrometer, BRL Report No. TR69-109, UTIAS Report No. 156.
5. Report on Barringer Research Flight - Winzen Research Incorp., Report No. 1297R, October 1969.
6. Skylook Flight 1237 for University of Saskatchewan, July 18, 1968. Raven Industries Report R-0169001.
7. Air Force Cambridge Research Laboratories - Handbook of Geo-physics and Space Environments, McGraw-Hill, 1965.
8. Recent Progress in the Remote Detection of Vapours and Gaseous Pollutants. A. J. Moffat, A. R. Barringer, Proceedings of the Sixth International Remote Sensing Symposium, Ann Arbor, Michigan, October 13-16, 1969.
9. The Problems and Potential in Monitoring Pollution from Satellites. A. R. Barringer, J. H. Davies, A. J. Moffat. Presented at the AIAA Earth Resource Observations and Inforamtion Systems, March 2-4, 1970, Annapolis, Maryland.

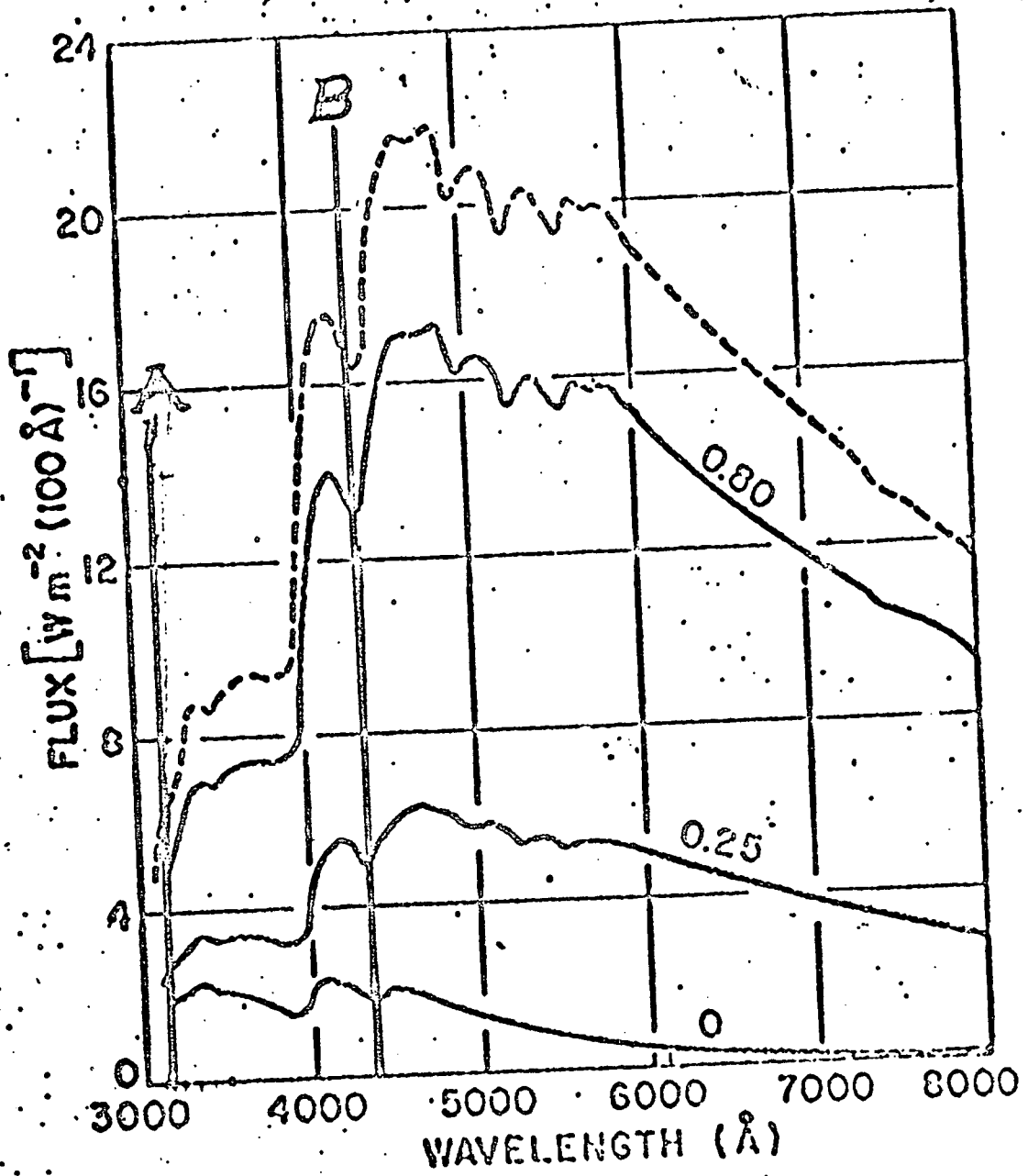
10. Analytical Chemistry - Vol. 29, No. 12 1957, P1870.
11. Ion-Selective Electrodes - United States Department of Commerce, National Bureau of Standards, Special Publications 314, Washington, D.C. 20234.
12. Gatt, G. and McCarthy, H. USGS, Cir. 535, 1966.
13. Goldschmidt, V. M. Geochemistry Clarendon Press, 1962.
14. Rankama, K. and Sahama Tk. G., Geochemistry, University of Chicago Press, 1950.
15. Millan, M., Townsend, S., and Davies J. Study of the Barringer Refractor Plate Correlation Spectrometer as a Remote Sensing Instrument. University of Toronto Institute for Aerospace Studies, Report No. 146 (1970).
16. U.V., Visible and IR Attenuation for Altitudes to 50 Km 1968, L. Elterman. Air Force Cambridge Research Laboratories, 1968.
17. The Solar Spectrum 2935 Å to 8770 Å, Monograph 61 United States Department of Commerce National Bureau of Standards, 1966.

OUTGOING FLUX = GAS SIGNAL + DILUTION



## ATTENUATION & DILUTION

FIGURE 1



Spectral distribution of flux emerging from top of a model atmosphere for different values of surface reflectance ( $r = 0, 0.25, \text{ and } 0.80$ ) and the sun at the zenith; dashed curve is the incident extraterrestrial flux. (After Coulson [1959].)

FIGURE 2

### EMERGING FLUX DISTRIBUTION



# AIR MONITORING PROGRAM

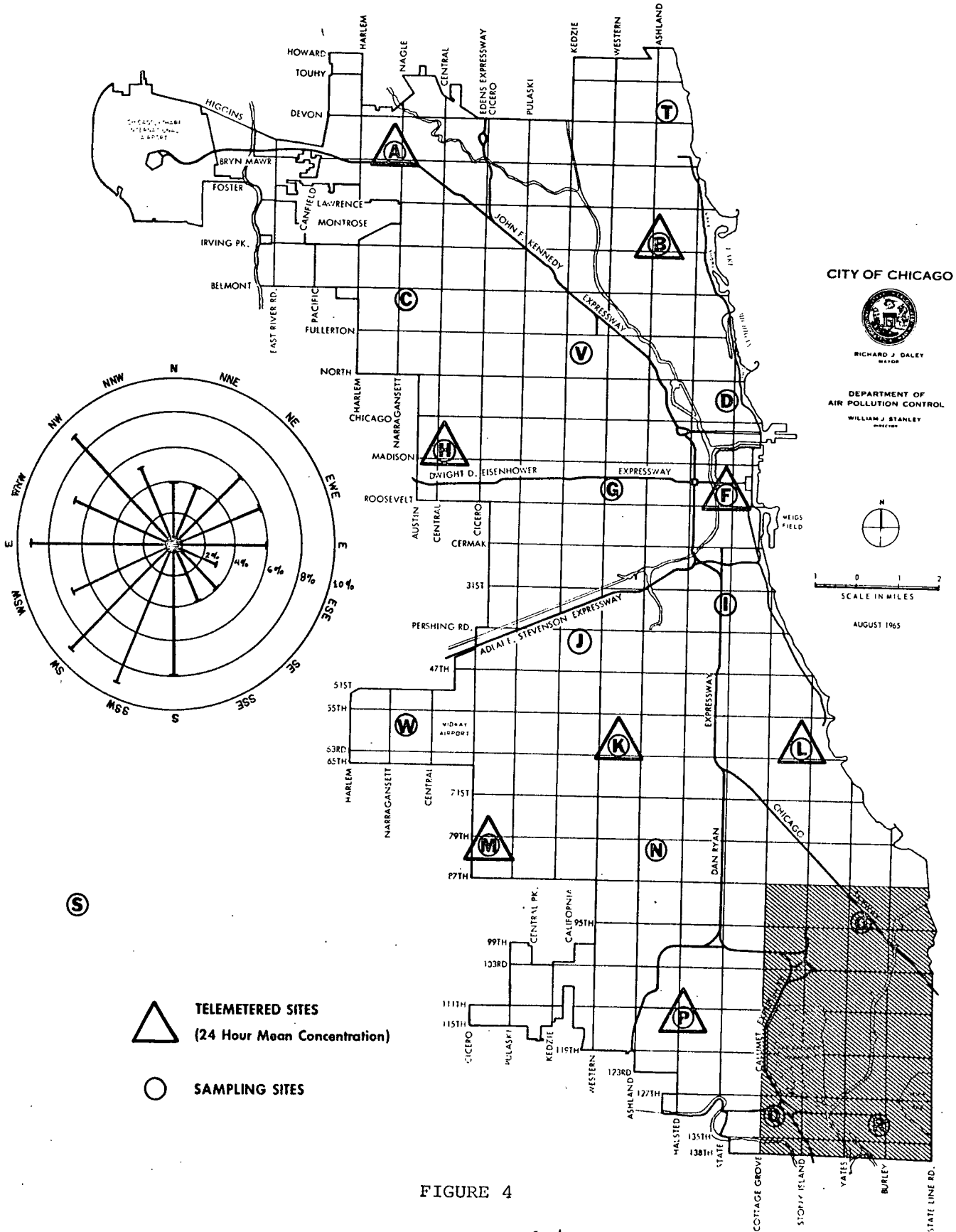


FIGURE 4

85

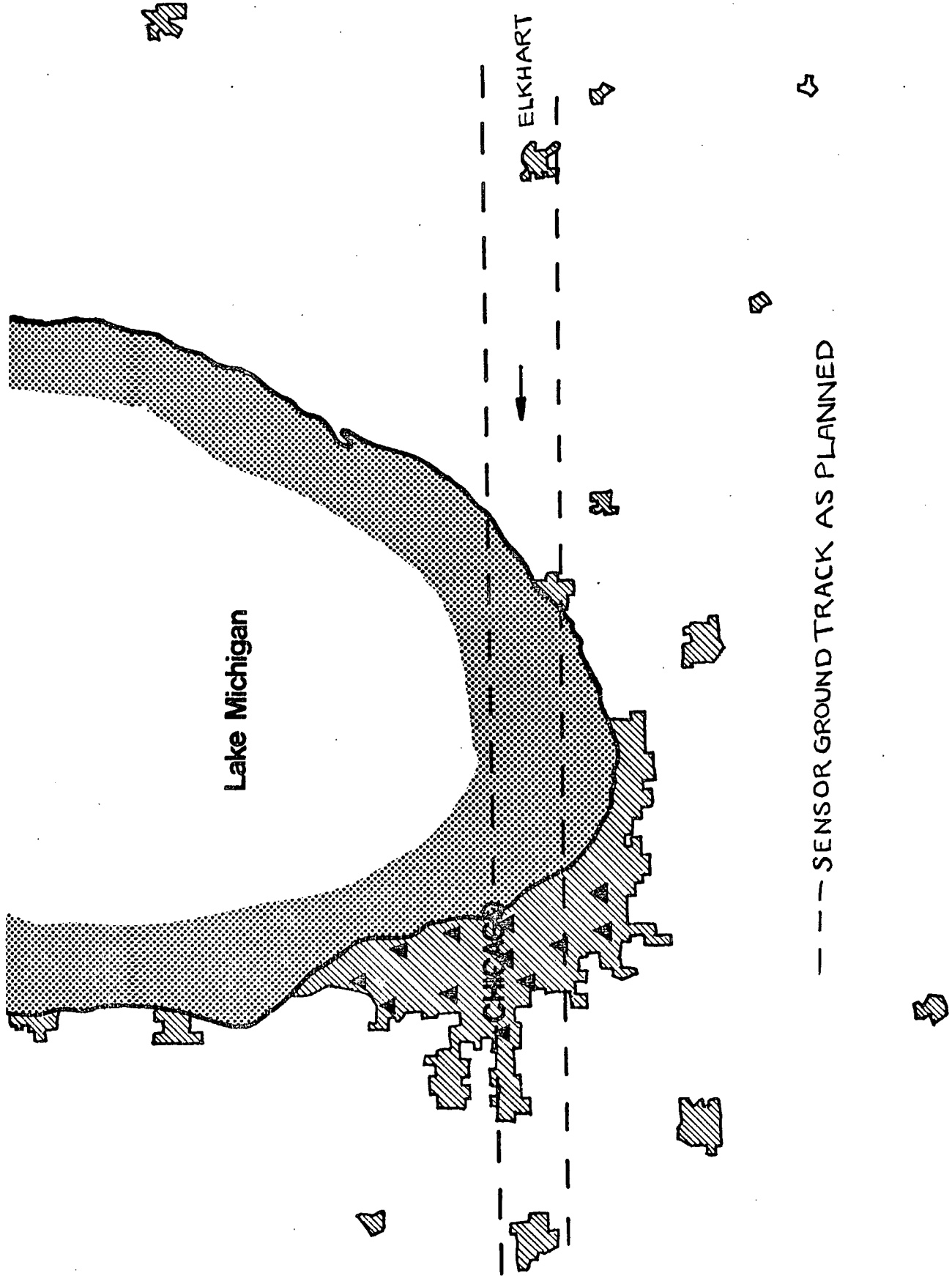


FIGURE 5

QI SOURCE

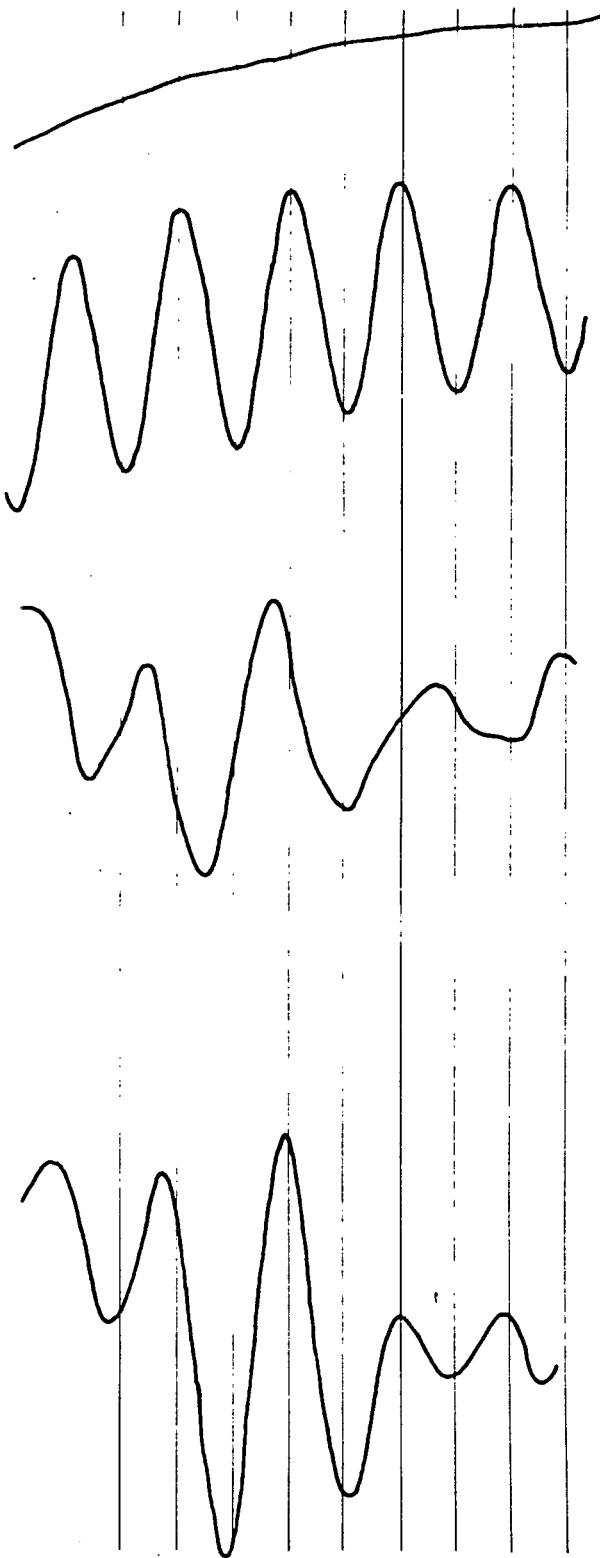
QI SOURCE  
+ 250 ppm-m SO<sub>2</sub>

SKY SOURCE

SKY SOURCE  
+ SO<sub>2</sub> (250 ppm-m)

SO<sub>2</sub> CORRELATION SCANS  
(SHORT  $\lambda$ )

FIGURE 6



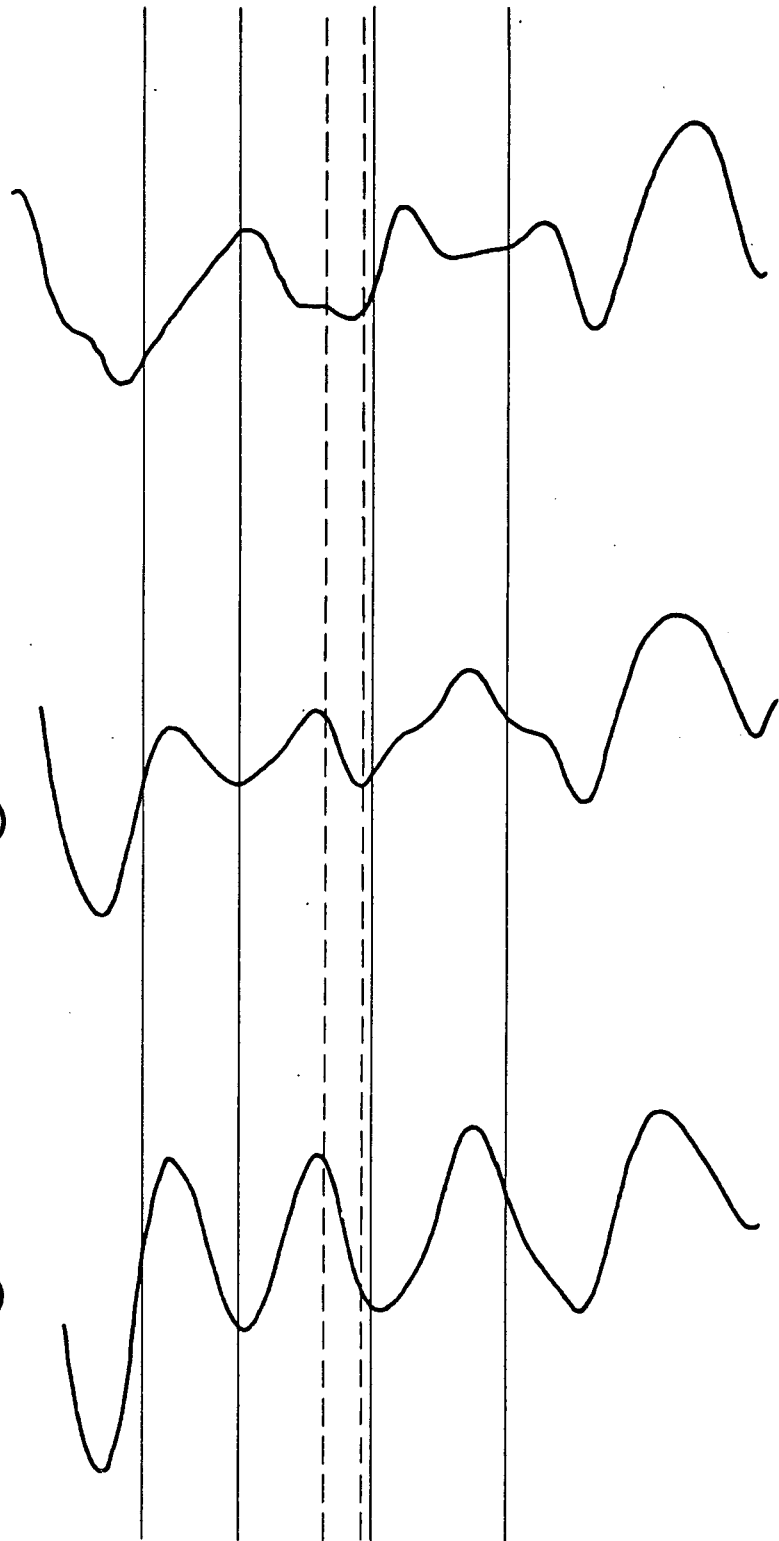
SKY SOURCE

SKY SOURCE  
+SO<sub>2</sub> (250 ppm-m)

SKY SOURCE  
+SO<sub>2</sub> (604 ppm-m)

# SO<sub>2</sub> CORRELATION SCANS

(LONG  $\lambda$ ) FIGURE 7



Total Updraft Sky cover

Reproduced from  
 best available copy.

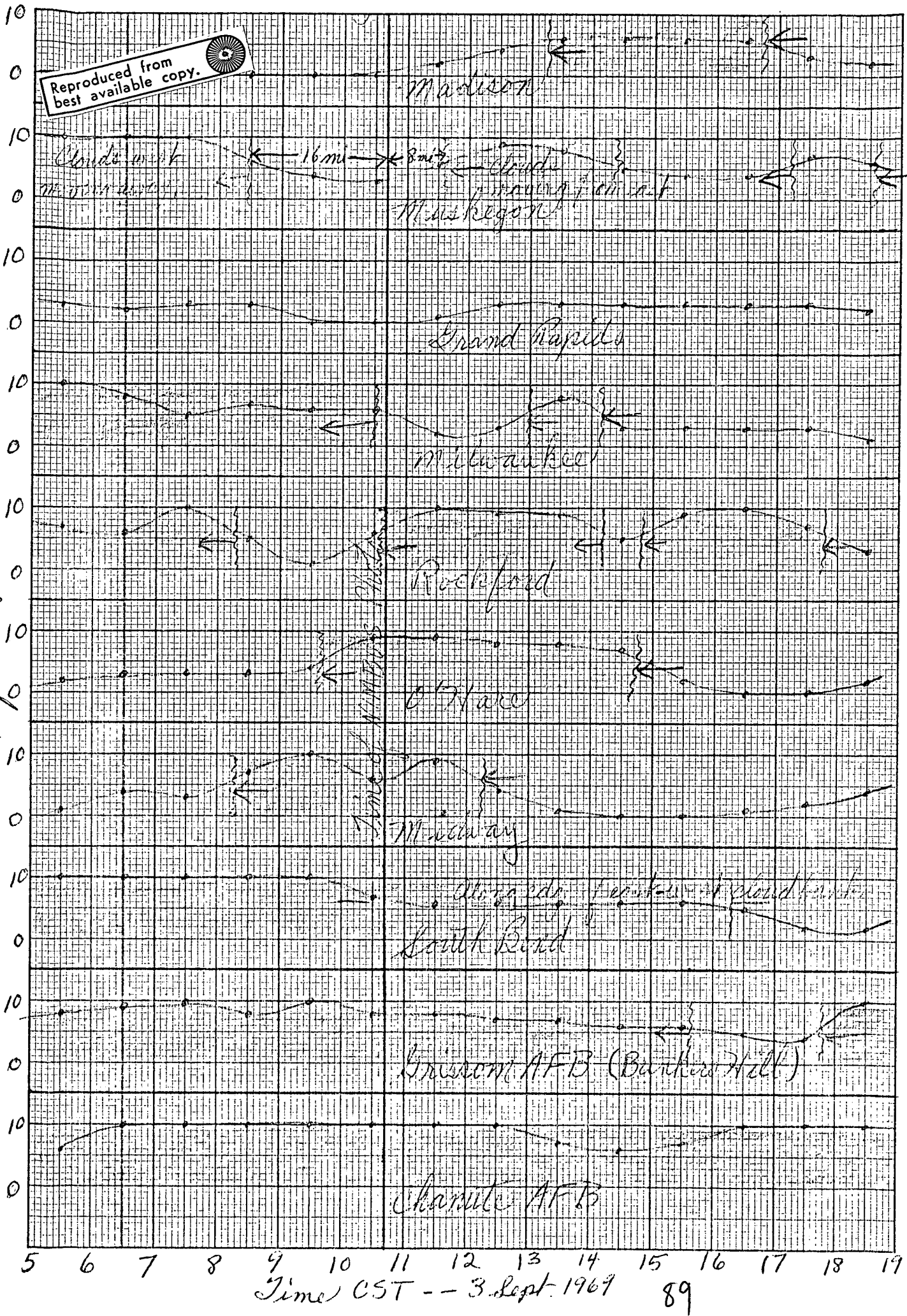
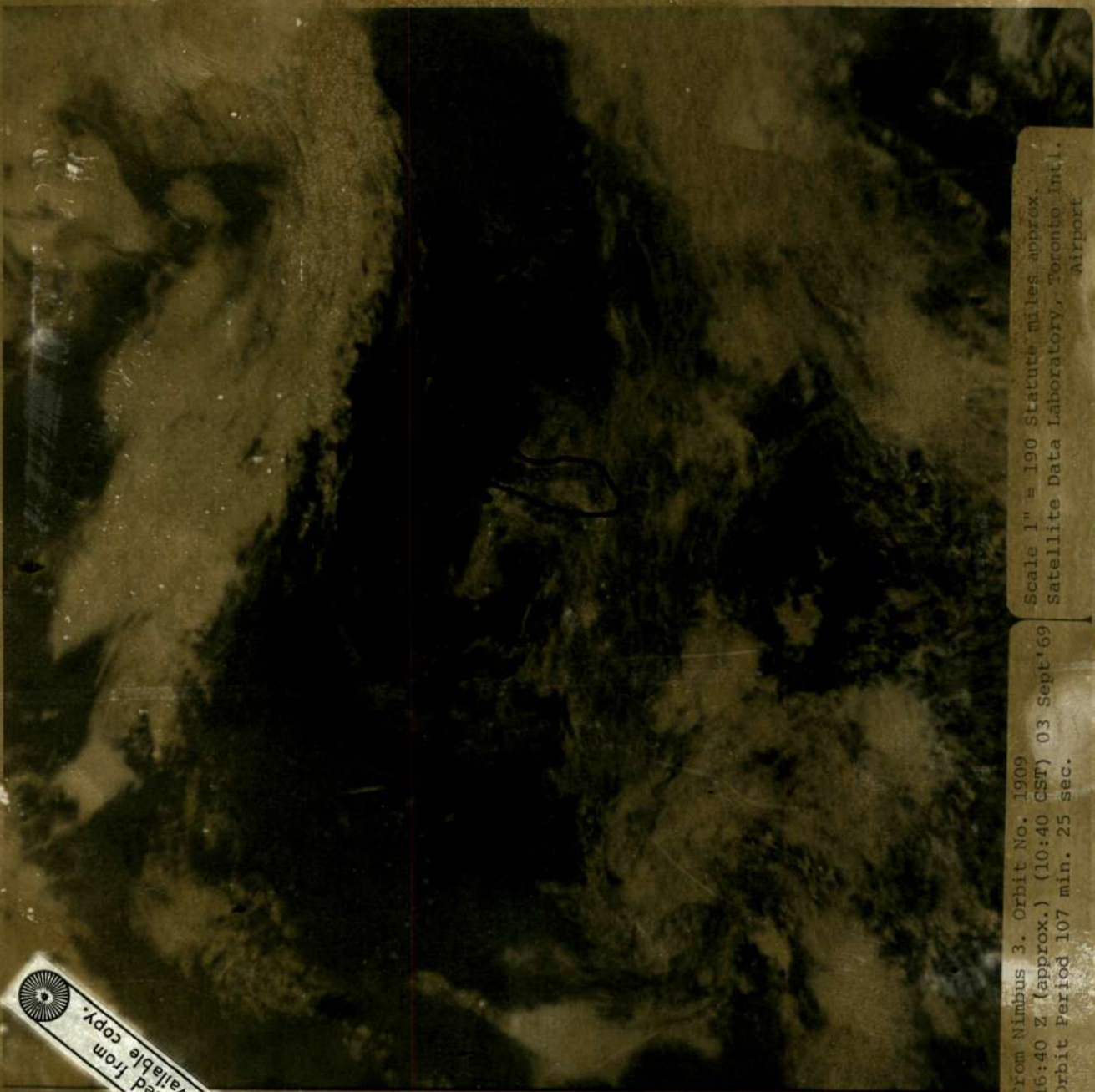


FIGURE 7.1

A BETTER QUALITY OF THESE  
PAGES IS REPRODUCED AT THE END OF  
THIS PUBLICATION



Reproduced from  
best available copy.

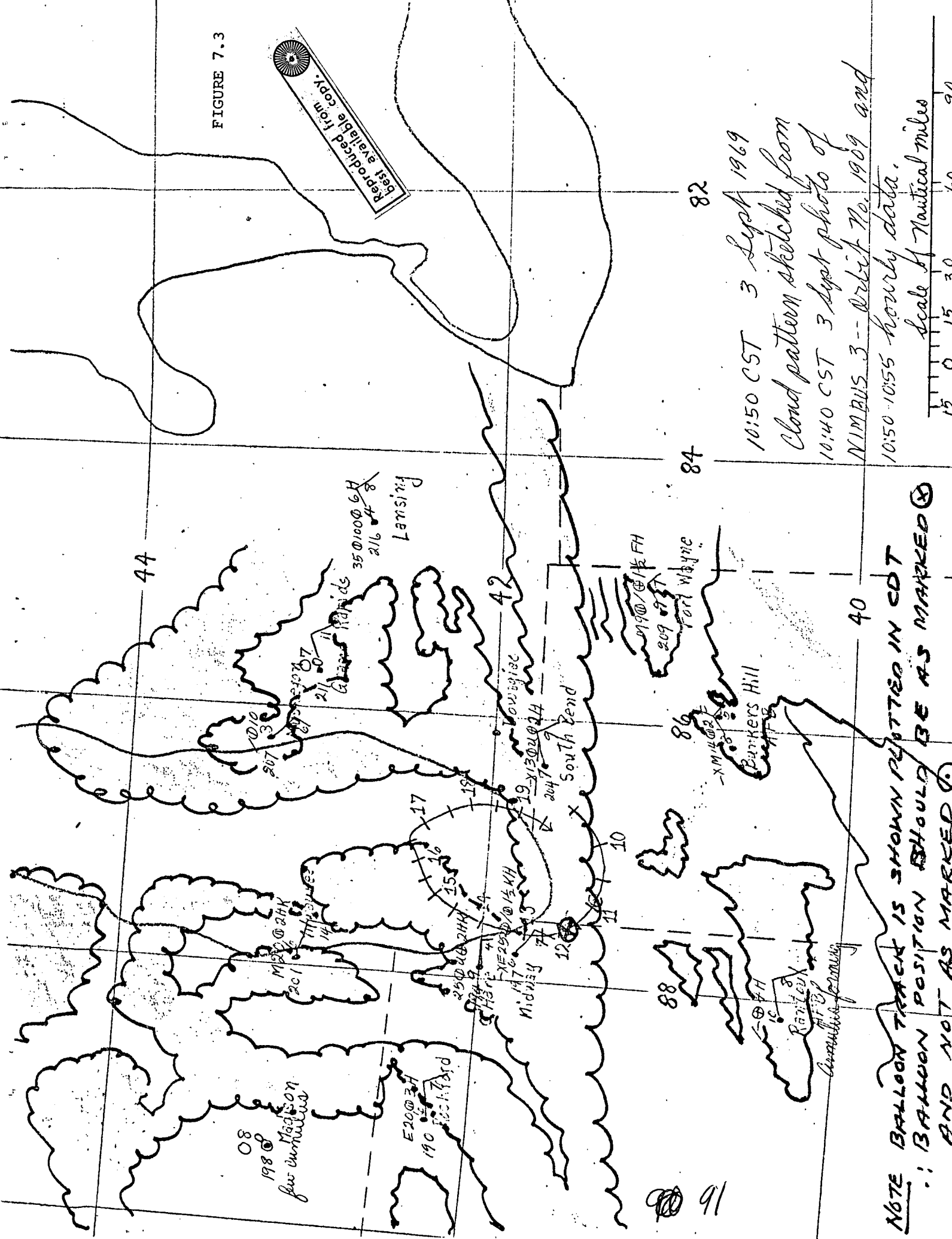
from Nimbus 3. Orbit No. 1909  
16:40 Z (approx.) (10:40 CST) 03 Sept '69  
Orbit Period 107 min. 25 sec.

Scale 1" = 190 Statute miles approx.  
Satellite Data Laboratory, Toronto Intl.  
Airport

FIGURE 7.2

FIGURE 7.3

Reproduced from:  
Best available copy.

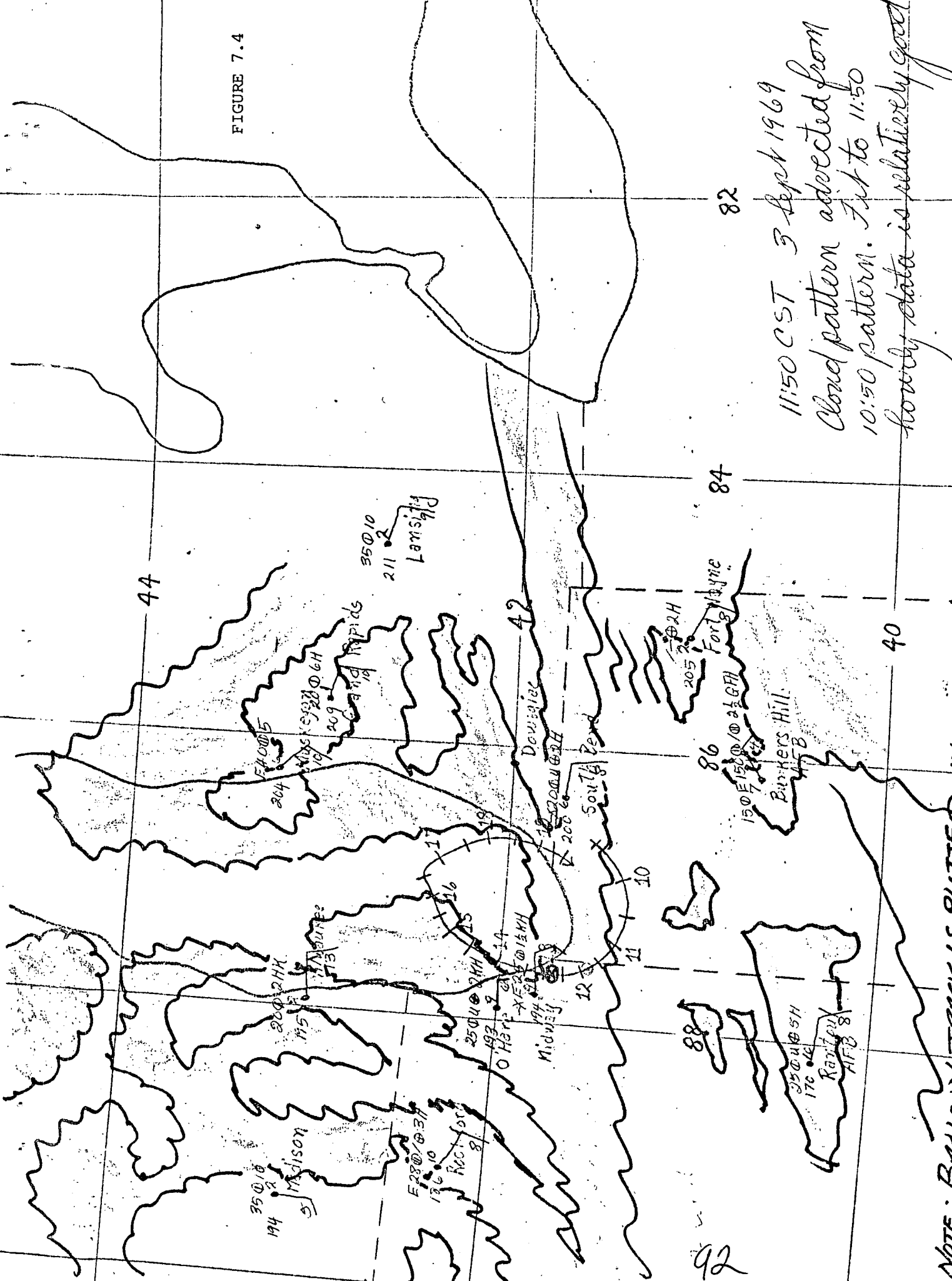


10:50 CST 3 Sept 1969  
 Cloud pattern sketched from  
 10:40 CST 3 Sept photo of  
 NIMBUS 3 -- Orbit No. 1909 and  
 10:50-10:55 hourly data.

Scale of Nautical miles  
 15 0 15 30 60 90

NOTE BALLOON TRACK IS SHOWN PLOTTED IN CDT  
 ∴ BALLOON POSITION SHOULD BE AS MARKED ⊙  
 AND NOT AS MARKED ⊗

FIGURE 7.4

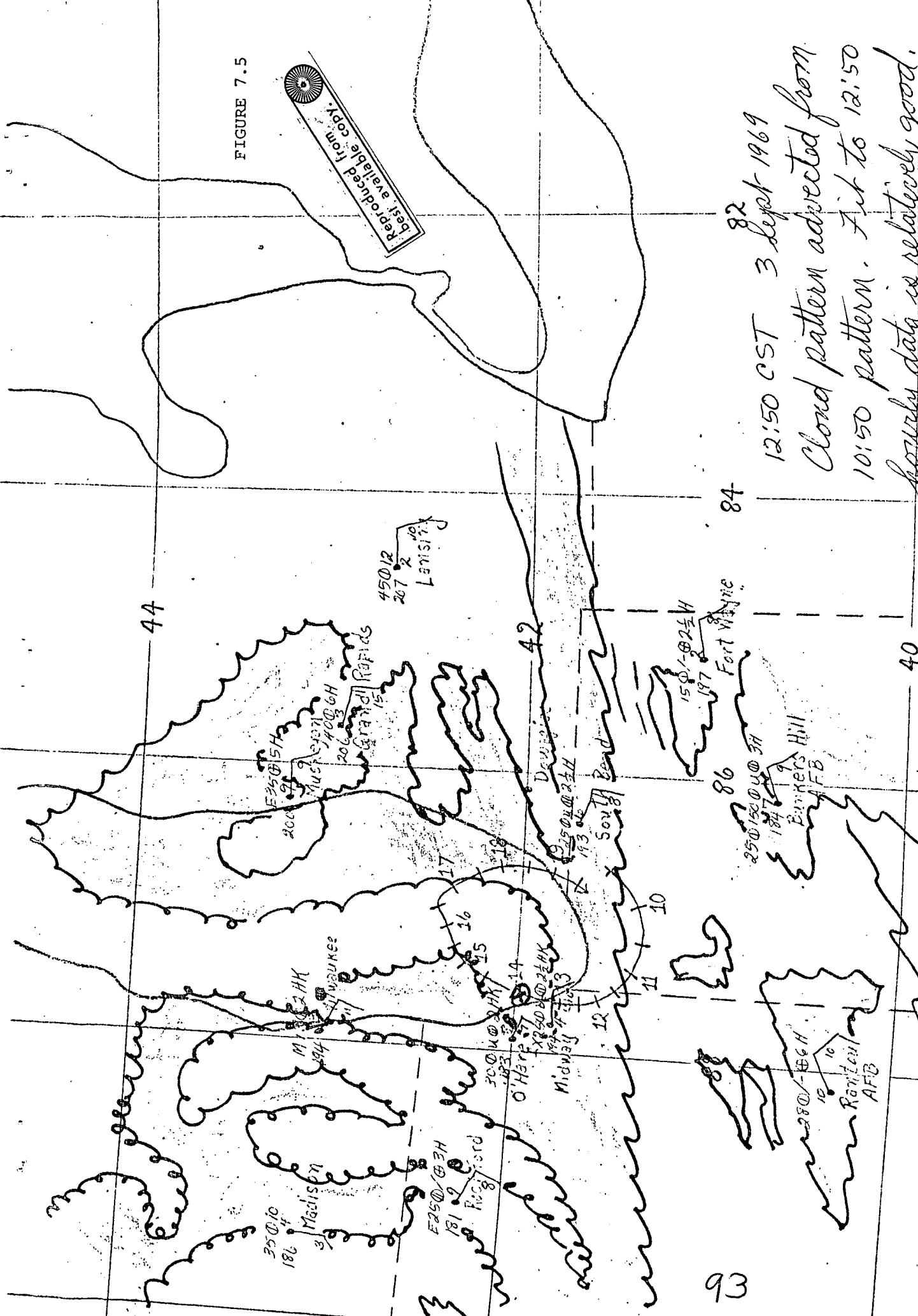


11:50 CST 3 Sept 1969  
 Cloud pattern advected from  
 10:50 pattern. Fit to 11:50  
 hourly data is relatively good.

NOTE: BALLOON TRACK IS PLOTTED IN C.D.T.  
 !! BALLOON POSITION SHOULD BE AS MARKED AND NOT O

FIGURE 7.5

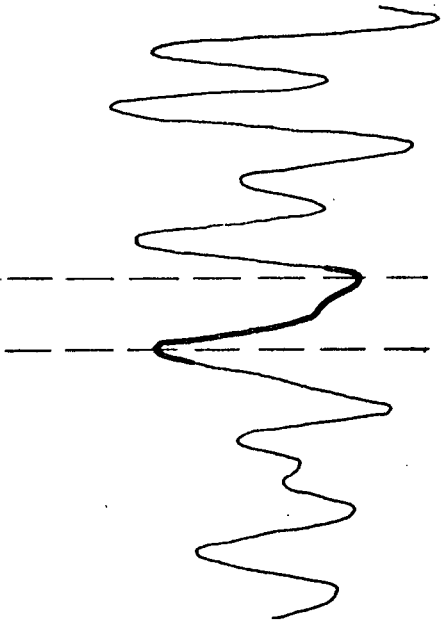
Reproduced from Best available copy.



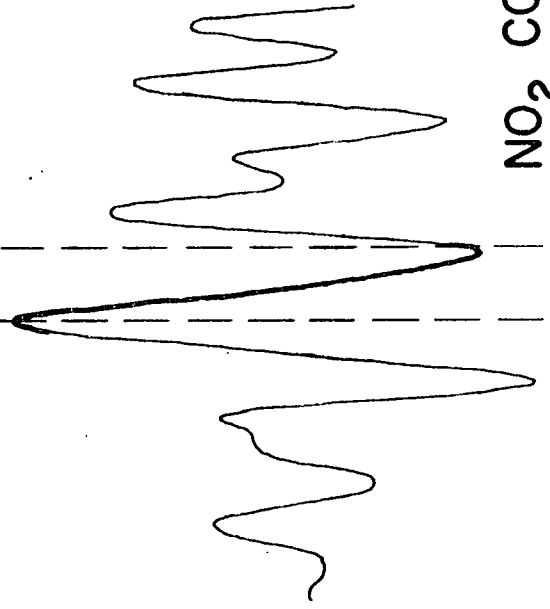
12:50 CST 3 Sept 1969 82  
 Cloud pattern advected from  
 10:50 pattern. Fit to 12:50  
 hourly data is relatively good.

NOTE BALLOON TRACK IS SHOWN PLOTTED IN CDT  
 ∴ BALLOON POSITION SHOULD BE AS MARKED (X) AND NOT AS (O)

LOW NO<sub>2</sub> BURDEN



HIGH (600 ppm-m)  
NO<sub>2</sub> BURDEN



NO<sub>2</sub> CORRELATION SCANS

FIGURE 8

76

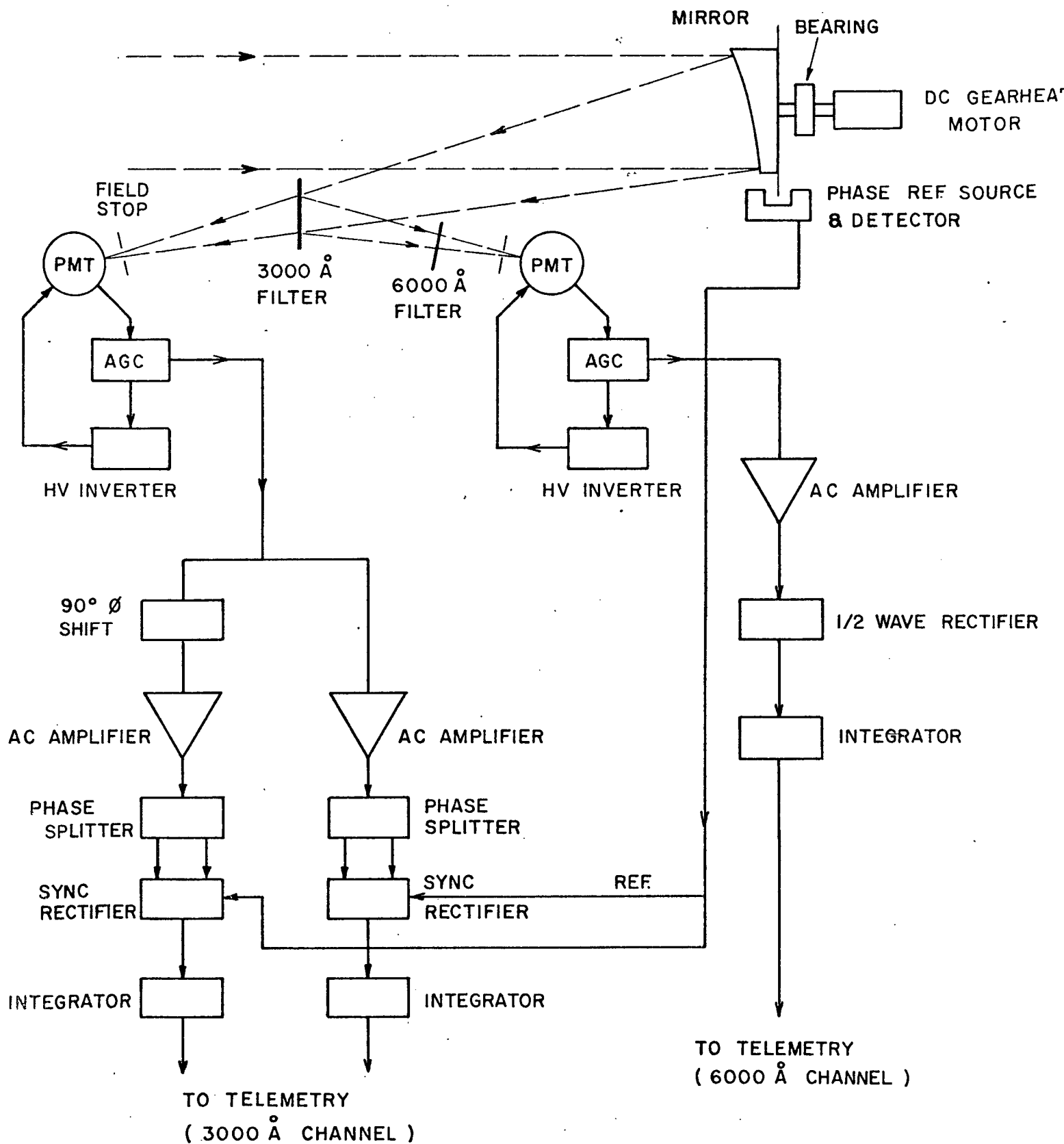
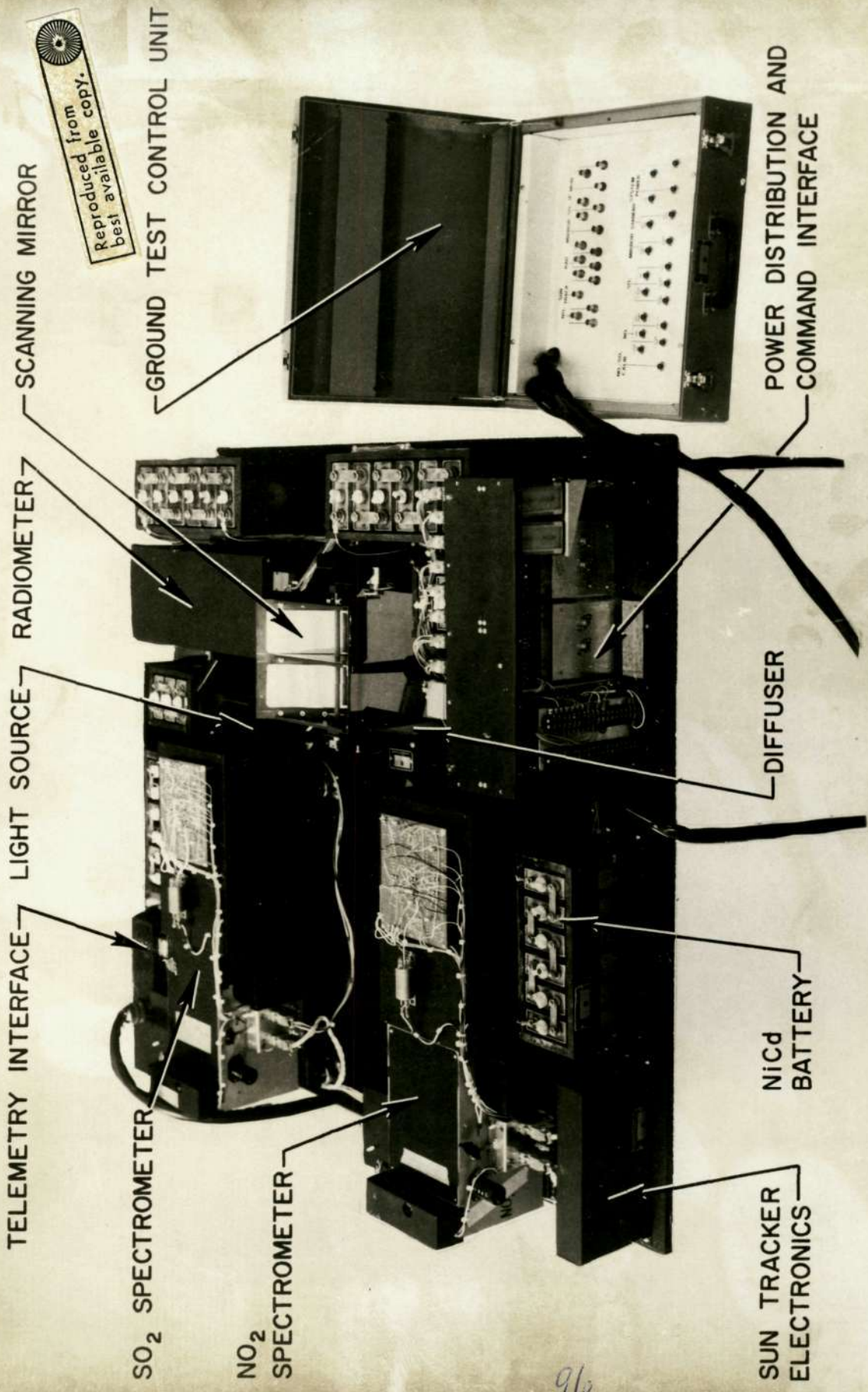


FIG. 9  
 RADIOMETER  
 BLOCK DIAGRAM

95



TELEMETRY INTERFACE

LIGHT SOURCE

RADIOMETER

SCANNING MIRROR

SO<sub>2</sub> SPECTROMETER

NO<sub>2</sub> SPECTROMETER

GROUND TEST CONTROL UNIT

SUN TRACKER ELECTRONICS

NiCd BATTERY

DIFFUSER

POWER DISTRIBUTION AND COMMAND INTERFACE

Reproduced from best available copy.

96

NASA/BARRINGER RESEARCH/NCAR/WINZEN SCIENTIFIC PAYLOAD FOR HIGH ALTITUDE BALLOON MEASUREMENTS OF AIR POLLUTION

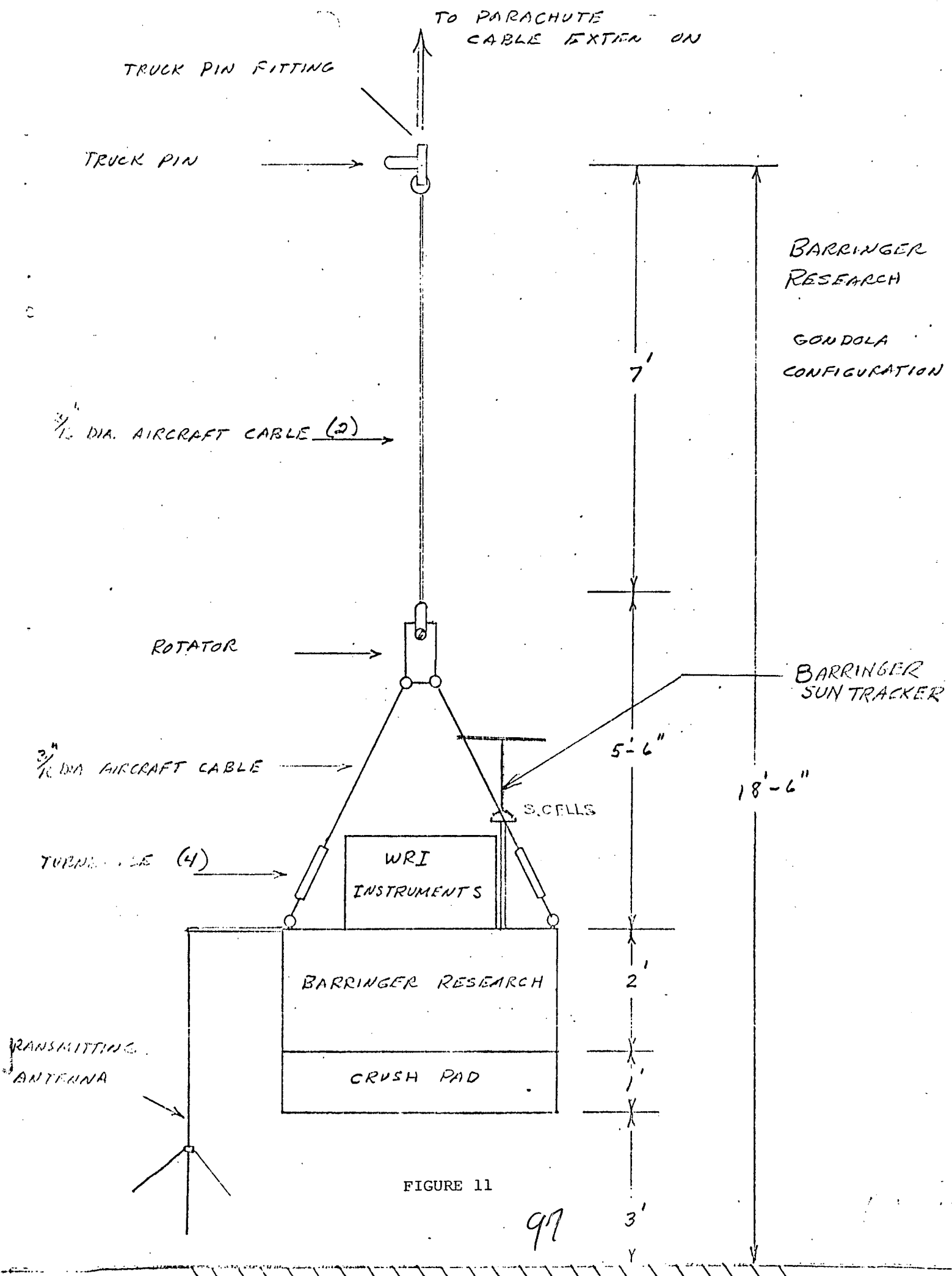
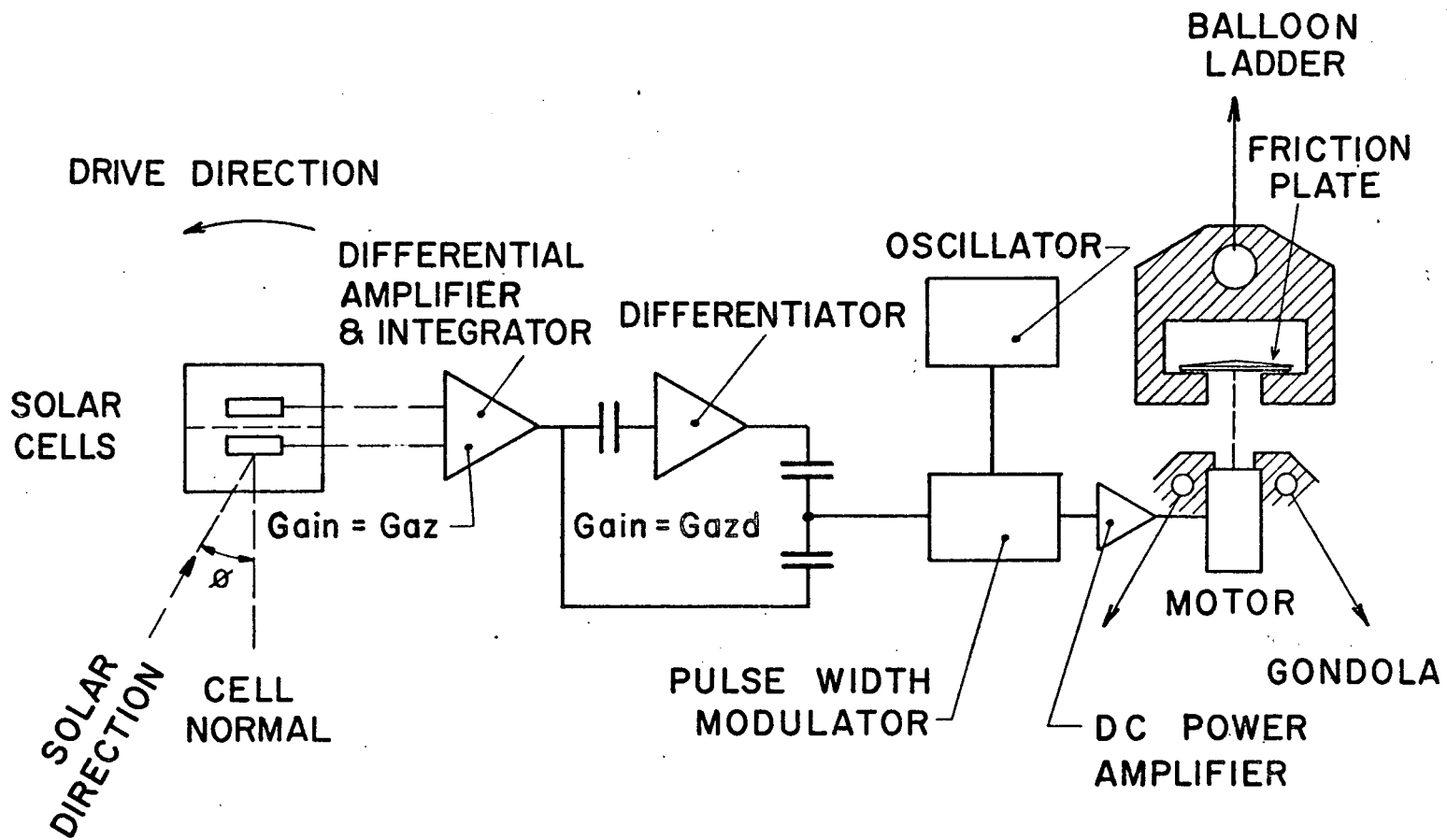


FIGURE 11

97



SUN TRACKER  
BLOCK DIAGRAM

FIG. 12

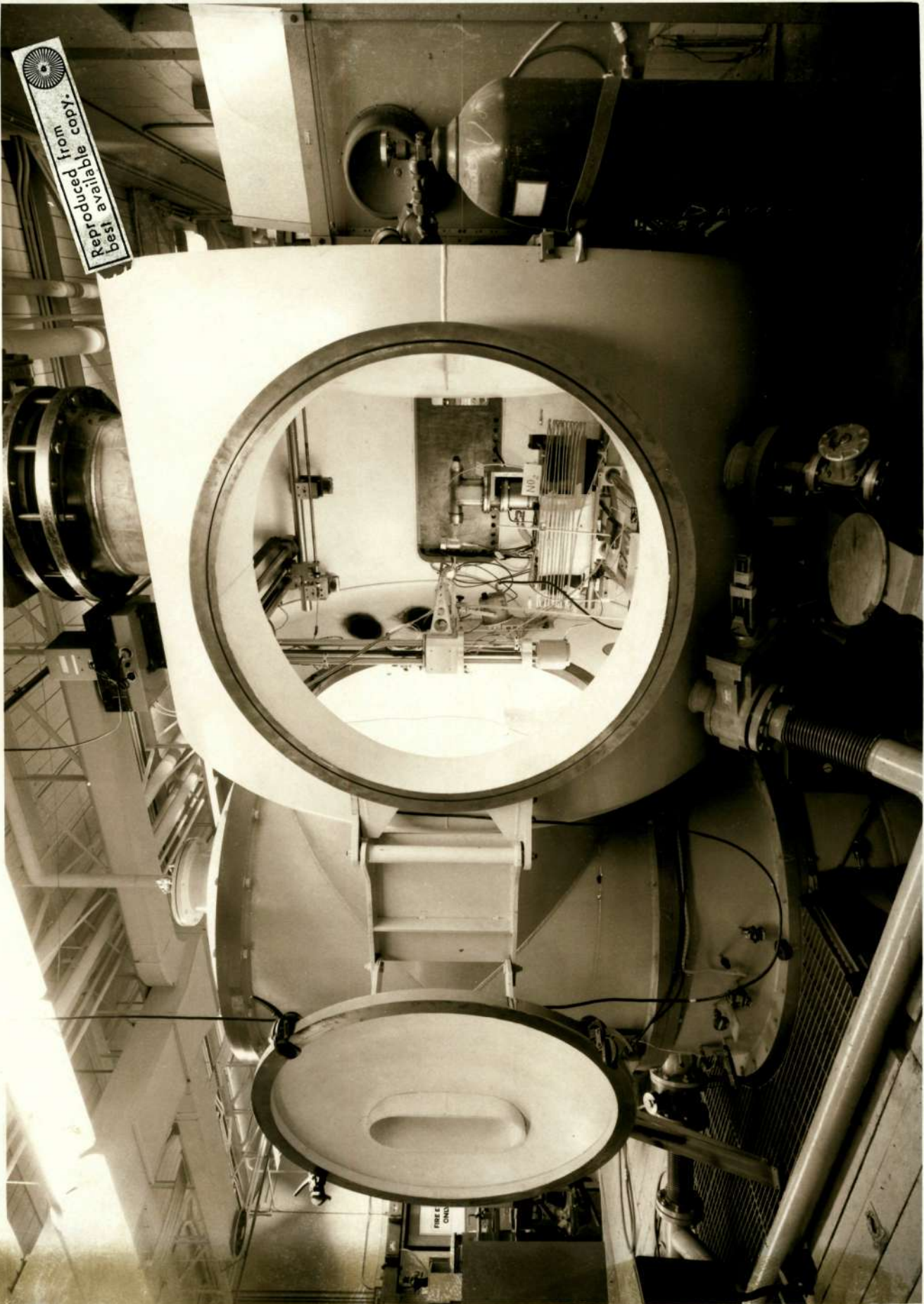
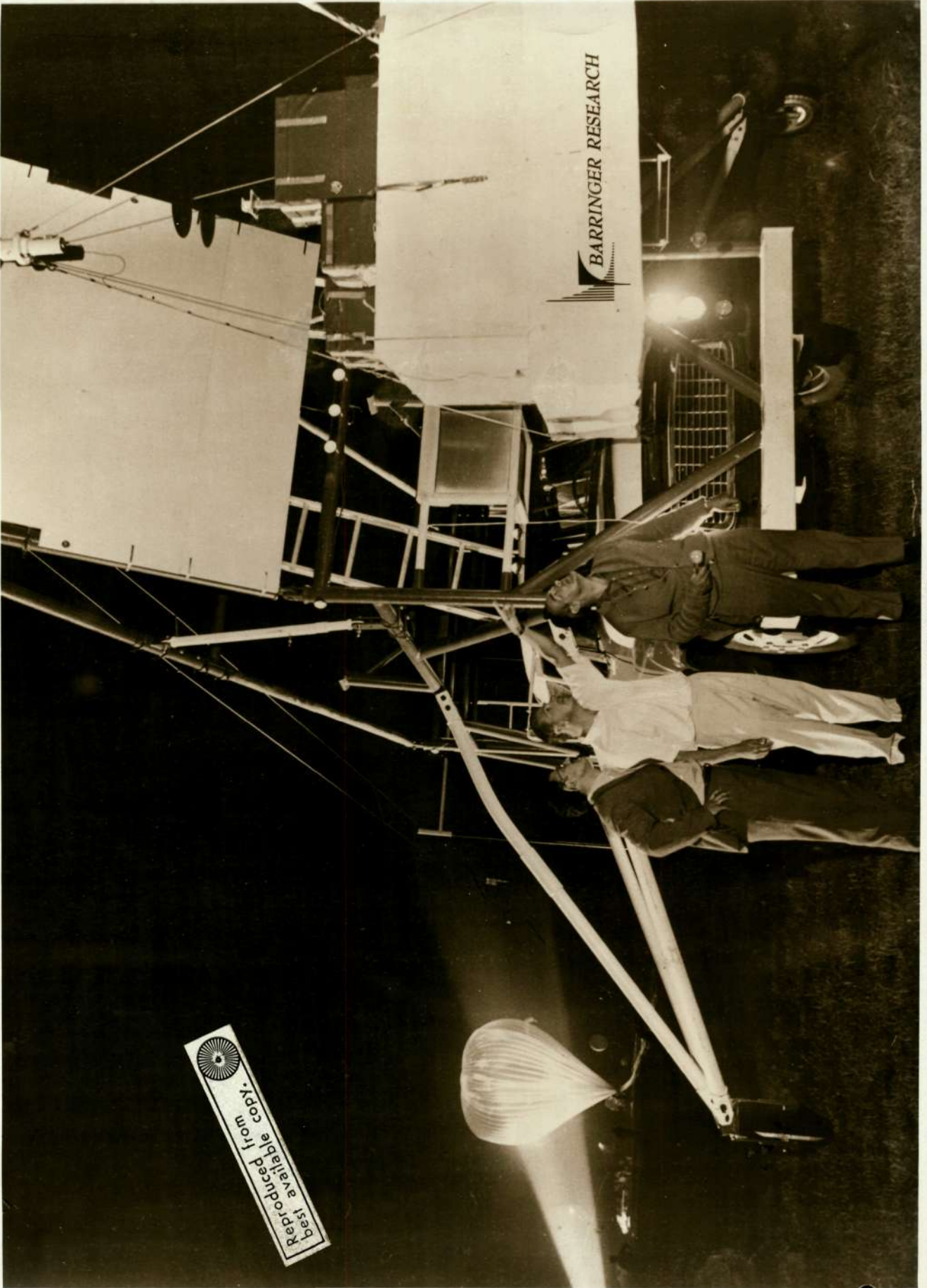


FIGURE 13



Reproduced from  
best available copy.

FIGURE 16

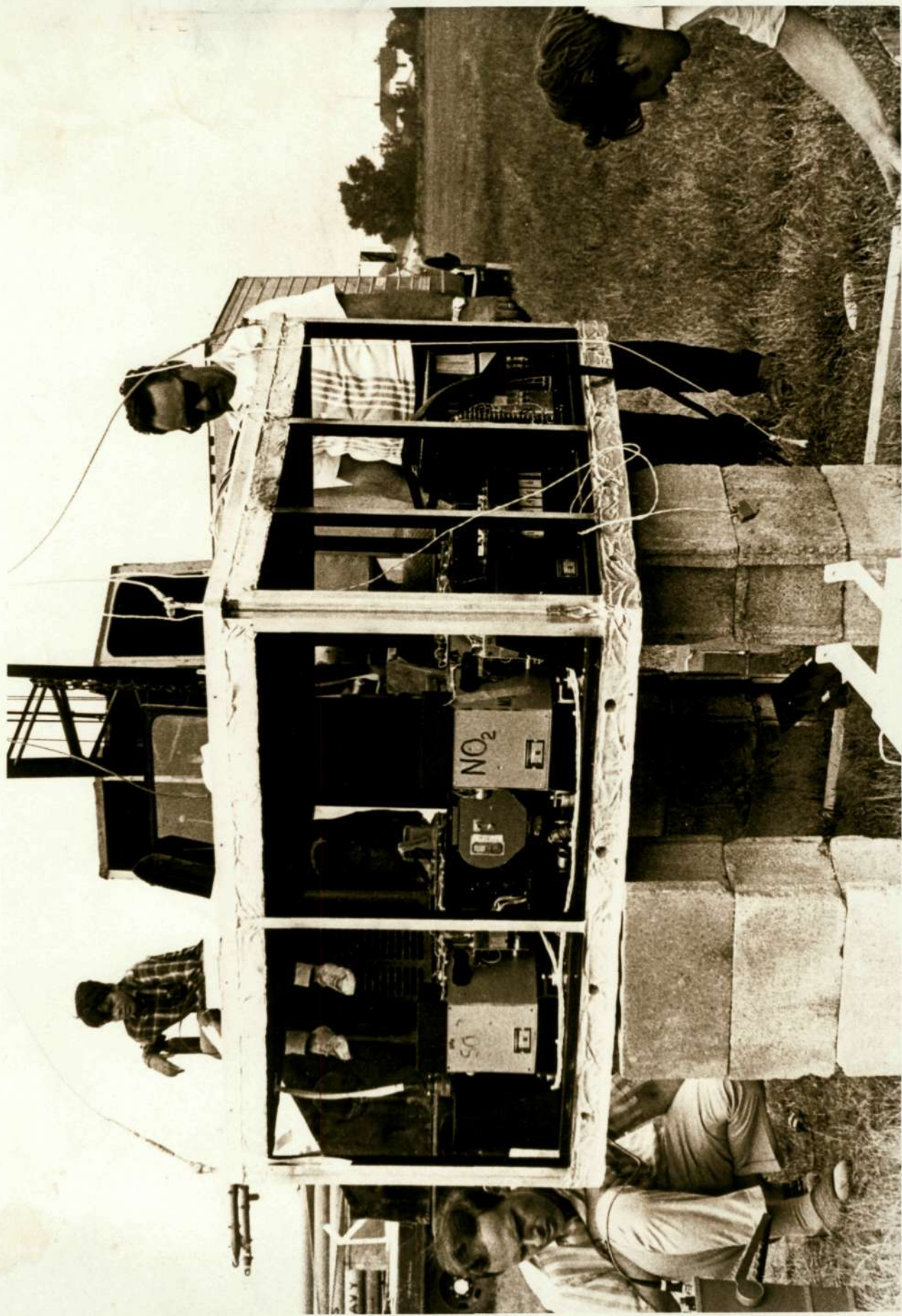


FIGURE 14



Reproduced from  
Best available copy.

FIGURE 15

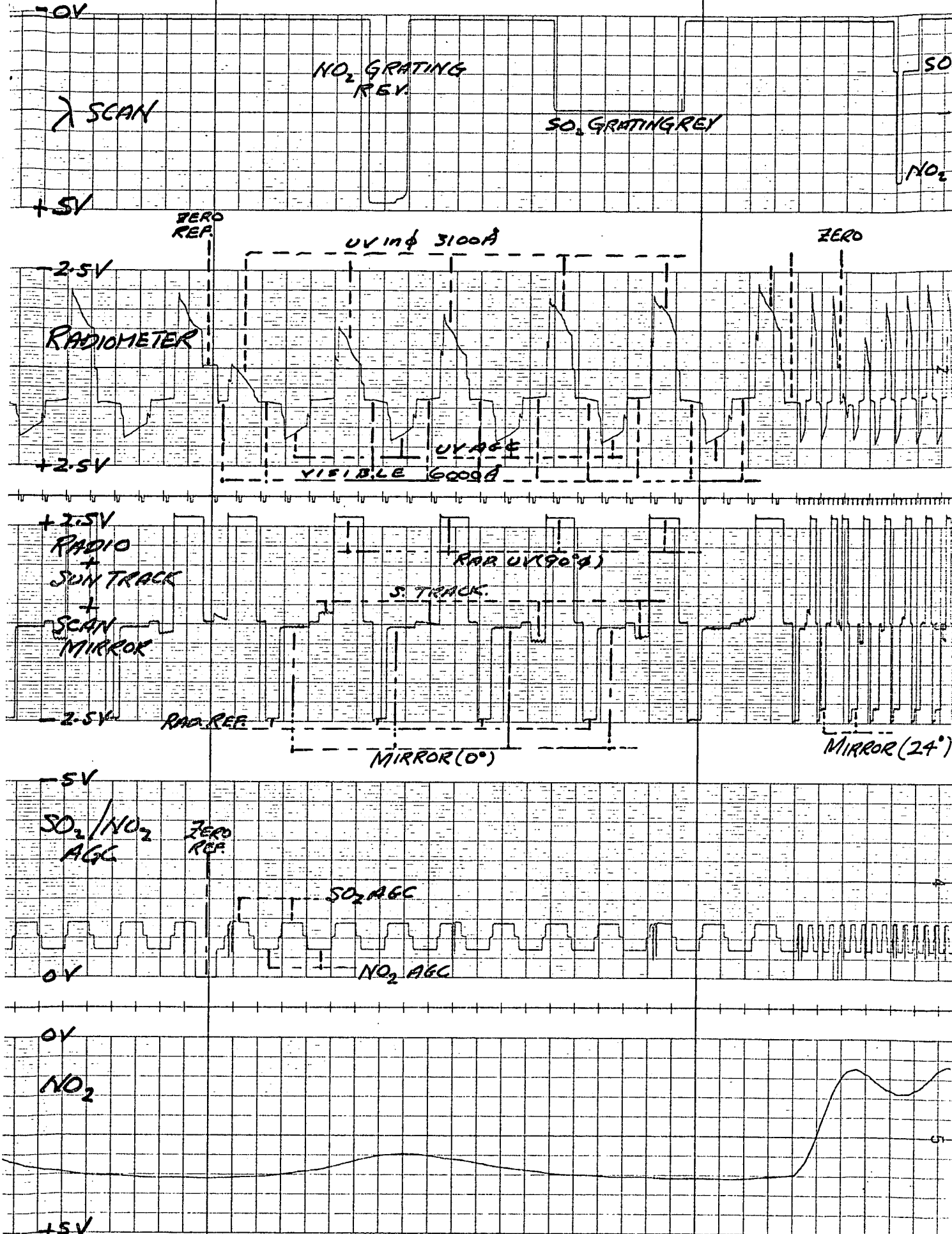
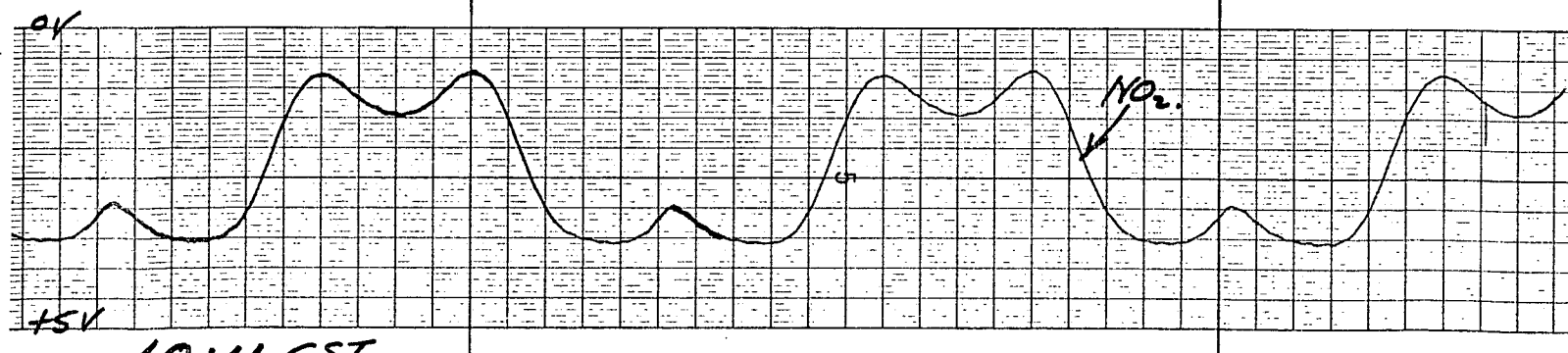
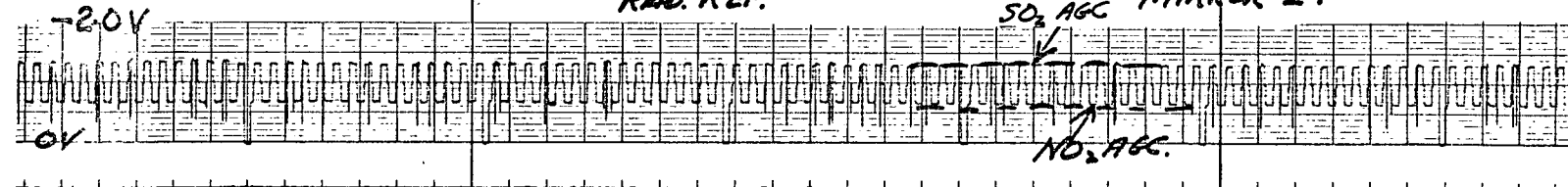
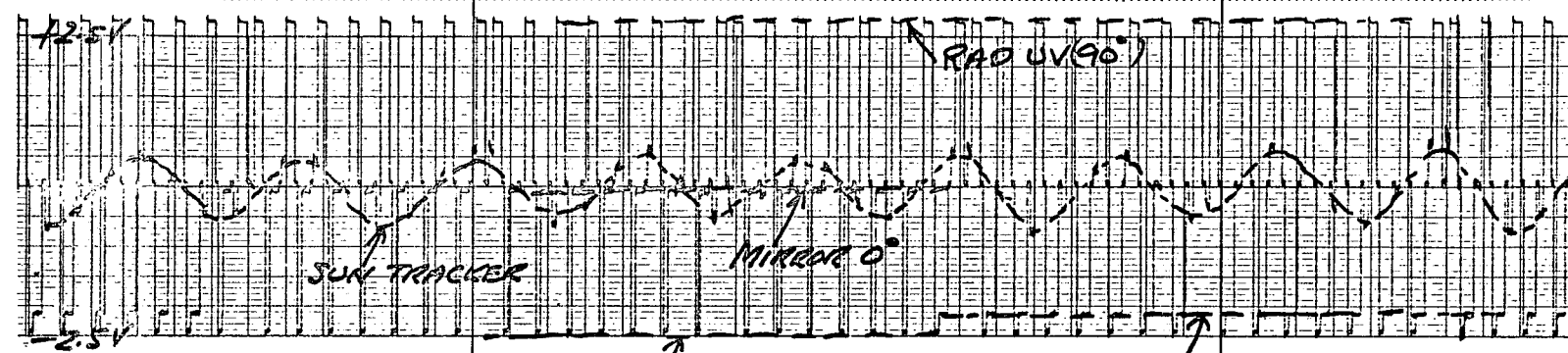
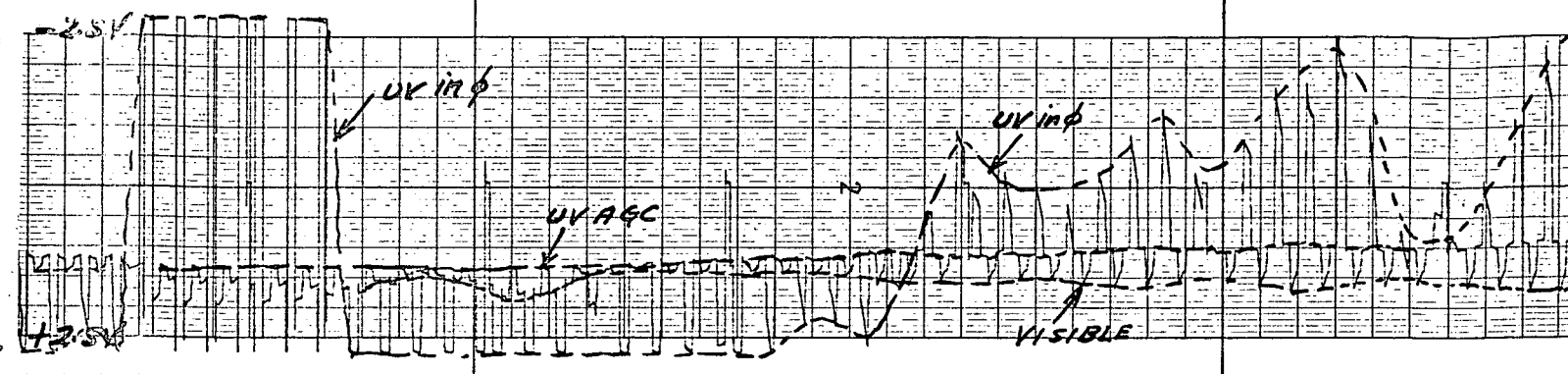
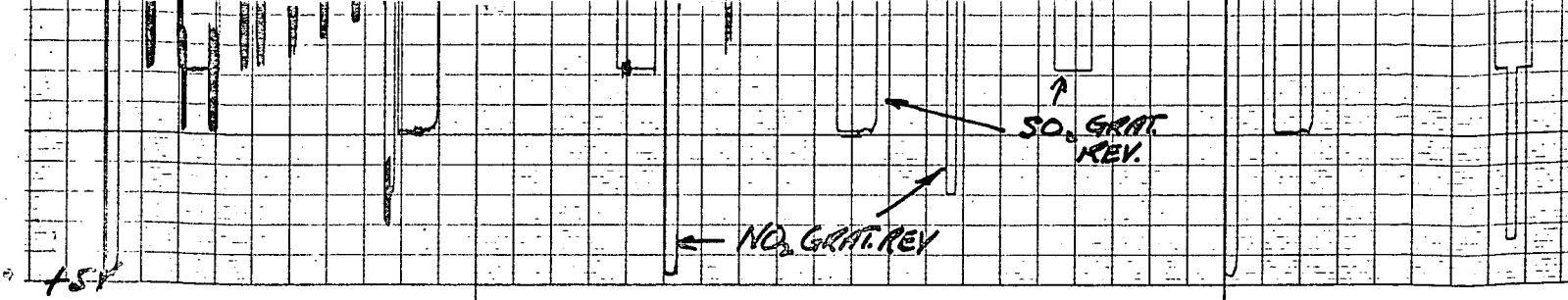
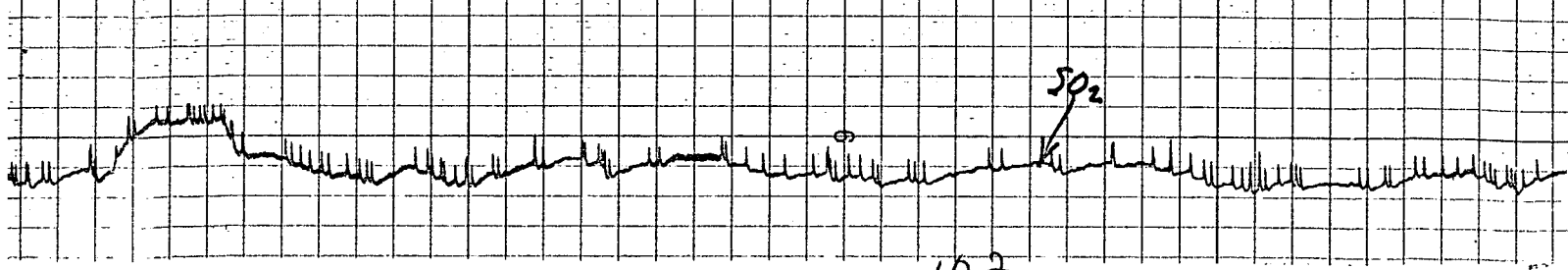


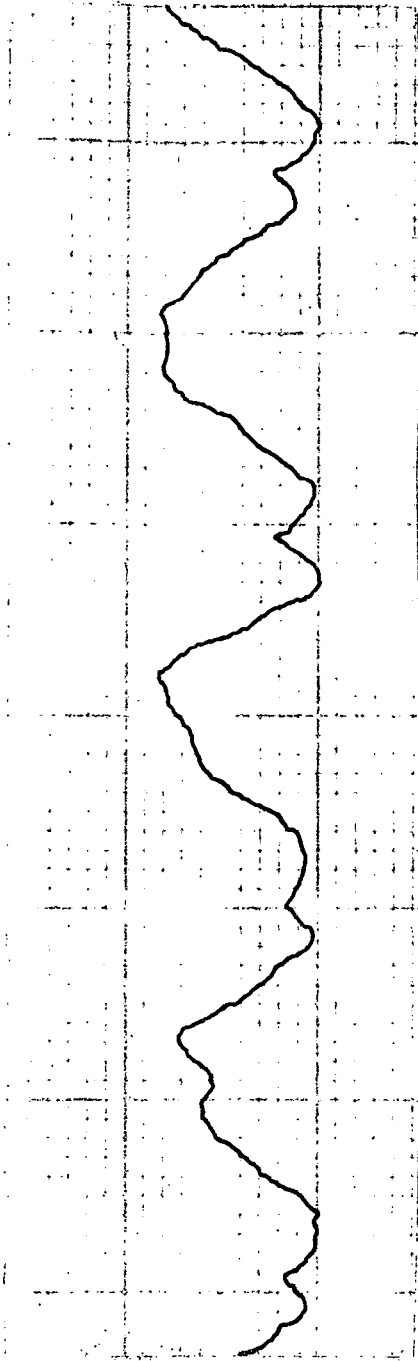
FIGURE 17



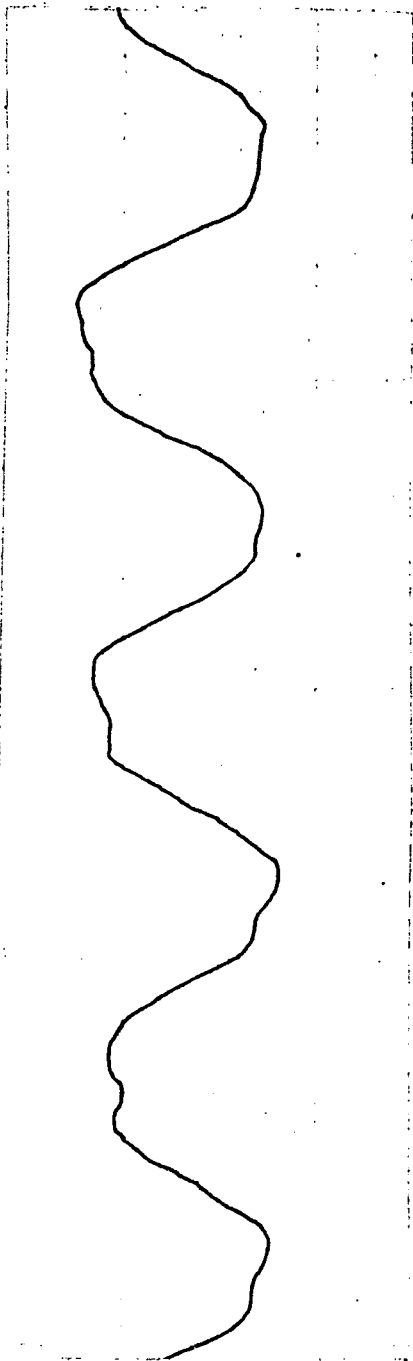
10:11 CST  
CHART SPEED 1mm/SEC.

FIGURE 18

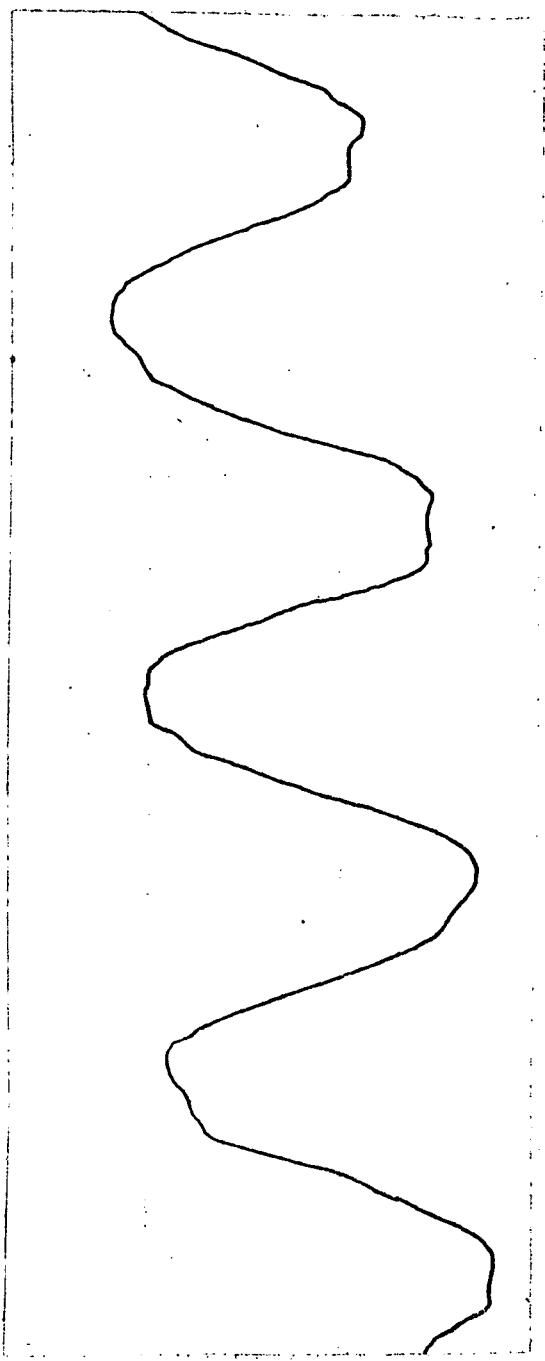




**LOW SO<sub>2</sub> BURDEN**



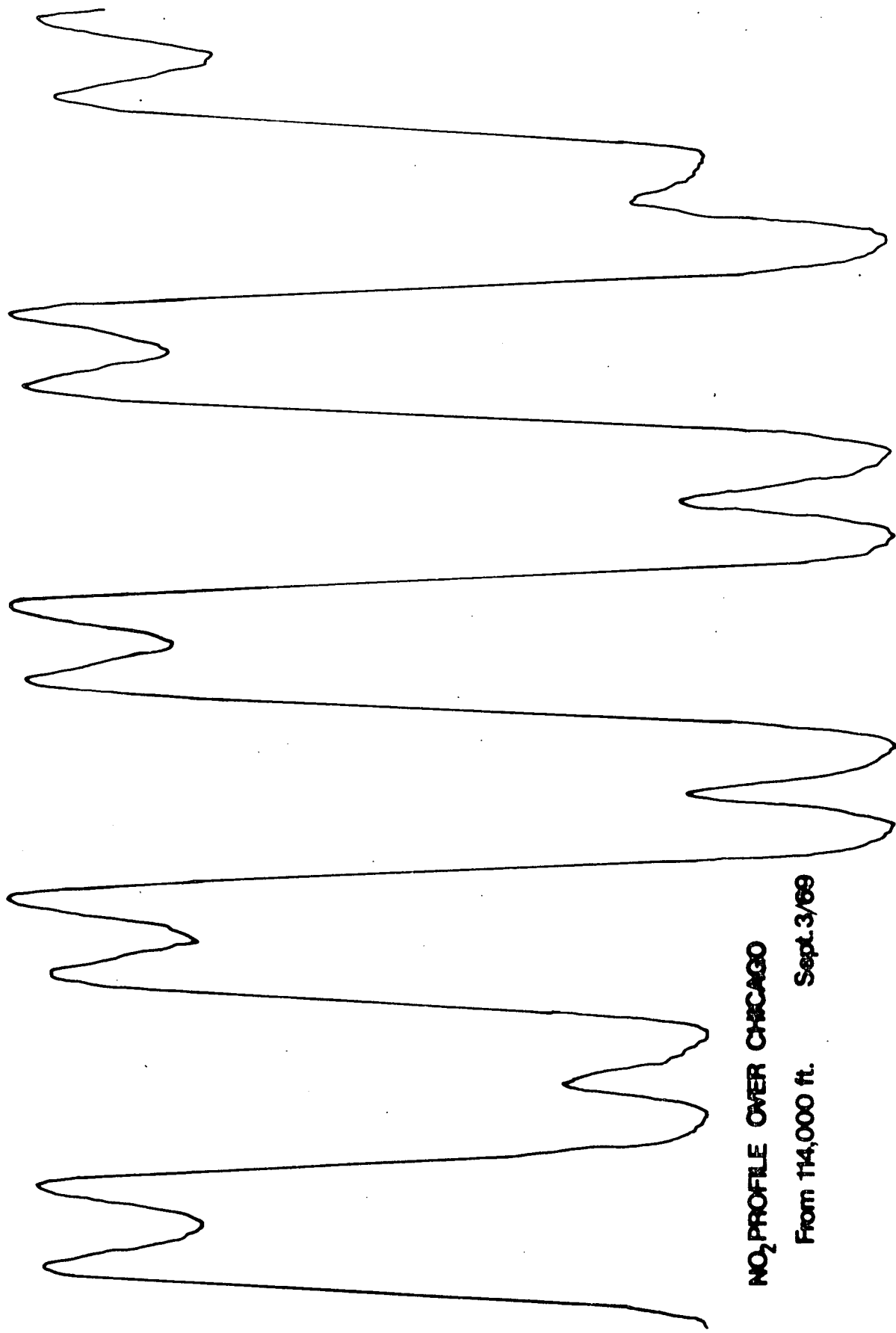
**11 ppm-m SO<sub>2</sub>**



**55 ppm-m SO<sub>2</sub>  
(REF CELL)**

**SO<sub>2</sub> SIGNAL OVER CHICAGO FROM 114,000 FT.**

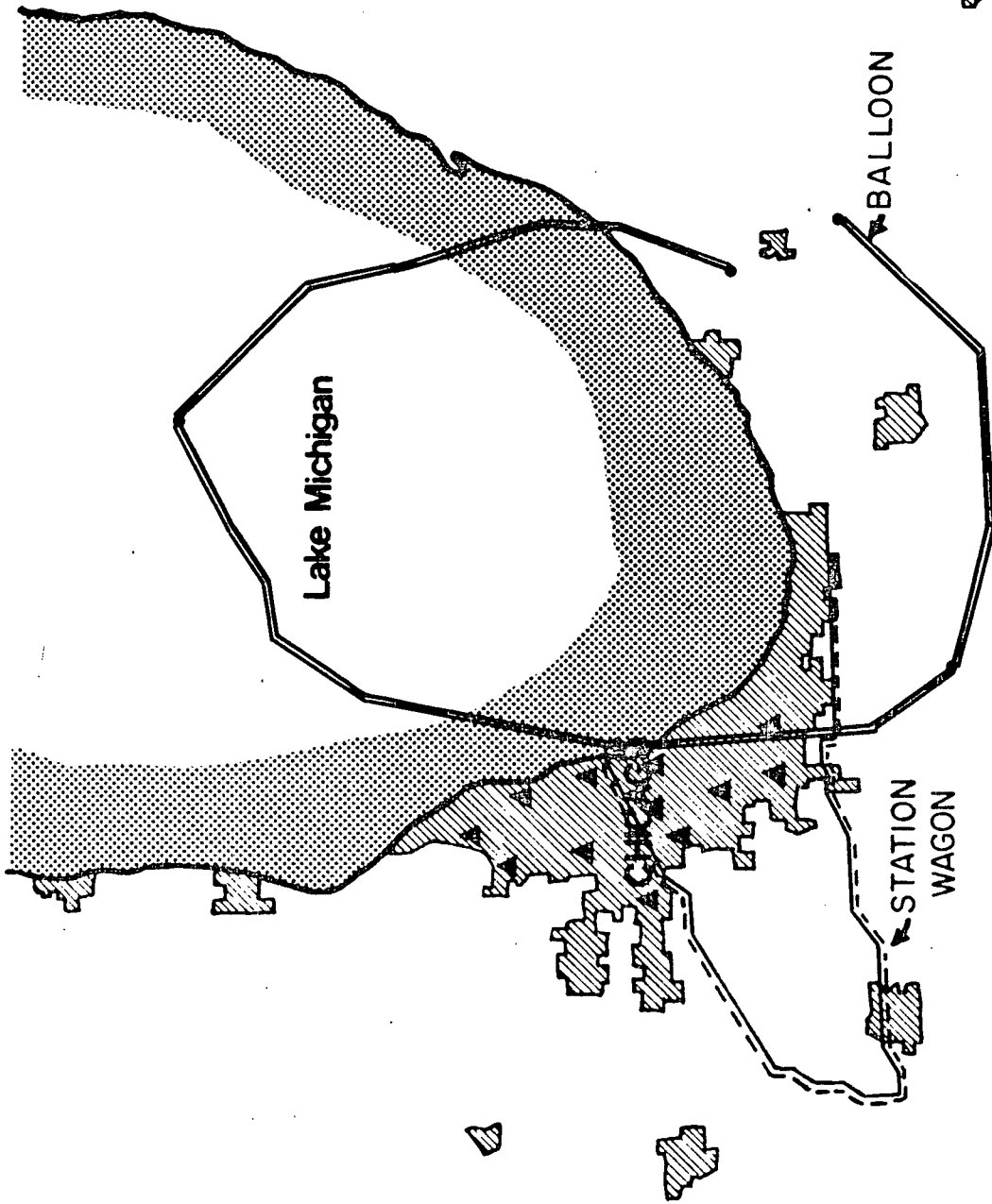
FIGURE 19



**NO<sub>2</sub> PROFILE OVER CHICAGO**  
From 114,000 ft.    Sept. 3/69

FIGURE 20

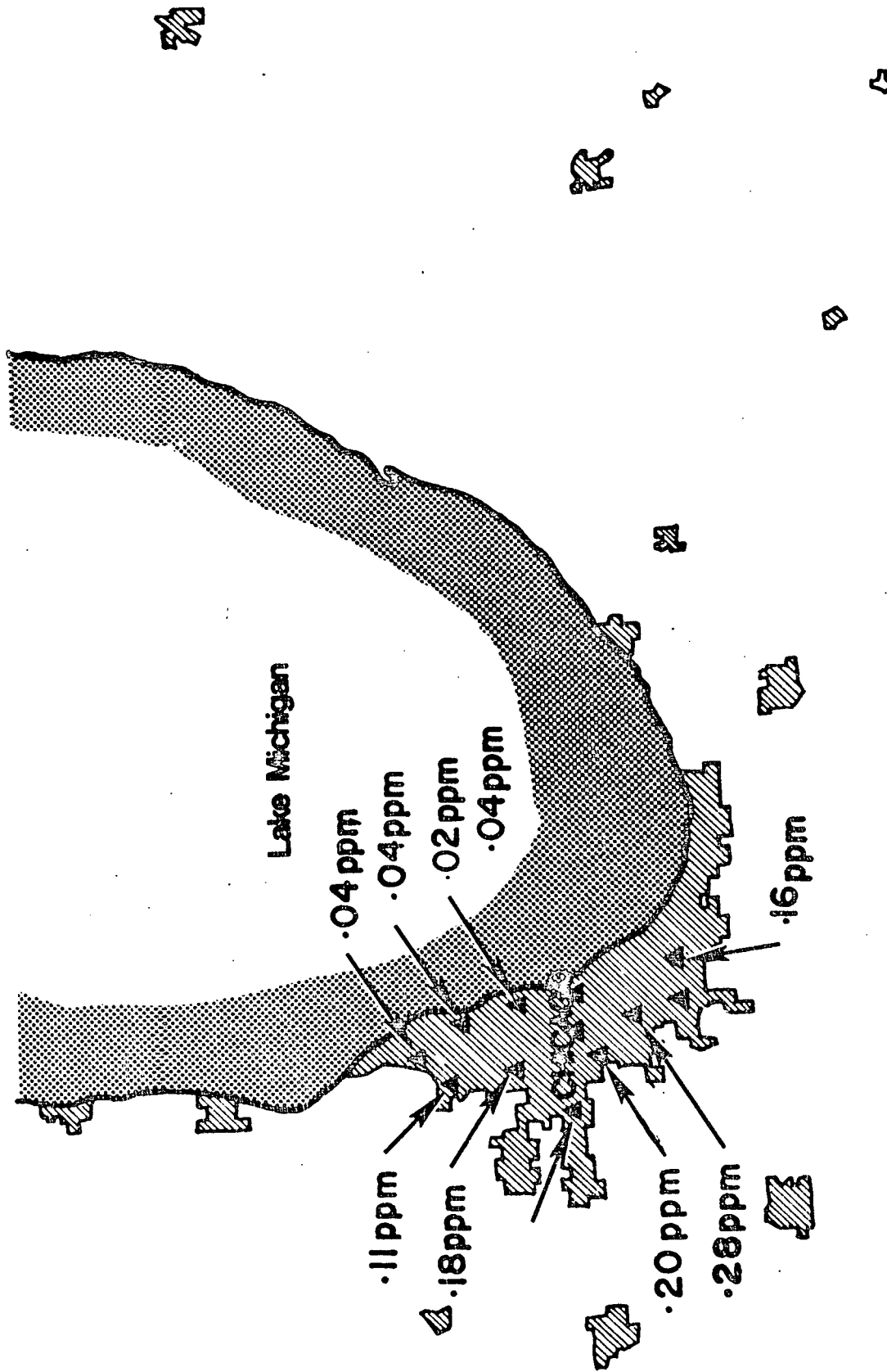
104



**BALLOON TRAJECTORY & STATION WAGON  
ROUTE**

SEPTEMBER 3rd 1969

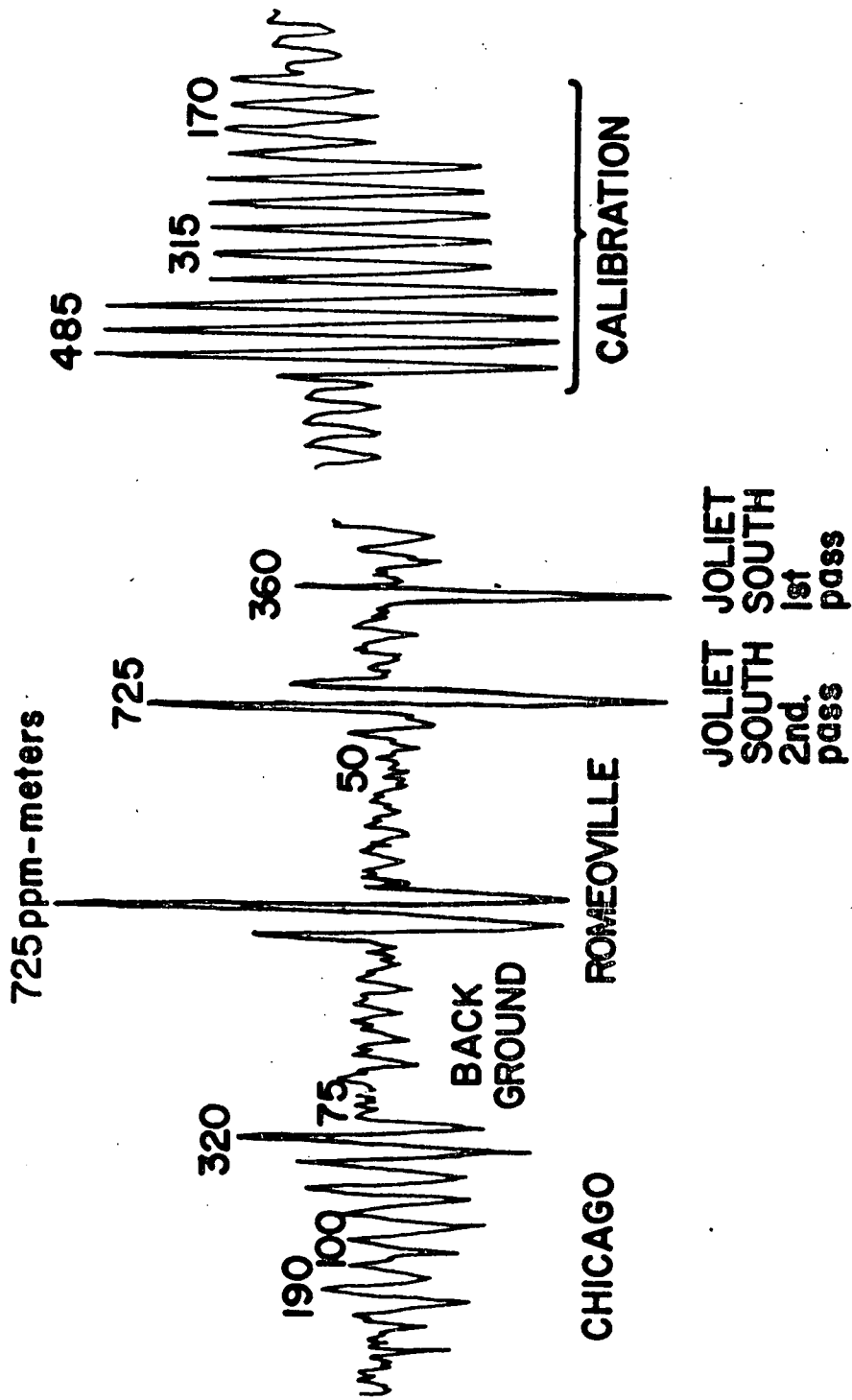
FIGURE 21



CHICAGO GROUND LEVEL SO<sub>2</sub>

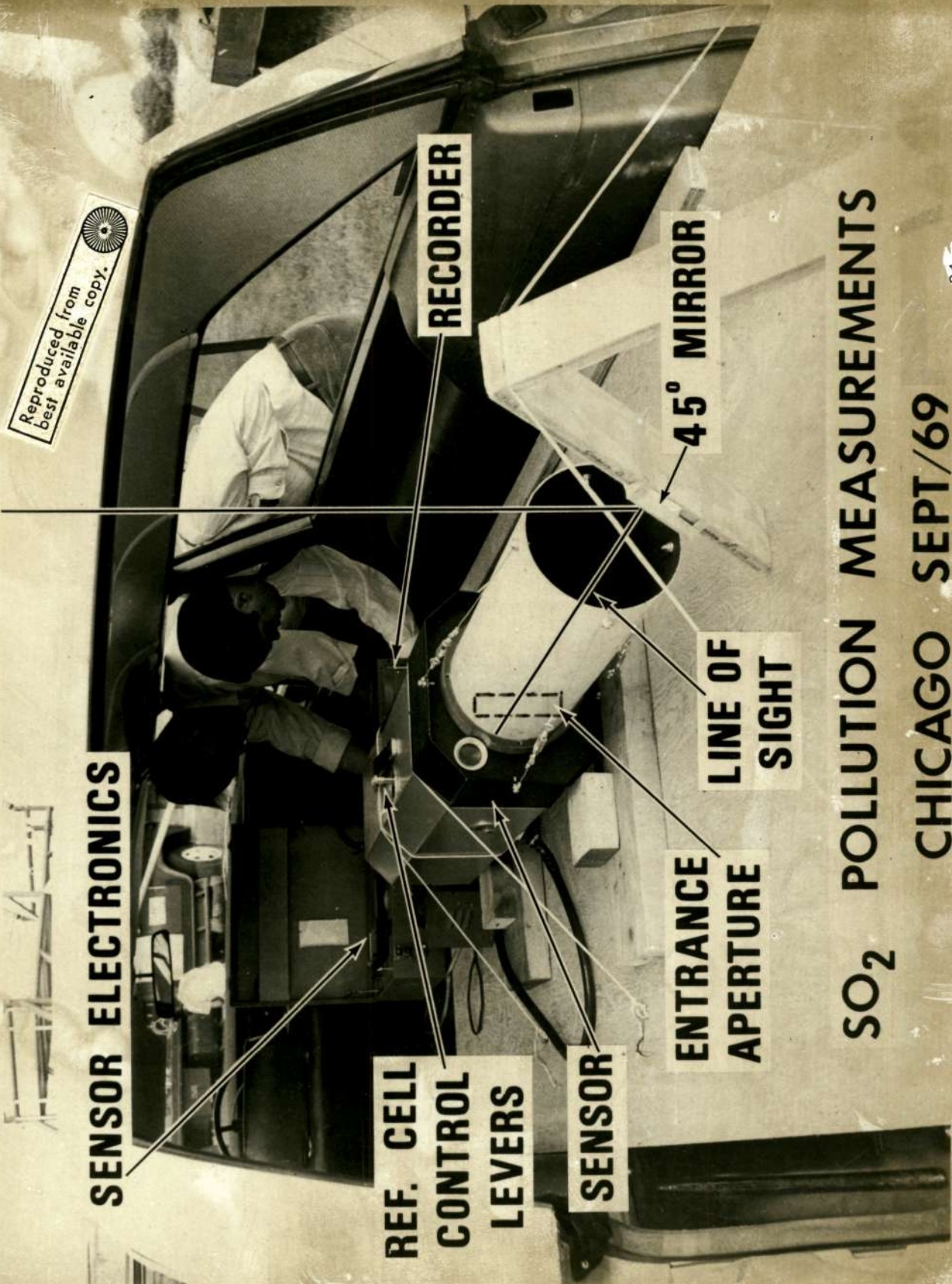
1215 CST      SEPT. 3rd. 1969

FIGURE 22



SO<sub>2</sub> VERTICAL PROFILE - GROUND TRAVERSE -  
CHICAGO

SEPT. 3rd 1969



Reproduced from  
best available copy.

**SENSOR ELECTRONICS**

**REF. CELL  
CONTROL  
LEVERS**

**SENSOR**

**ENTRANCE  
APERTURE**

**LINE OF  
SIGHT**

**45° MIRROR**

**RECORDER**

**SO<sub>2</sub> POLLUTION MEASUREMENTS  
CHICAGO SEPT/69**

101

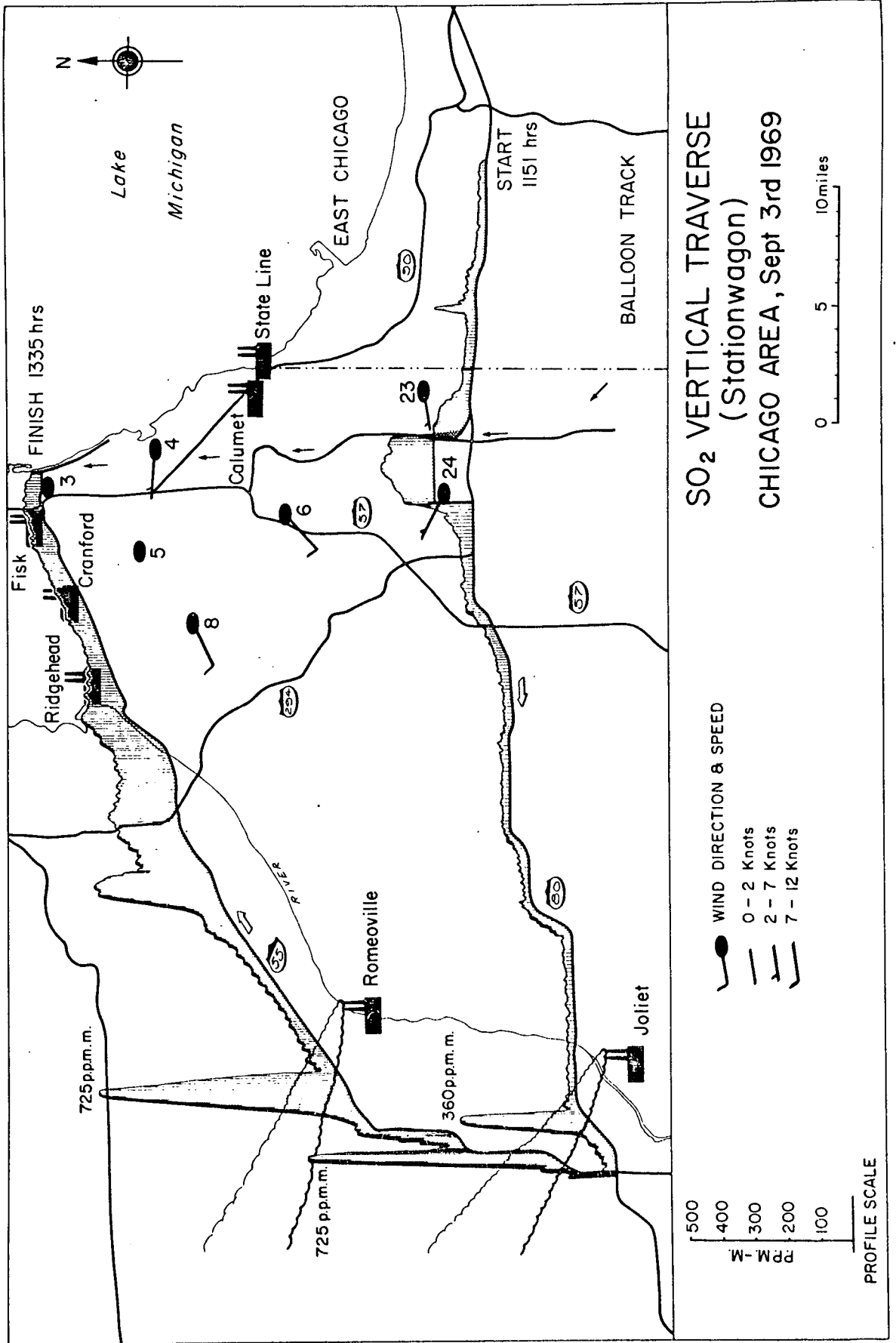


FIGURE 25

109



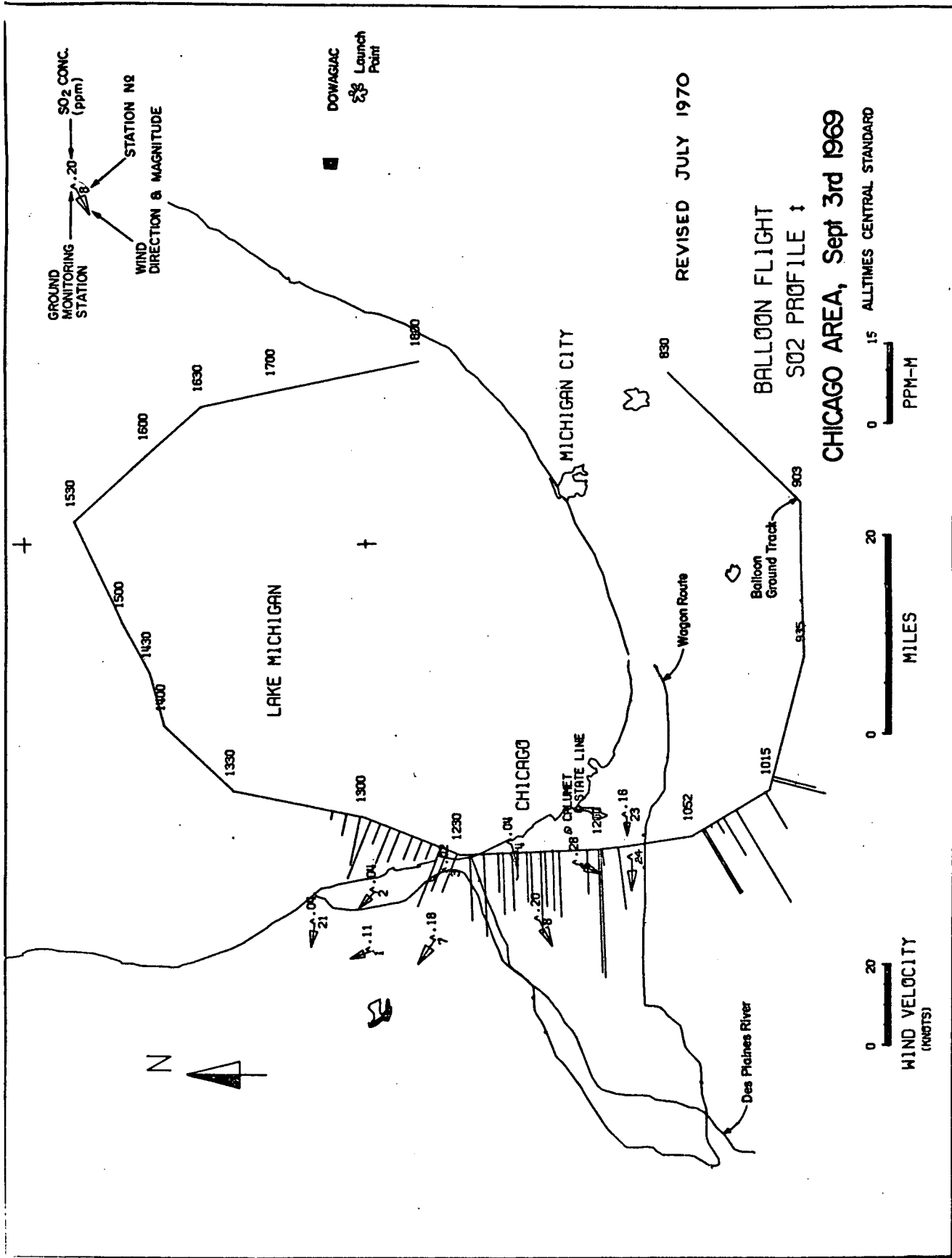


FIGURE 27

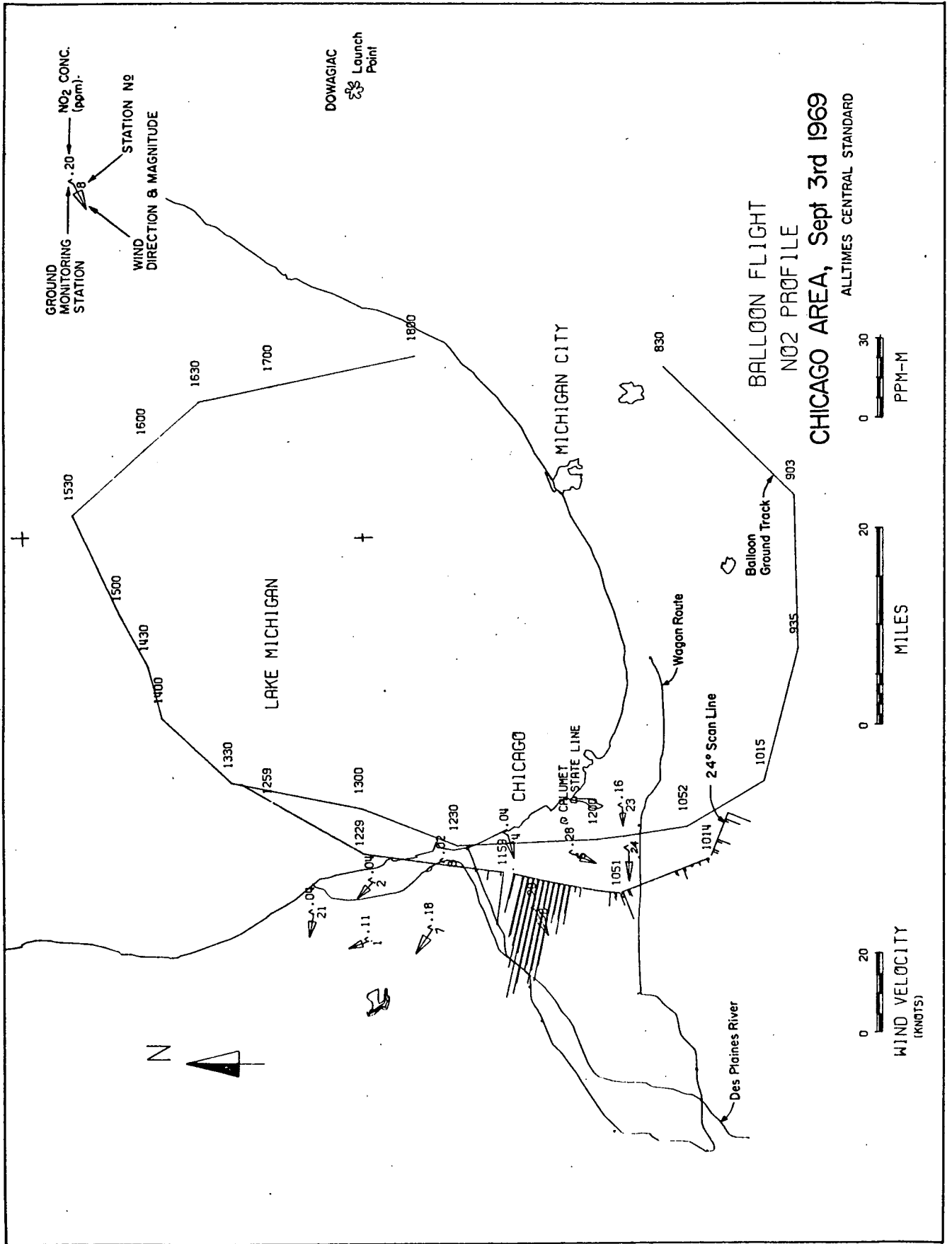


FIGURE 28

112

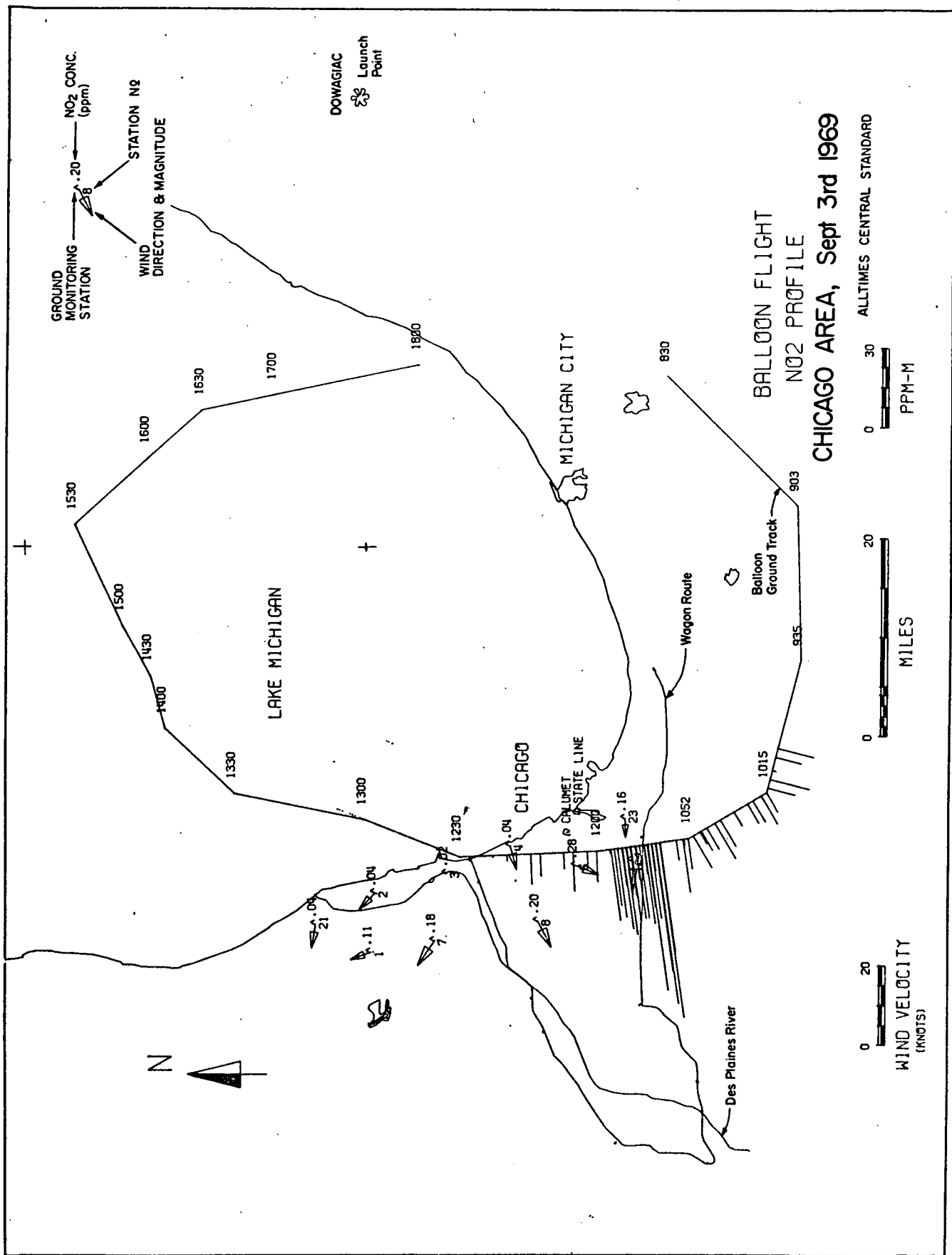


FIGURE 29

3-3

113

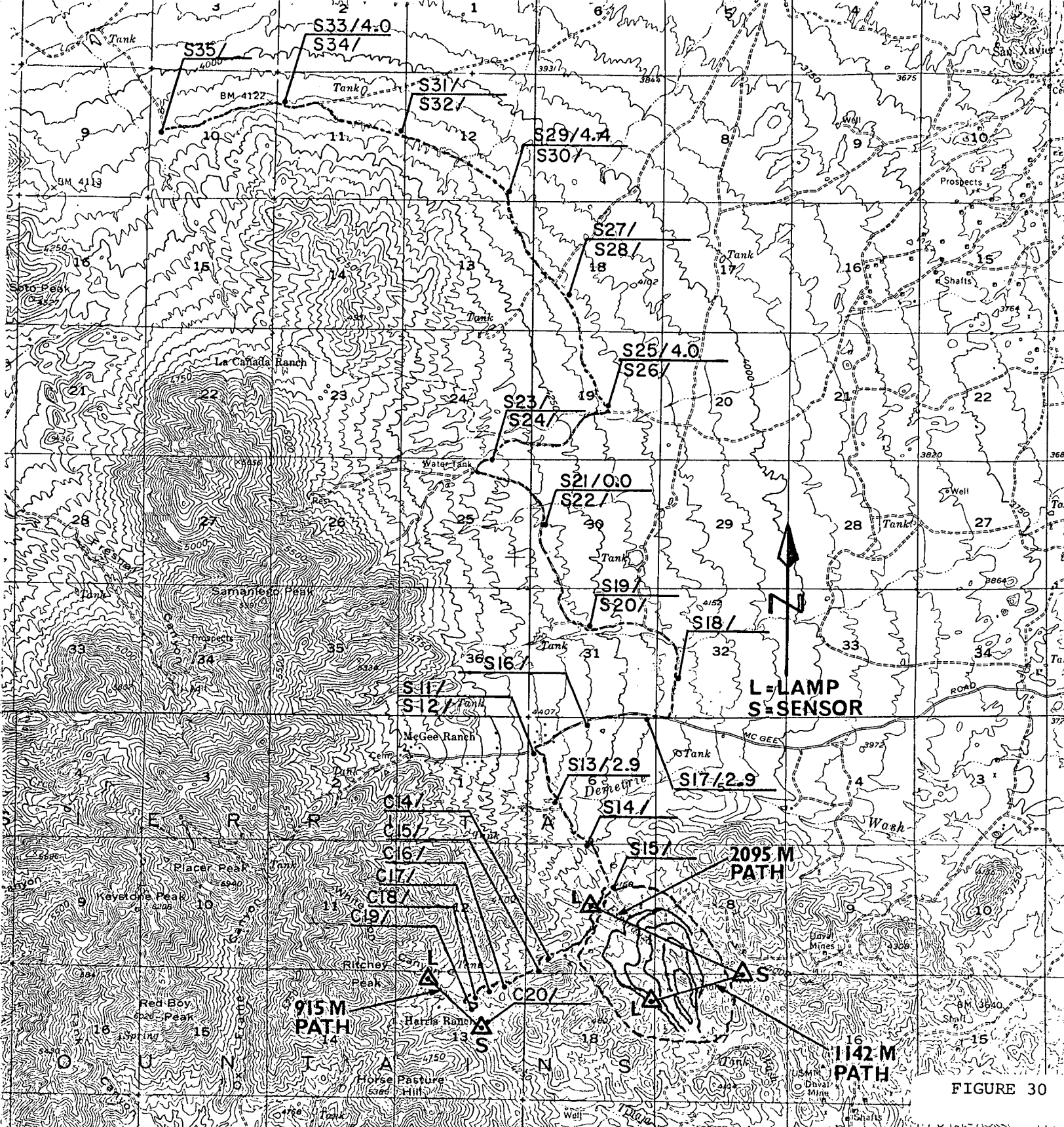


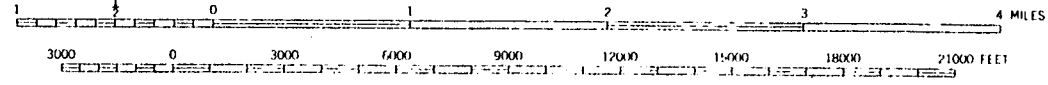
FIGURE 30

DUVAL SIERRITA PORPHYRY COPPER OPEN PIT  
 SHOWING SENSOR SITES &  
 ROCK AND SOIL SAMPLE LOCATIONS  
 TWIN BUTTES, ARIZONA. APRIL, 1970.



TWIN BUTTES, ARIZONA  
 N3145-W11100/15

SCALE 1:62500



CONTOUR INTERVAL 50 FEET  
 DATUM IS MEAN SEA LEVEL

Reproduced from  
best available copy.

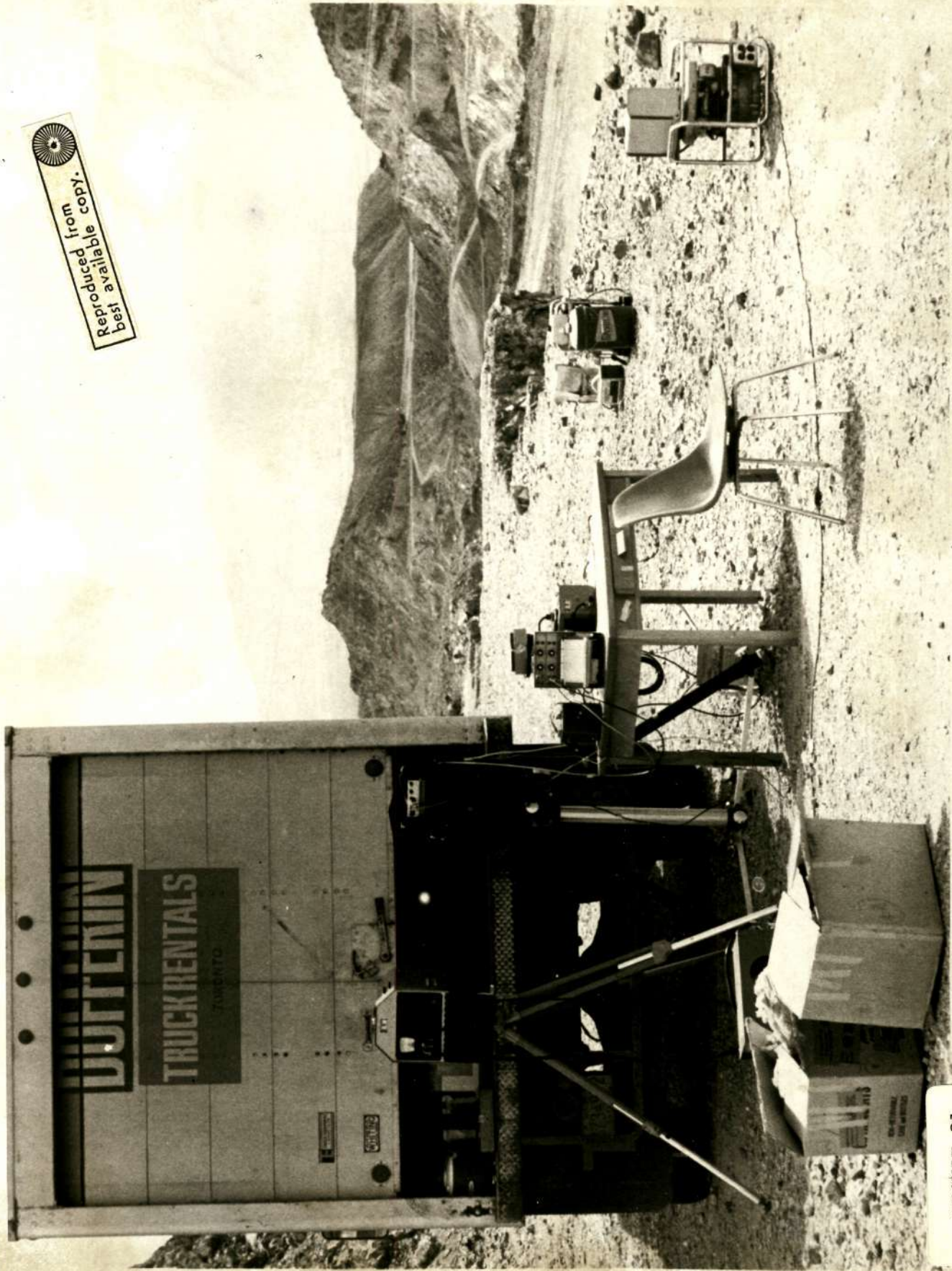


FIGURE 31 ZERO PATH LENGTH CALIBRATION. DUVAL SIERRITA. APRIL. 1970

113



Reproduced from  
best available copy.

SOURCE

WET CHEM SITE CA 3,4,5.

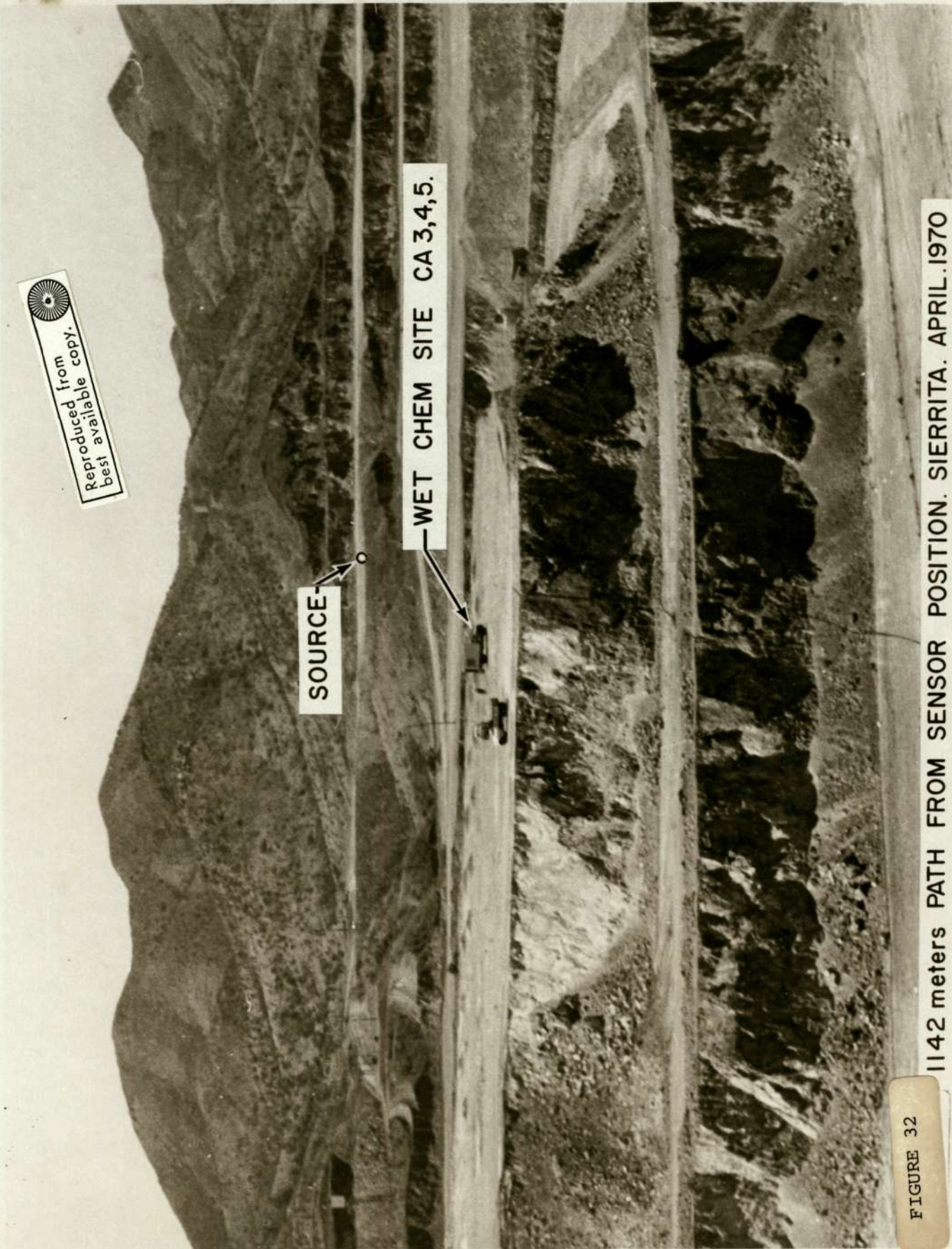
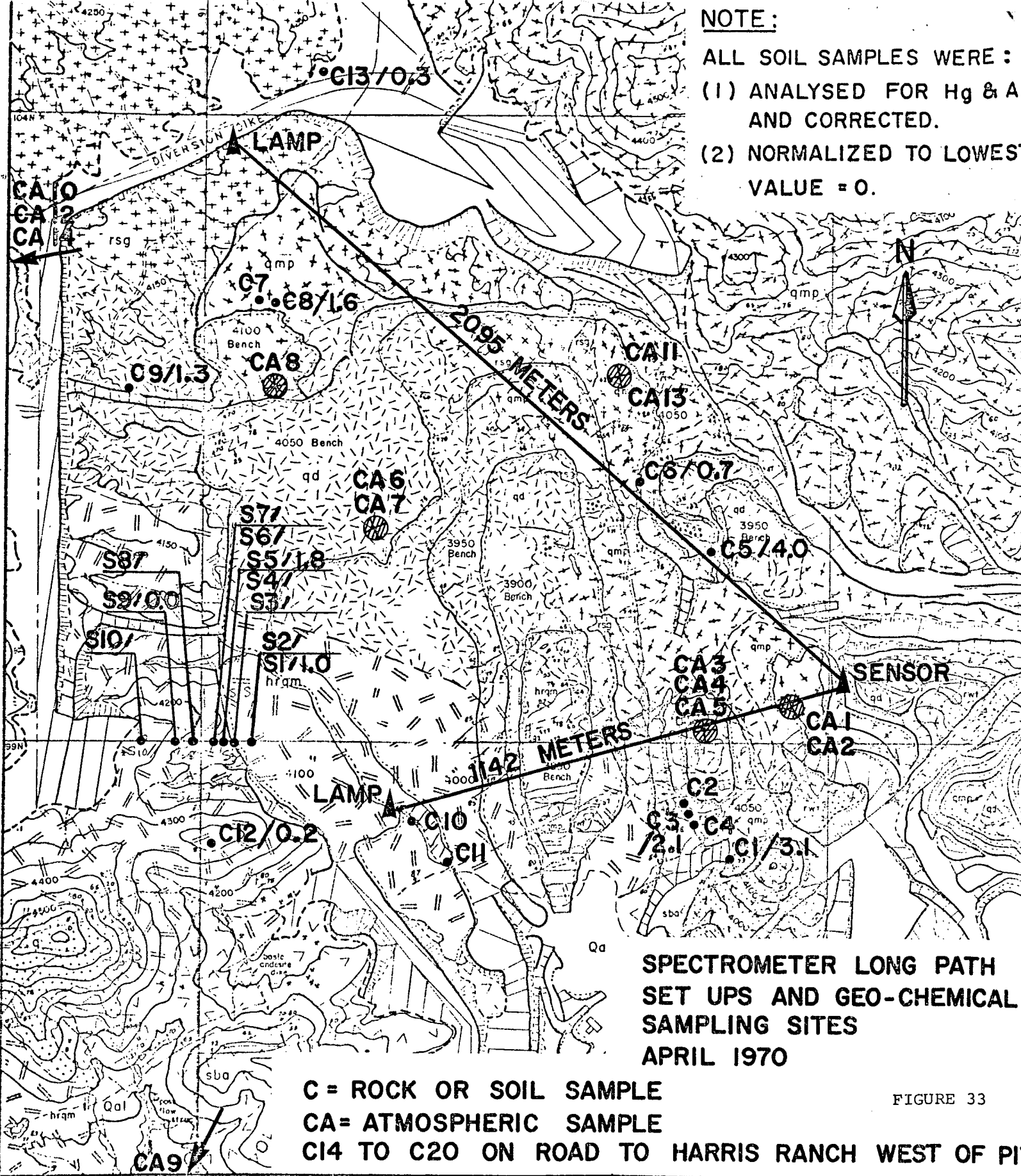


FIGURE 32

1142 meters PATH FROM SENSOR POSITION. SIERRITA. APRIL. 1970

**NOTE:**

- ALL SOIL SAMPLES WERE :
- (1) ANALYSED FOR Hg & Ag AND CORRECTED.
  - (2) NORMALIZED TO LOWEST VALUE = 0.



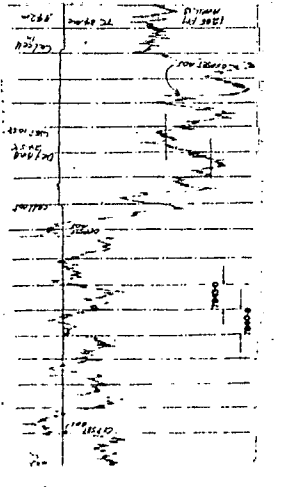
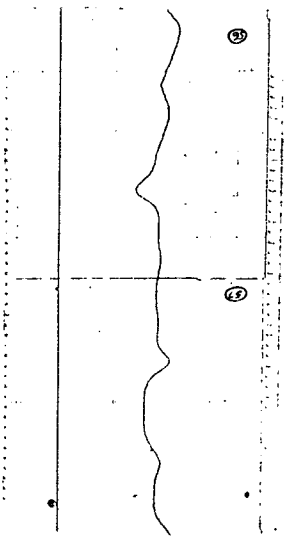
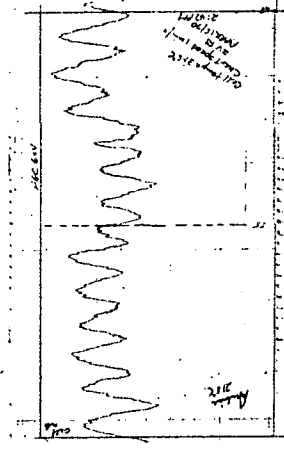
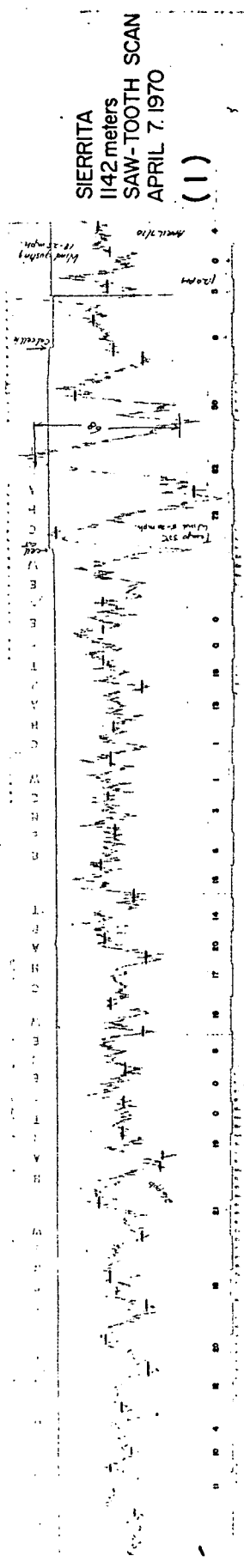
**SPECTROMETER LONG PATH SET UPS AND GEO-CHEMICAL SAMPLING SITES APRIL 1970**

**C = ROCK OR SOIL SAMPLE  
CA = ATMOSPHERIC SAMPLE  
C14 TO C20 ON ROAD TO HARRIS RANCH WEST OF PIUTE**

FIGURE 33

EXPLANATION	
Qal	Alluvium, waste dumps, Aplite
[Blank]	Massive quartz veins
qip	Quartz latite porphyry
qmp	Quartz monzonite porphyry
rsg	Ruby Star granodiorite
sba	Silver Bell (Demetrie) andesite
qd	Biotite quartz diorite
hrqm	Harris Ranch quartz monzonite
rwi	Oxframe rhyolite welded tuff
q	Quartzite

DUVAL SIERRITA CORPORATION	
SIERRITA PIT GEOLOGY	
SCALE: 1" = 1,000'	DATE: 3/2/70
GEOLOGY BY RAM, ANJ, BLW, DWL, FWM.	DRAWN BY R.D.G.



PORPHYRY COPPER RESULTS

118

# I<sub>2</sub> VAPOR PRESSURE vs TEMPERATURE

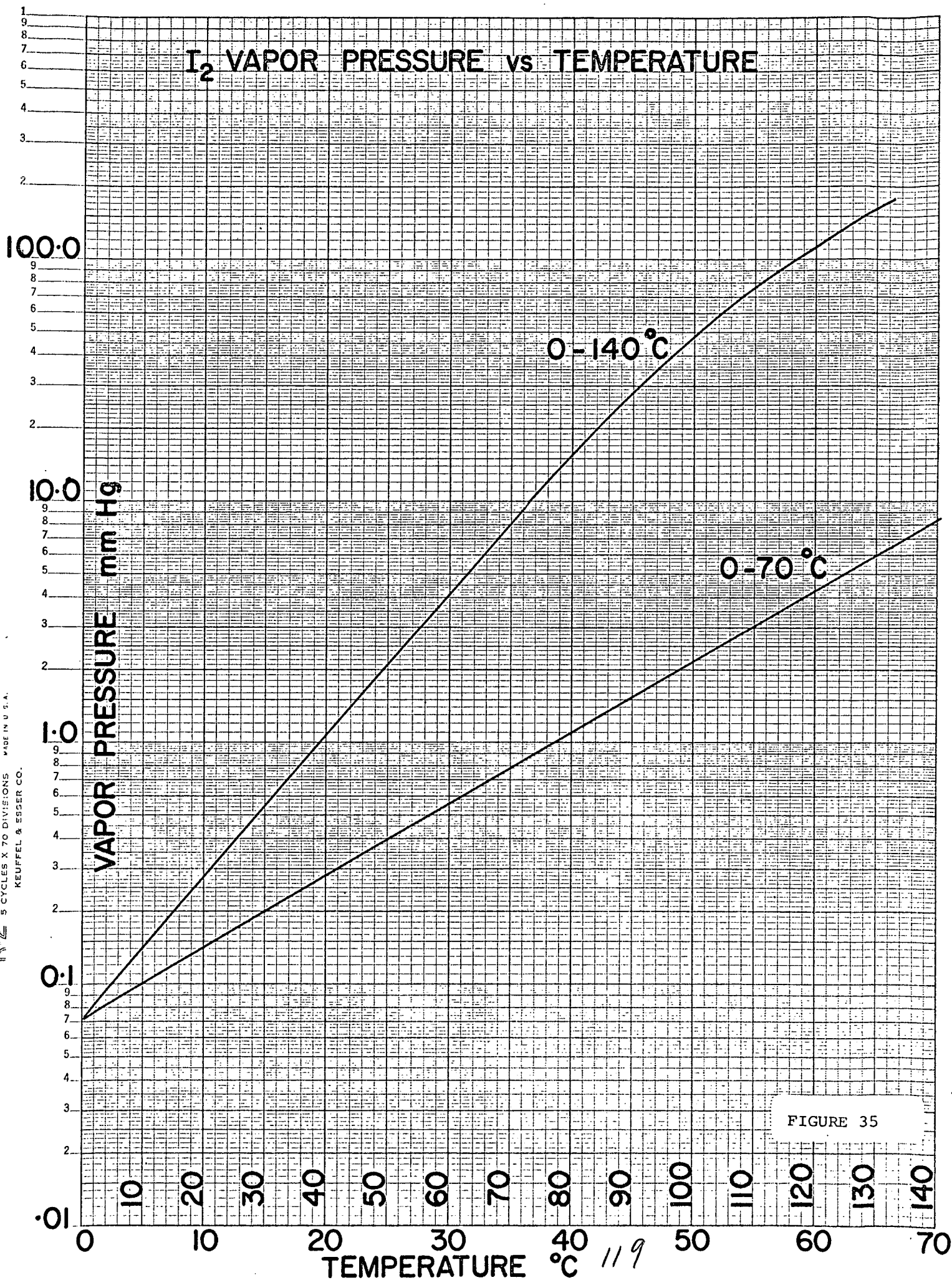
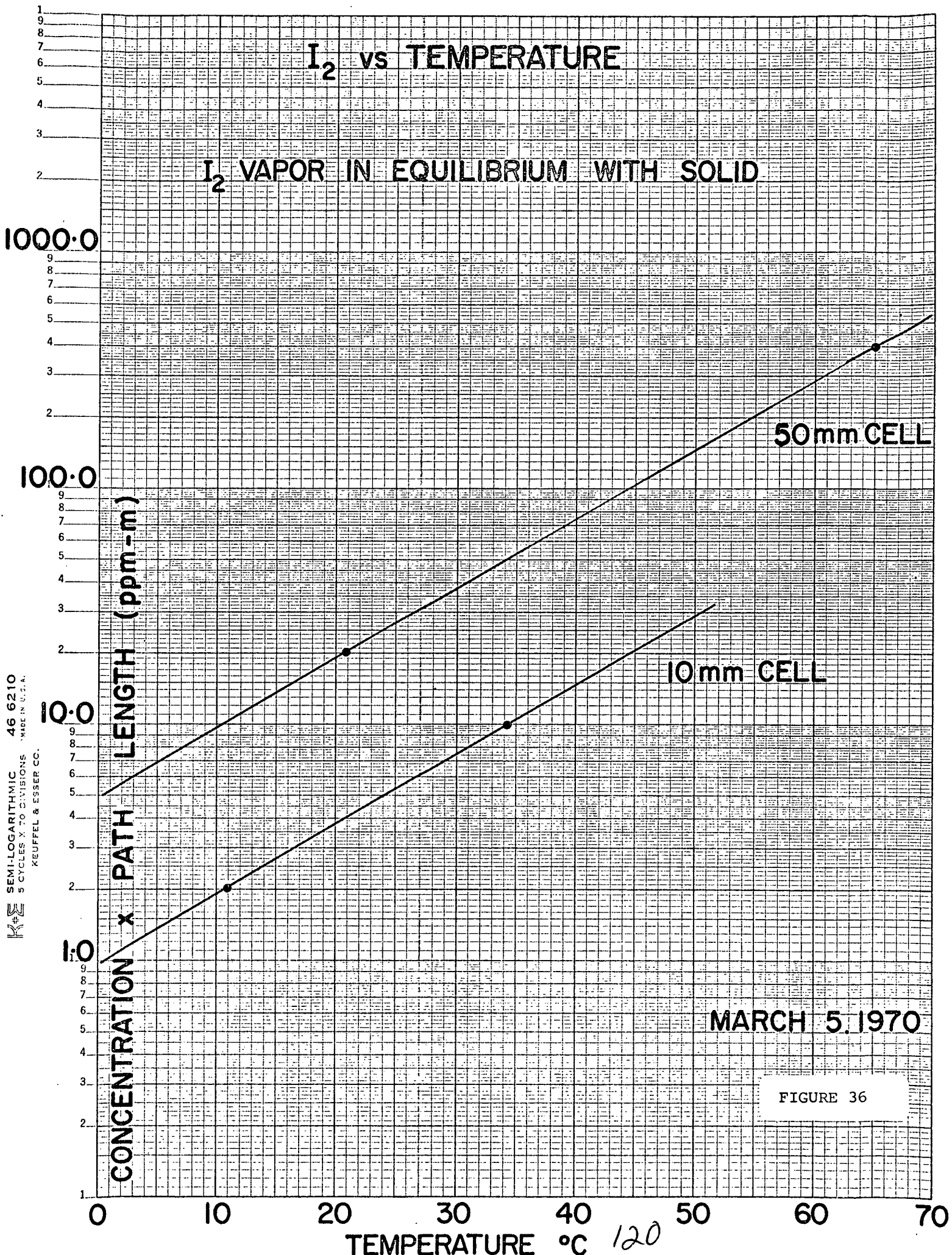


FIGURE 35

KE SEMI-LOGARITHMIC 46 6210  
5 CYCLES X 70 DIVISIONS MADE IN U.S.A.  
KEUFFEL & ESSER CO.



MARCH 5, 1970

FIGURE 36

120

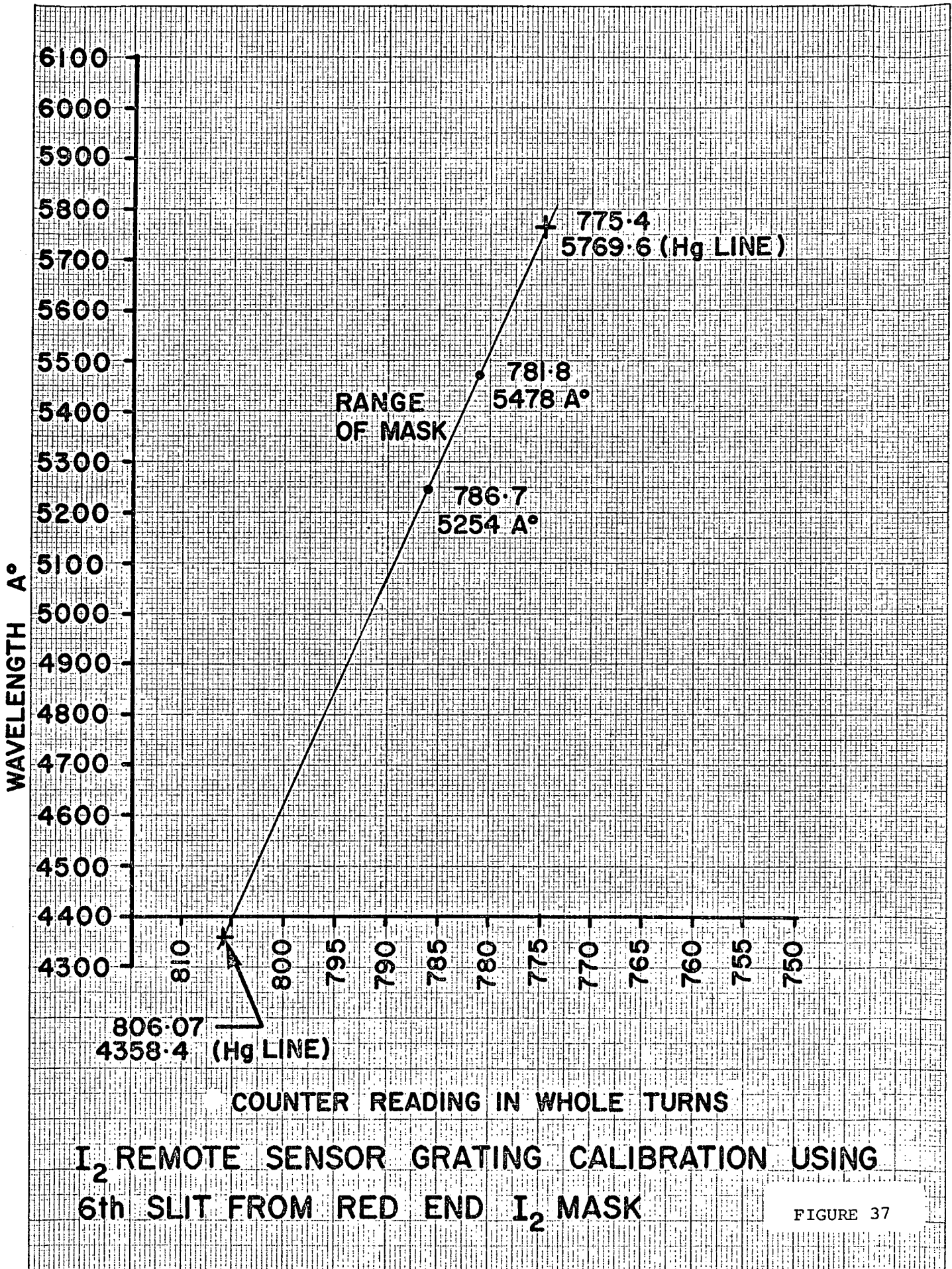
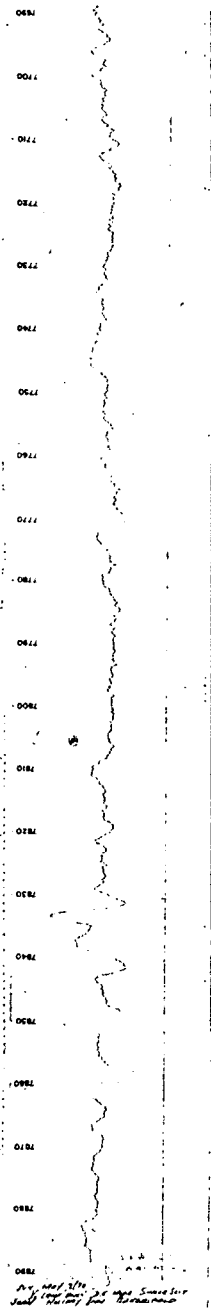


FIGURE 37

**GRATING POSITION**

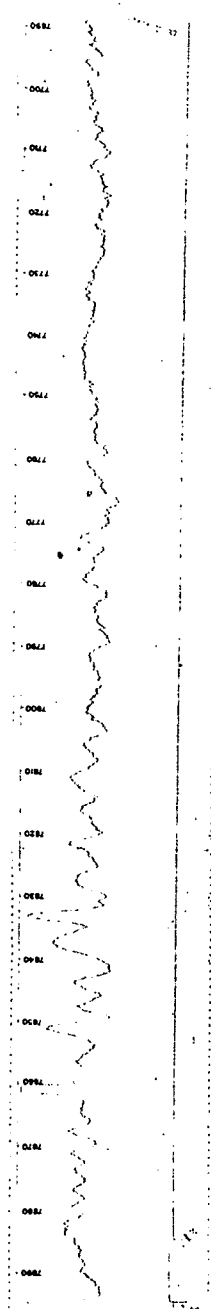
ZERO PATH LENGTH  
SINGLE SLIT SCAN  
Xe SOURCE ONLY  
MAY 3, 1970

(1)



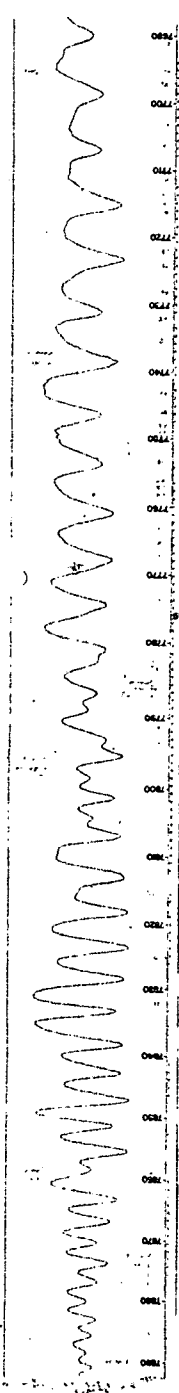
BROMINE CALIBRATION  
ZERO PATH LENGTH WITH Xe  
SINGLE SLIT SCAN 330ppm-m Br  
MAY 3, 1970

(2)



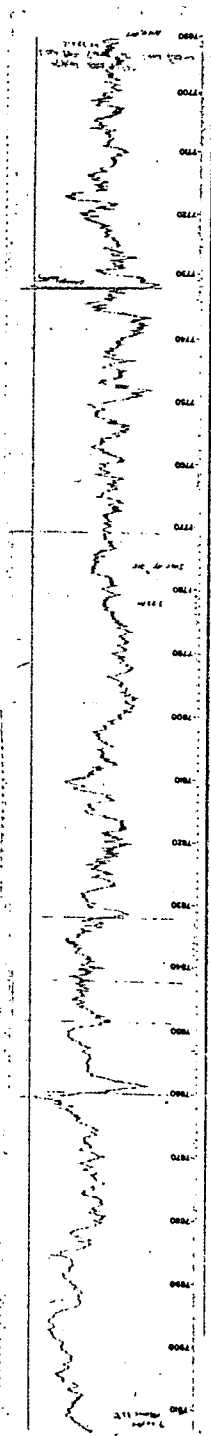
I<sub>1</sub> CALIBRATION  
ZERO PATH LENGTH WITH Xe  
SINGLE SLIT SCAN 56ppm-m I<sub>1</sub>  
APRIL 25, 1970

(3)



DUVAL SIERRITA OPEN PIT  
1142 METER PATH LENGTH  
SINGLE SLIT SCAN  
APRIL 23, 1970

(4)

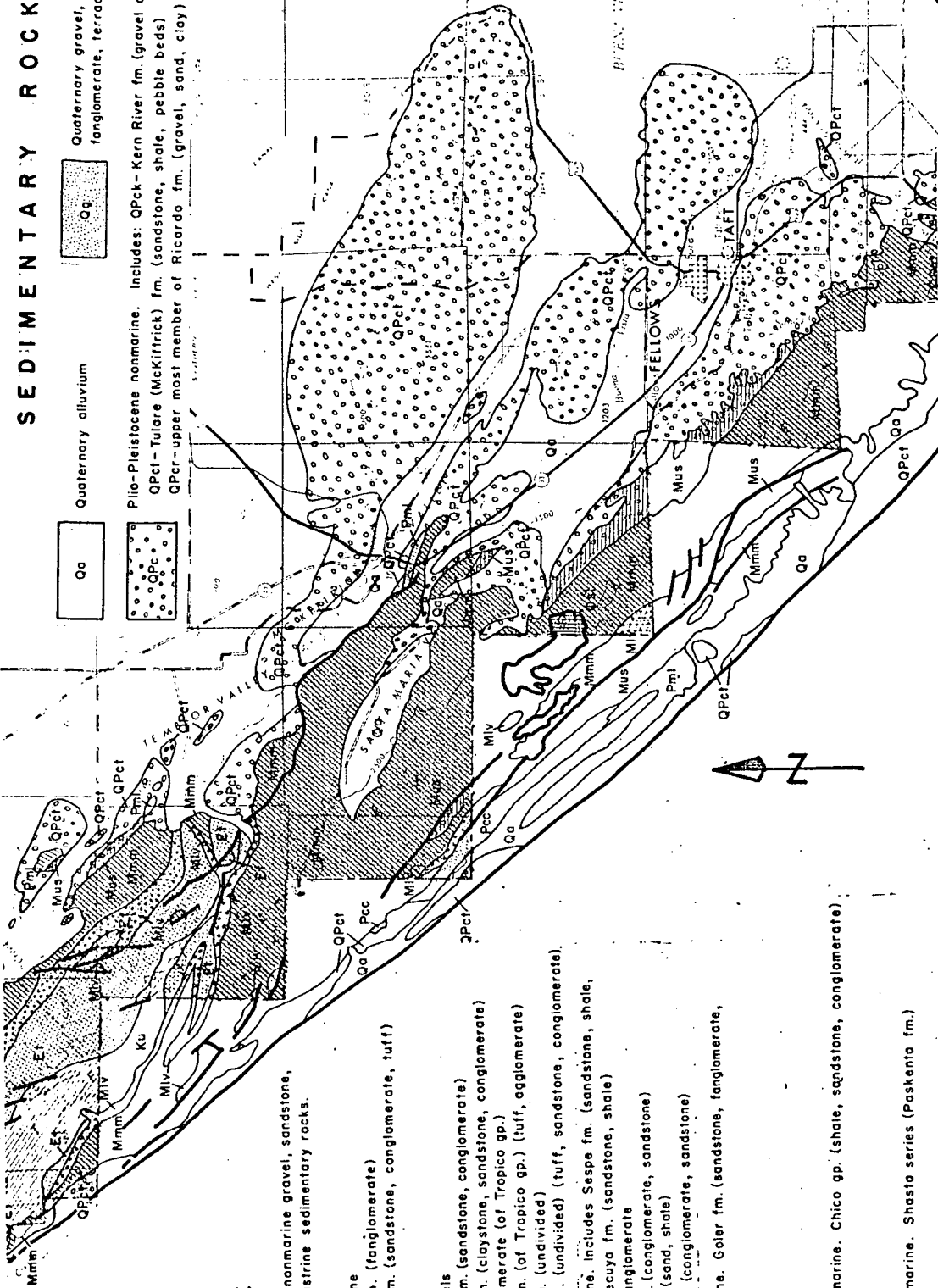


**SINGLE SLIT SCAN, SIERRITA.**



# SEDIMENTARY ROCKS

- Quaternary alluvium
- Quaternary gravel, sand, fanglomerate, terrace deposits
- Plio-Pleistocene nonmarine. Includes: QPct-Kern River fm. (gravel and sand) QPct-Tulare (McKfirick) fm. (sandstone, shale, pebble beds) QPcr-upper most member of Ricardo fm. (gravel, sand, clay)



## NON MARINE

- Tertiary undivided nonmarine gravel, sandstone, siltstone, and lacustrine sedimentary rocks.
- Pliocene nonmarine
  - Pcc-Chanac fm. (fanglomerate)
  - Pcr-Ricardo fm. (sandstone, conglomerate, tuff)
- Miocene nonmarine
  - Mcb-Bena gravels
  - Mcbp-Bopesta fm. (sandstone, conglomerate)
  - Mcc-Caliente fm. (claystone, sandstone, conglomerate)
  - Mcf-Fiss fanglomerate (of Tropic gp.)
  - Mcg-Gem Hill fm. (of Tropic gp.) (tuff, agglomerate)
  - Mck-Kinnick fm. (undivided)
  - Mct-Tropico gp. (undivided) (tuff, sandstone, conglomerate)
- Oligocene nonmarine. Includes Sespe fm. (sandstone, shale, conglomerate), Tecuya fm. (sandstone, shale)
- Qcb-Bealville fanglomerate
- Qcs-Simmier fm. (conglomerate, sandstone)
- Qcw-Walker fm. (sand, shale)
- Qcwt-Wiinet fm. (conglomerate, sandstone)
- Paleocene nonmarine. Galer fm. (sandstone, fanglomerate, clay)

## MARINE

- Upper Cretaceous marine. Chico gp. (shale, sandstone, conglomerate)
- Lower Cretaceous marine. Shasta series (Paskenta fm.)
- Pliocene marine. Includes
  - Pus-upper Pliocene San Joaquin fm. (clays)
  - Pml-middle and lower Pliocene Etchegoin fm. (sand, gravel)
- Upper Miocene marine
  - Mum-McClure shale
  - Mus-Santa Margarita sandstone and McDonald shale
- Middle Miocene marine. Includes Olcese sand, Round Mountain silt, Freeman silt, Jewett sand.
- Mmm-Maricopa shale
- Lower Miocene marine
  - Mlv-Lobos "Embudo" sandstone, Ferrero fm (silt, s. stone)

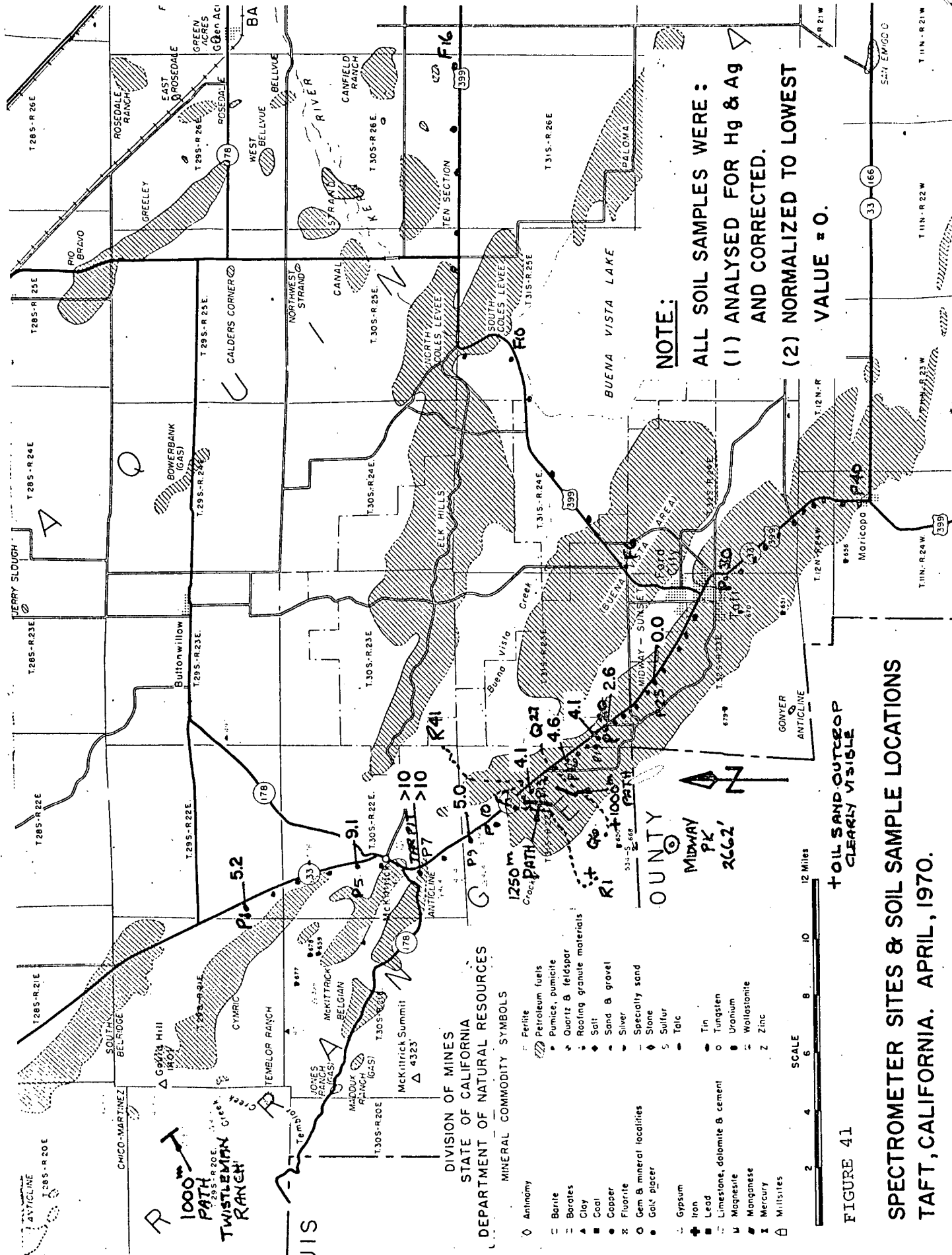
- Oligocene marine.
  - Osl-San Lorenzo fm. (Pleisto and San Emigdio membs.) (shale, sandstone)
  - Qw-Wagonwheel fm. (sandstone, diatomaceous shale)
- Eocene marine
  - Ej-Juncal shale
  - Emp-Pattway fm. (sandstone, shale)
  - Et-Tejon fm. (sandy shale, sandstone) (includes Kreyenhagen shale, Point/of Rocks sandstone)

GEOLOGIC MAP, KERN COUNTY, S.W. CORNER

FIGURE 40

SCALE





**NOTE:**

ALL SOIL SAMPLES WERE :  
 (1) ANALYSED FOR Hg & Ag  
 AND CORRECTED.  
 (2) NORMALIZED TO LOWEST  
 VALUE = 0.

DIVISION OF MINES  
 STATE OF CALIFORNIA  
 DEPARTMENT OF NATURAL RESOURCES  
 MINERAL COMMODITY SYMBOLS

- ◊ Anthracite
- ◻ Barite
- ◻ Borates
- ▲ Clay
- Coal
- Copper
- ⊗ Fluorite
- Gem & mineral localities
- Gink placer
- ⊥ Gypsum
- ⊕ Iron
- ⊖ Lead
- ◻ Limestone, dolomite & cement
- ⊥ Magnesite
- ⊥ Manganese
- ⊥ Mercury
- ⊥ Millsties
- ◻ Ferrite
- ◻ Petroleum fuels
- ◻ Pumice, pumicite
- ◻ Quartz & feldspar
- ◻ Roofing granite materials
- ◻ Salt
- ◻ Sand & gravel
- ◻ Silver
- ◻ Specially sand
- ◻ Stone
- ◻ Sulfur
- ◻ Talc
- ◻ Tin
- ◻ Tungsten
- ◻ Uranium
- ◻ Wollastonite
- ◻ Zinc

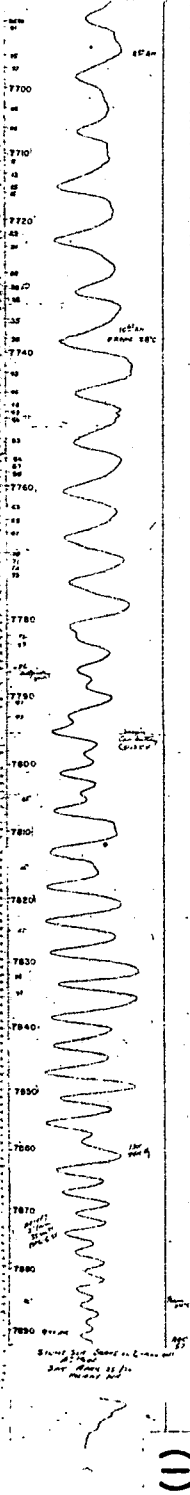
SCALE 2 4 6 8 10 12 Miles

FIGURE 41

SPECTROMETER SITES & SOIL SAMPLE LOCATIONS  
 TAFT, CALIFORNIA. APRIL, 1970.

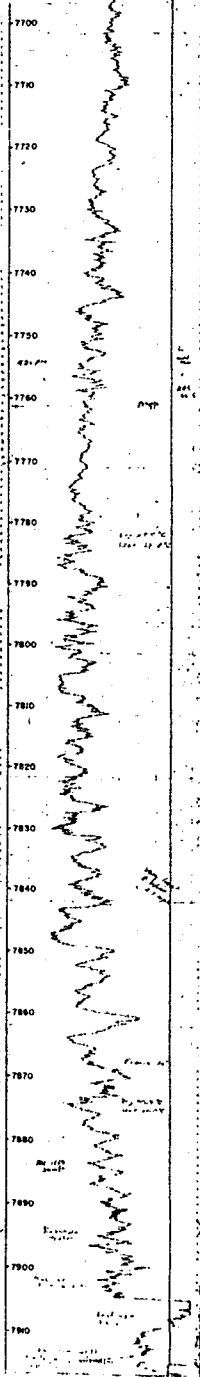
GRATING POSITION

I<sub>1</sub> CALIBRATION  
 ZERO PATH LENGTH WITH Xe  
 SINGLE SLIT SCAN 56ppm-m I<sub>1</sub>  
 APRIL 25, 1970



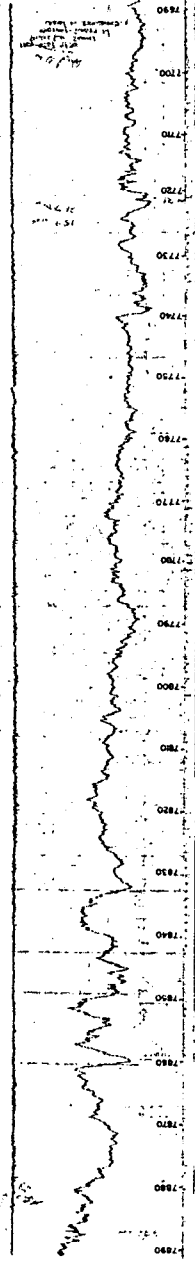
(1)

1000 METERS  
 TWISTLEMAN RANCH BACKGROUND  
 TRACE OF I<sub>1</sub> IN REF CELL  
 MAY 2, 1970



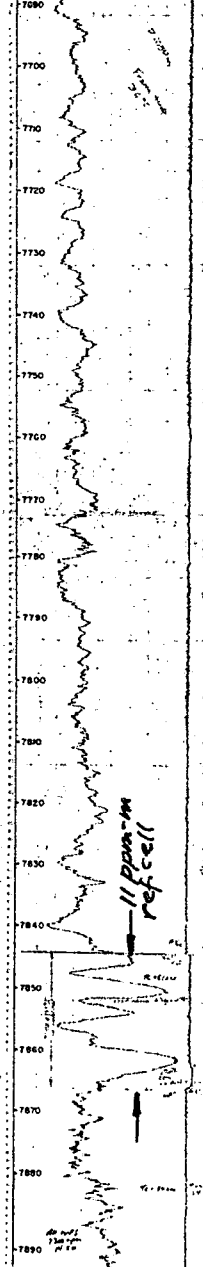
(2)

1000 METER SINGLE SLIT SCAN  
 MIDWAY-SUNSET NORTH  
 MAY 4, 1970  
 SCAN No. 1



(3)

1000 METERS SINGLE SLIT SCAN  
 MIDWAY-SUNSET NORTH  
 MAY 4, 1970  
 SCAN No. 2



(4)

SINGLE SLIT SCAN OIL FIELD

SAMP SITE	TTL I <sub>1</sub>	SAMP SITE	TTL I <sub>2</sub>
R 20		R 40	2.1
R 19	4.5	R 39	1.0
R 18		R 38	
R 17	4.9	R 37	2.9
R 16		R 36	
R 15		R 35	1.0
R 14		R 34	
R 13	2.6	R 33	1.0
R 12		R 32	
R 11		R 31	1.0
R 10		R 30	
R 9	5.6	R 29	
R 8		R 28	
R 7		R 27	1.0
R 6		R 26	
R 5	0.6	R 25	
R 4		R 24	
R 3		R 23	0.6
R 2		R 22	
R 1	1.4	R 21	

SAMP SITE	TTL I <sub>1</sub>	SAMP SITE	TTL I <sub>2</sub>
Q 15			
Q 14			
Q 13			
Q 12		Q 27	
Q 11		Q 26	
Q 10		Q 25	
Q 9		Q 24	
Q 8		Q 23	
Q 7		Q 22	
Q 6		Q 21	
Q 5		Q 20	
Q 4		Q 19	
Q 3		Q 18	
Q 2		Q 17	
Q 1		Q 16	

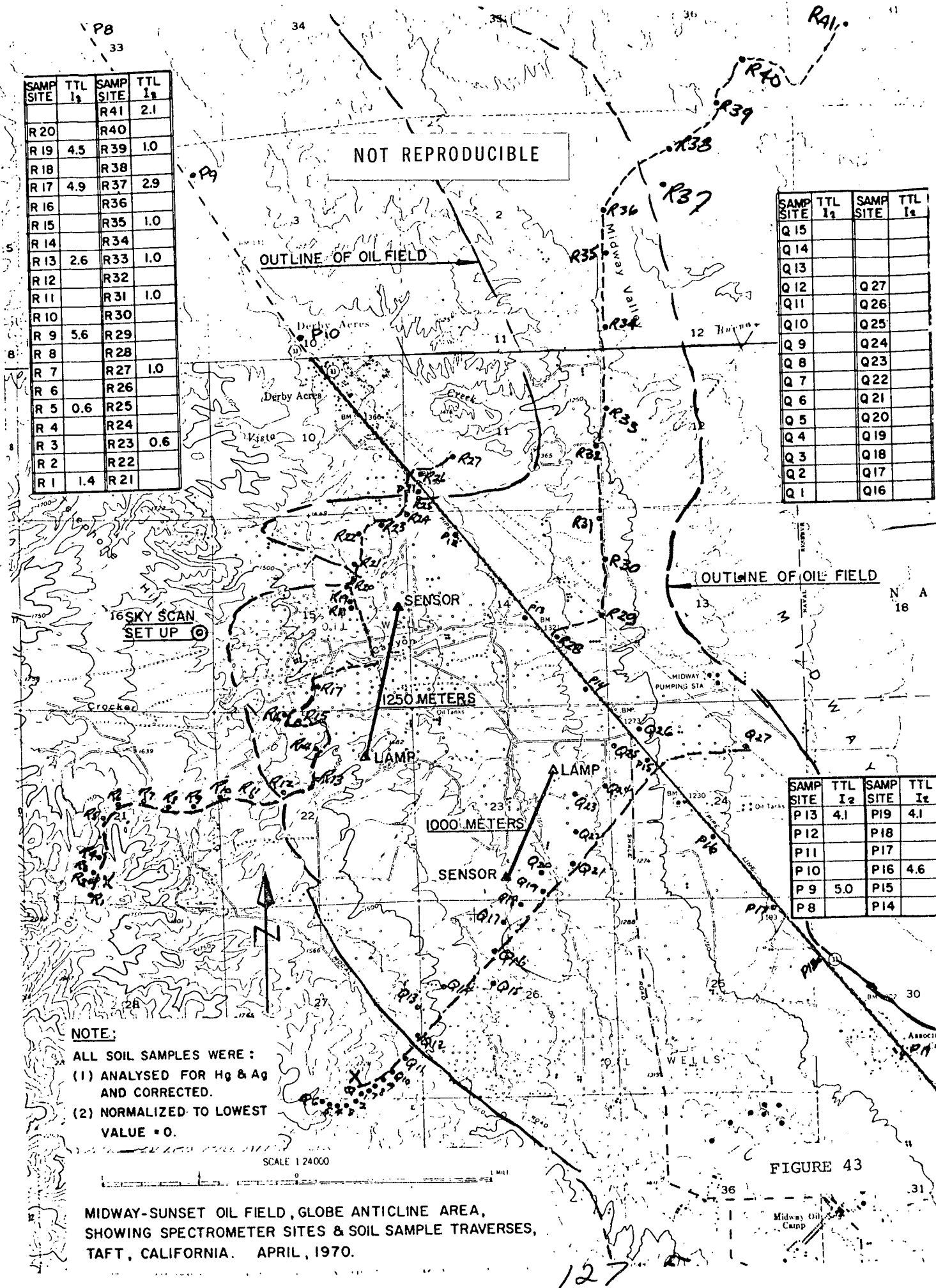
SAMP SITE	TTL I <sub>2</sub>	SAMP SITE	TTL I <sub>2</sub>
P 13	4.1	P 19	4.1
P 12		P 18	
P 11		P 17	
P 10		P 16	4.6
P 9	5.0	P 15	
P 8		P 14	

**NOTE:**  
 ALL SOIL SAMPLES WERE :  
 (1) ANALYSED FOR Hg & Ag AND CORRECTED.  
 (2) NORMALIZED TO LOWEST VALUE = 0.

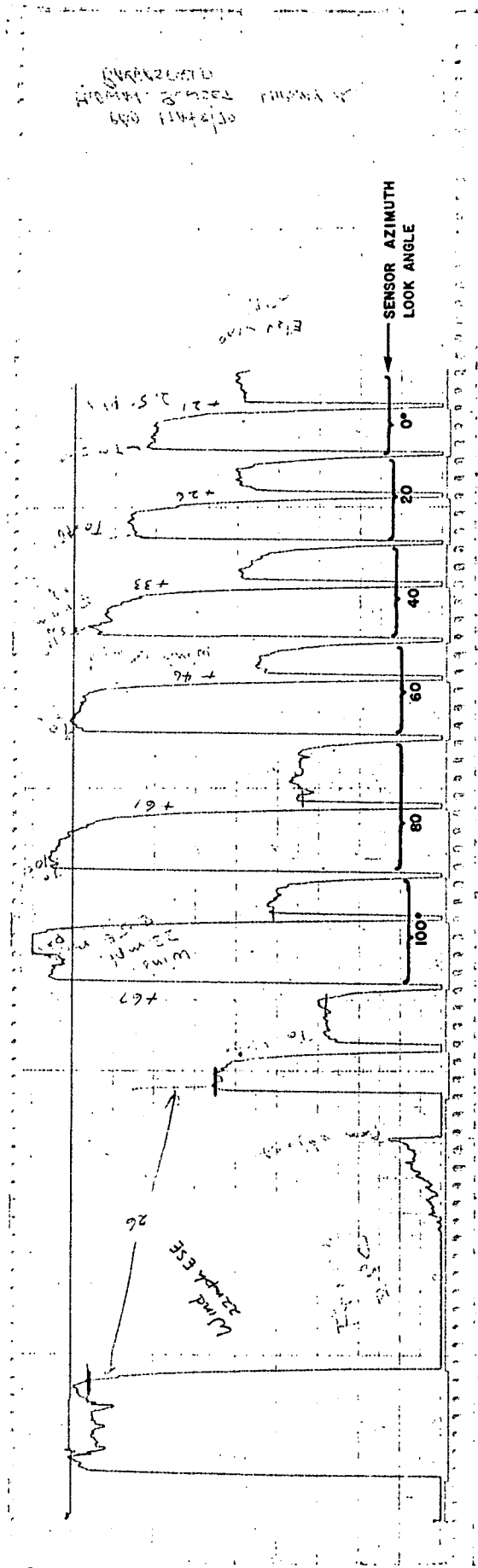
SCALE 1:24000

MIDWAY-SUNSET OIL FIELD, GLOBE ANTICLINE AREA, SHOWING SPECTROMETER SITES & SOIL SAMPLE TRAVERSES, TAFT, CALIFORNIA. APRIL, 1970.

FIGURE 43

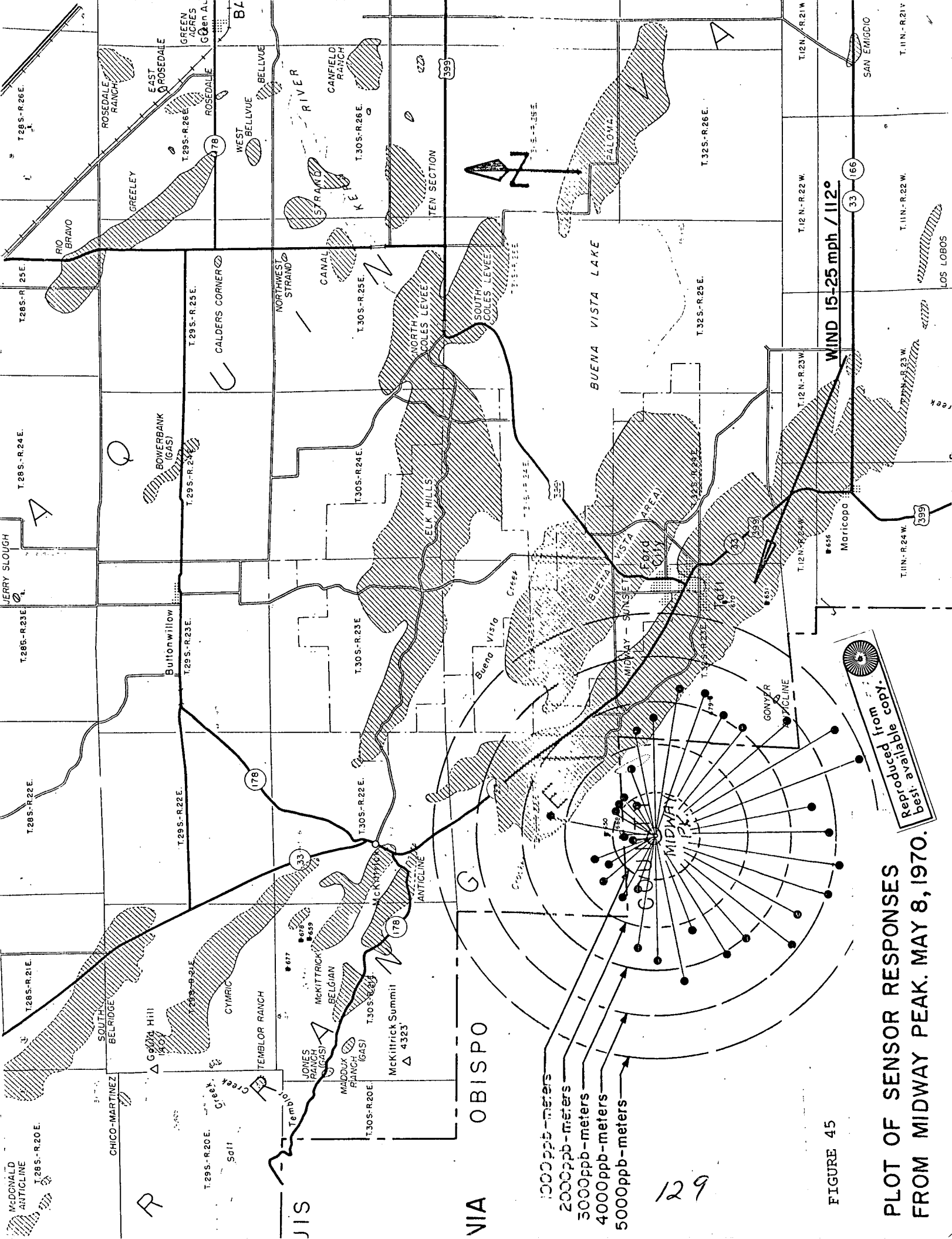


127



SQ. WAVE SCANS IN PASSIVE MODE  
 FOR DISCRETE AZIMUTH ANGLES  
 AND 10° DEPRESSIONS.  
 MIDWAY PEAK. MAY 8.1970

  
 Reproduced from  
 best available copy.



McDONALD ANTICLINE  
T.285.-R.20E.

T.285.-R.21E.

T.285.-R.22E.

T.285.-R.23E.

T.285.-R.24E.

T.285.-R.25E.

T.285.-R.26E.

T.285.-R.26E.

CHICO-MARTINEZ

SOUTH BELBRIDGE

GODDARD HILL

Buttón willow

BOVERBANK (GAS)

CALDERS CORNER

WEST BELLVUE

ROSEDALE RANCH

T.295.-R.20E.

T.295.-R.21E.

T.295.-R.22E.

T.295.-R.23E.

T.295.-R.24E.

T.295.-R.25E.

T.295.-R.26E.

T.295.-R.26E.

Temblor Creek

Temblor Ranch

JONES RANCH (GAS)

McKITTRICK RANCH (GAS)

McKITTRICK BELGIAN

McKITTRICK SUMMIT

McKITTRICK BELGIAN

McKITTRICK BELGIAN

T.305.-R.20E.

T.305.-R.21E.

T.305.-R.22E.

T.305.-R.23E.

T.305.-R.24E.

T.305.-R.25E.

T.305.-R.26E.

T.305.-R.26E.

McKITTRICK SUMMIT

McKITTRICK BELGIAN

T.315.-R.20E.

T.315.-R.21E.

T.315.-R.22E.

T.315.-R.23E.

T.315.-R.24E.

T.315.-R.25E.

T.315.-R.26E.

T.315.-R.26E.

McKITTRICK BELGIAN

T.325.-R.20E.

T.325.-R.21E.

T.325.-R.22E.

T.325.-R.23E.

T.325.-R.24E.

T.325.-R.25E.

T.325.-R.26E.

T.325.-R.26E.

McKITTRICK BELGIAN

T.335.-R.20E.

T.335.-R.21E.

T.335.-R.22E.

T.335.-R.23E.

T.335.-R.24E.

T.335.-R.25E.

T.335.-R.26E.

T.335.-R.26E.

McKITTRICK BELGIAN

T.345.-R.20E.

T.345.-R.21E.

T.345.-R.22E.

T.345.-R.23E.

T.345.-R.24E.

T.345.-R.25E.

T.345.-R.26E.

T.345.-R.26E.

McKITTRICK BELGIAN

T.355.-R.20E.

T.355.-R.21E.

T.355.-R.22E.

T.355.-R.23E.

T.355.-R.24E.

T.355.-R.25E.

T.355.-R.26E.

T.355.-R.26E.

McKITTRICK BELGIAN

T.365.-R.20E.

T.365.-R.21E.

T.365.-R.22E.

T.365.-R.23E.

T.365.-R.24E.

T.365.-R.25E.

T.365.-R.26E.

T.365.-R.26E.

McKITTRICK BELGIAN

T.375.-R.20E.

T.375.-R.21E.

T.375.-R.22E.

T.375.-R.23E.

T.375.-R.24E.

T.375.-R.25E.

T.375.-R.26E.

T.375.-R.26E.

McKITTRICK BELGIAN

T.385.-R.20E.

T.385.-R.21E.

T.385.-R.22E.

T.385.-R.23E.

T.385.-R.24E.

T.385.-R.25E.

T.385.-R.26E.

T.385.-R.26E.

McKITTRICK BELGIAN

T.395.-R.20E.

T.395.-R.21E.

T.395.-R.22E.

T.395.-R.23E.

T.395.-R.24E.

T.395.-R.25E.

T.395.-R.26E.

T.395.-R.26E.

McKITTRICK BELGIAN

T.405.-R.20E.

T.405.-R.21E.

T.405.-R.22E.

T.405.-R.23E.

T.405.-R.24E.

T.405.-R.25E.

T.405.-R.26E.

T.405.-R.26E.

McKITTRICK BELGIAN

T.415.-R.20E.

T.415.-R.21E.

T.415.-R.22E.

T.415.-R.23E.

T.415.-R.24E.

T.415.-R.25E.

T.415.-R.26E.

T.415.-R.26E.

McKITTRICK BELGIAN

T.425.-R.20E.

T.425.-R.21E.

T.425.-R.22E.

T.425.-R.23E.

T.425.-R.24E.

T.425.-R.25E.

T.425.-R.26E.

T.425.-R.26E.

McKITTRICK BELGIAN

Reproduced from copy. best available copy.

FIGURE 45

PLOT OF SENSOR RESPONSES FROM MIDWAY PEAK. MAY 8, 1970.

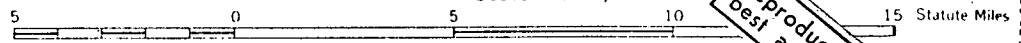
- 1000 ppb-meters
- 2000 ppb-meters
- 3000 ppb-meters
- 4000 ppb-meters
- 5000 ppb-meters

129



SAMP SITE	1	2	3	4	5	6	7	8	9	10
I <sub>2</sub>	>10		2.0		1.8		5.0		4.0	
SAMP SITE	11	12	13	14	15	16	17	18		
I <sub>2</sub>			0.0			2.8	2.6	4.1		

Scale 1:250,000



**SENSOR SITE & SOIL SAMPLE LOCATIONS  
STEAM FIELD, GEYSERVILLE, CALIFORNIA.**

Reproduced from  
best available copy.

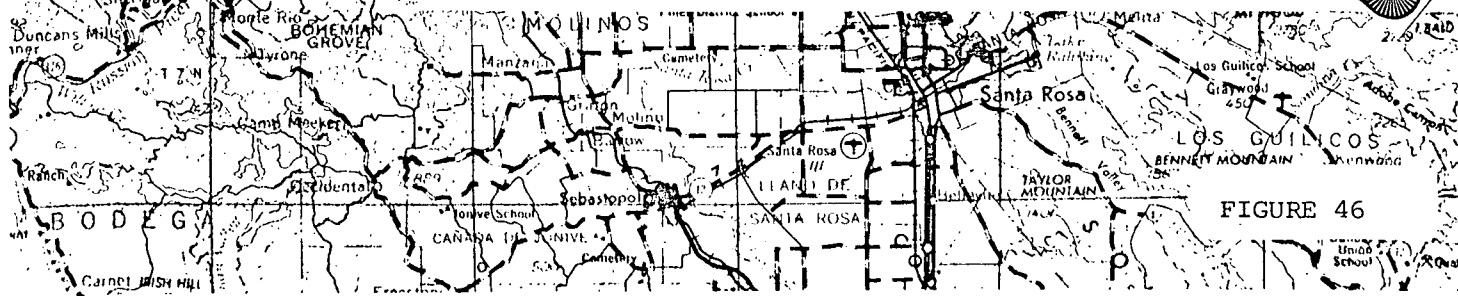


FIGURE 46

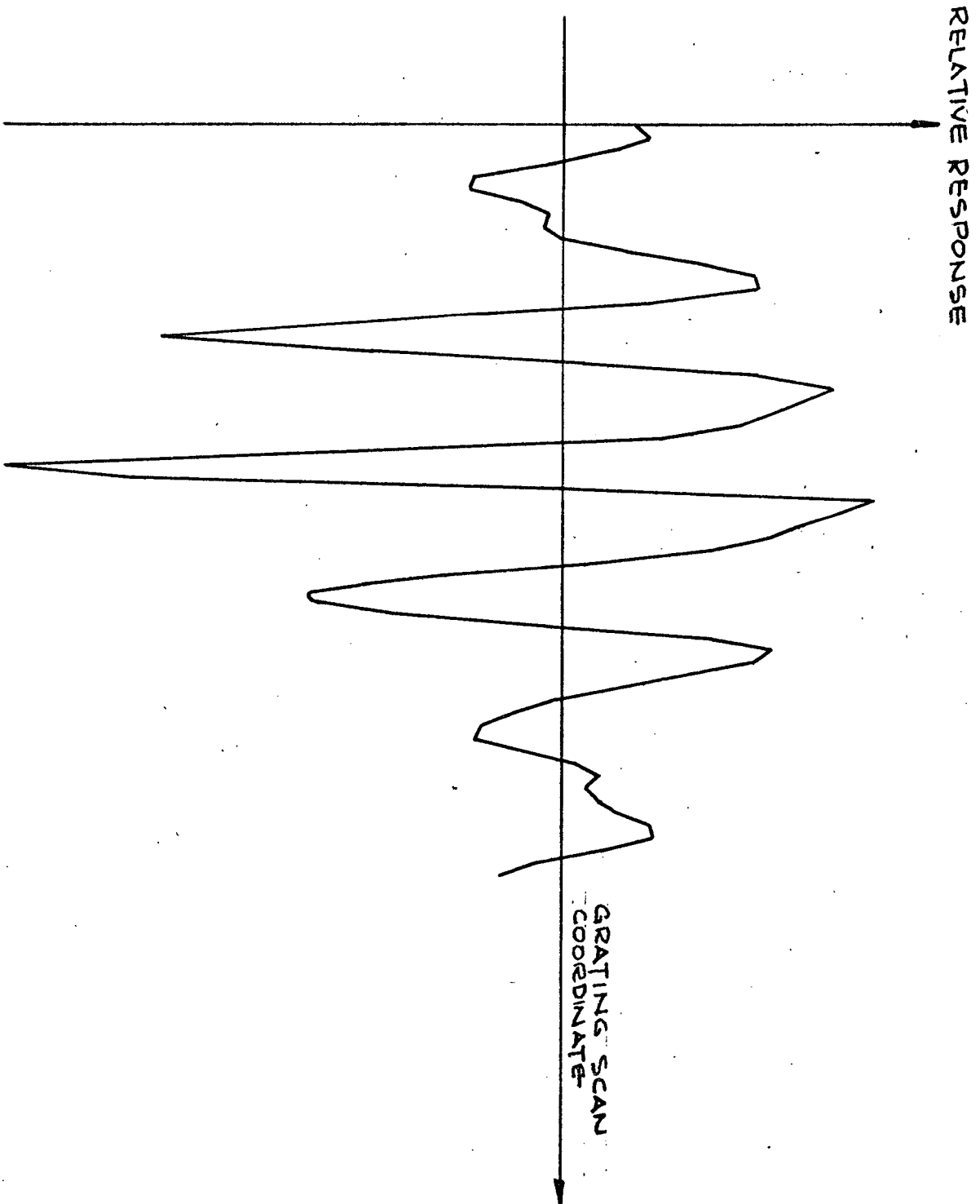


FIGURE 47

Theoretical response of a 12 Slit  $I_2$  Mask to 5 ppm-m of  $I_2$

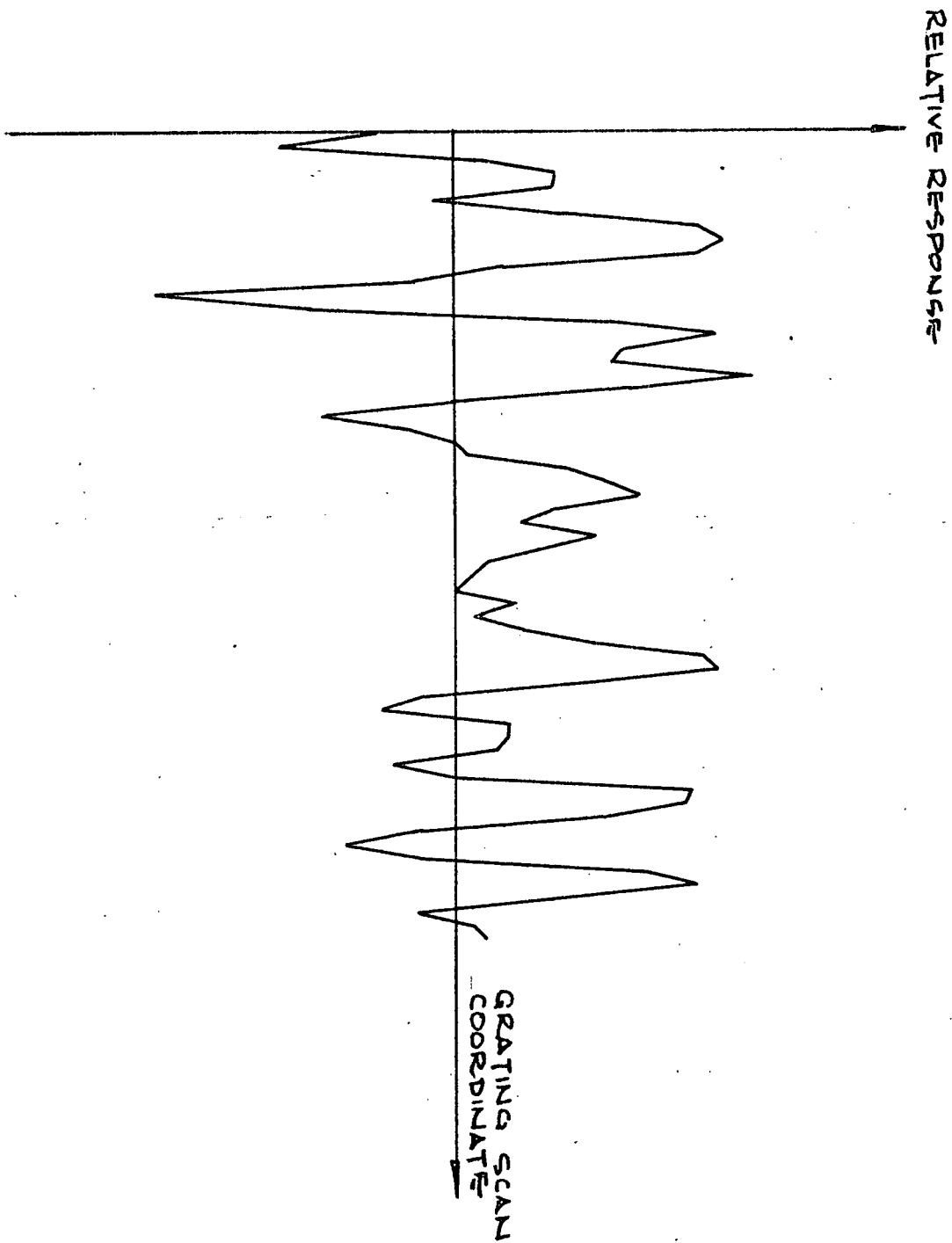
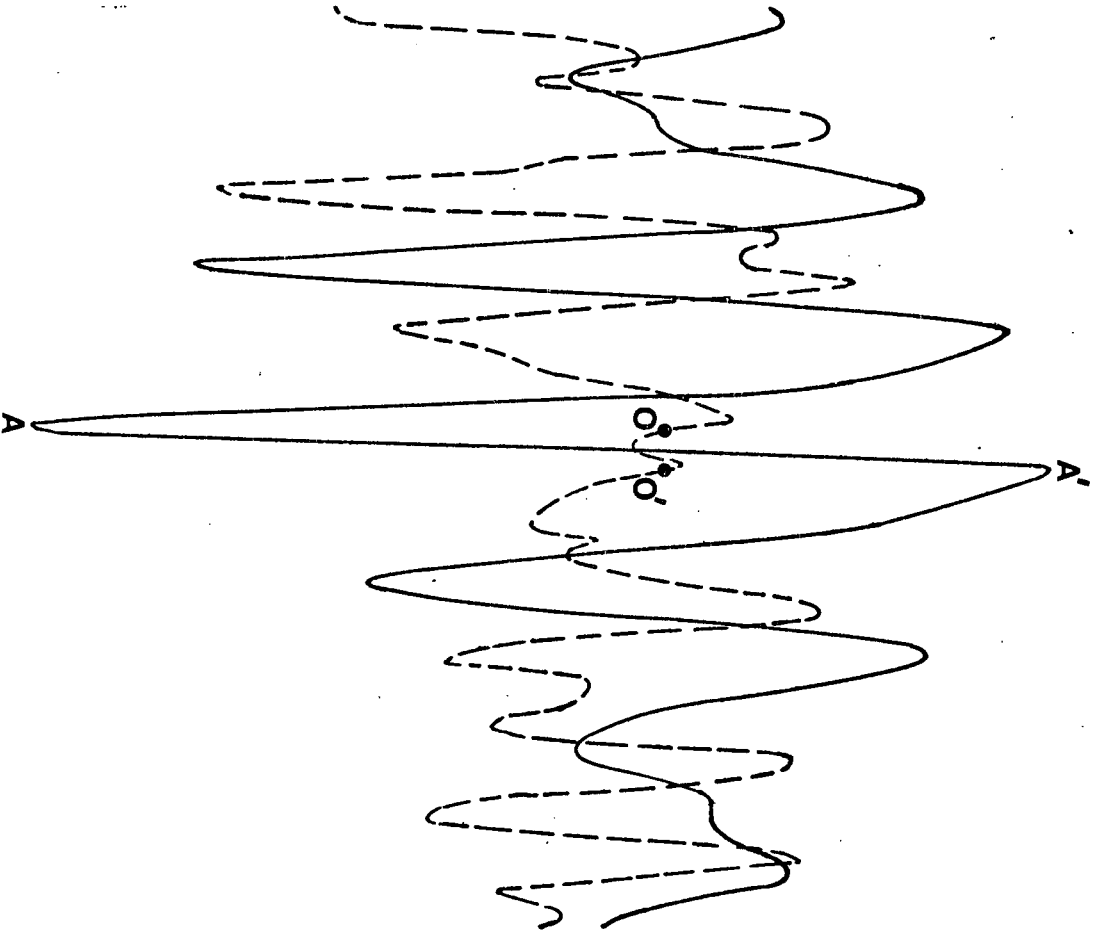


FIGURE 48

Theoretical response of a 12 slit I<sub>2</sub> Mask to the Fraunhofer lines in the 5200Å - 5560Å waveband.

Overlay of Figures 47 and 48 showing the region of interest for  $I_2$  detection (theoretical)

FIGURE 49



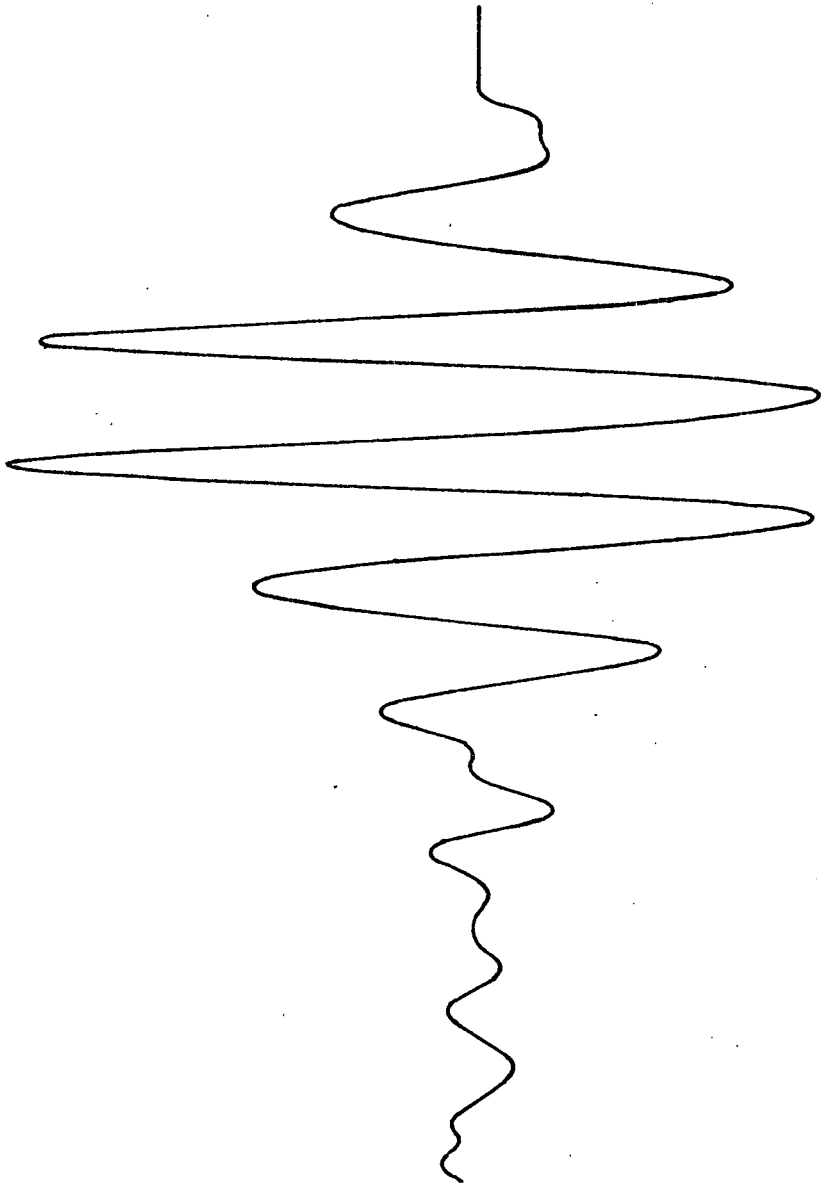


FIGURE 50

Experimental response of  $I_2$  to the 12 slit mask

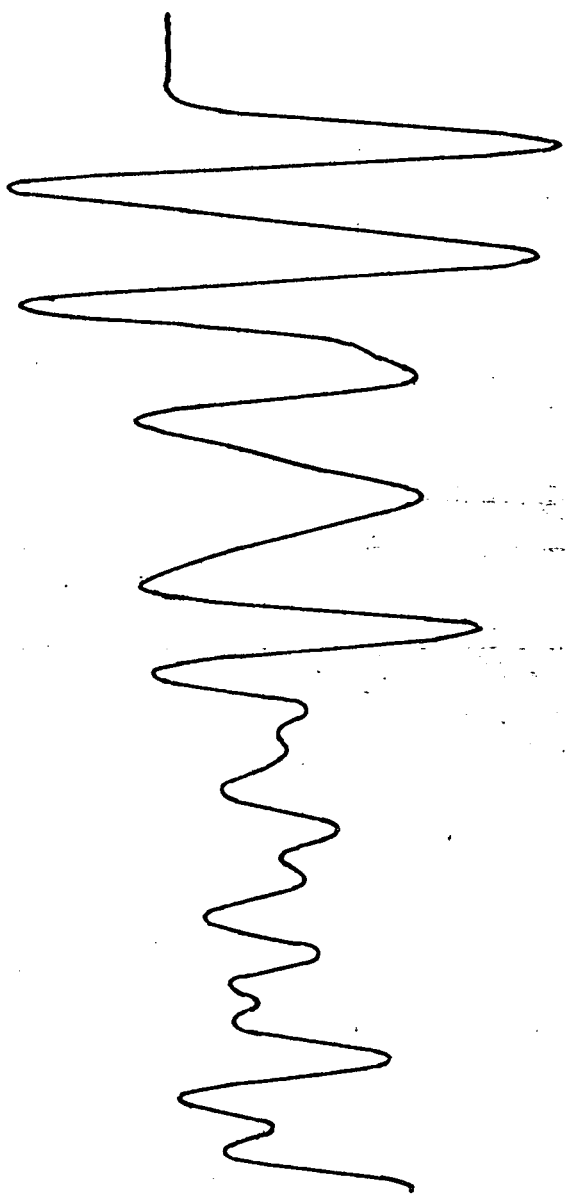


FIGURE 51

Experimental response of the 12 slit  $I_2$  mask to the Fraunhofer lines in the 5200 Å - 5600 Å waveband.

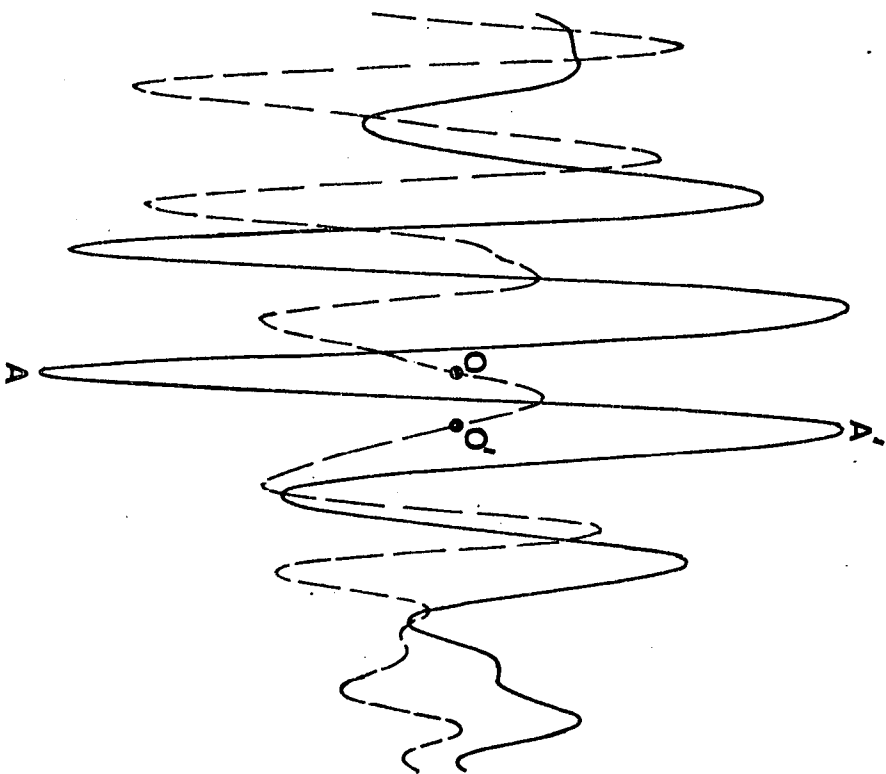


FIGURE 52

Overlay of Figures 50 and 51 showing the actual points of interest for  $I_2$  detection (experimental).